

# $\pi \cdots \pi$ interactions in aromatic systems: effect of distance and molecular size

Nuno Alexandre Sousa Dias

Mestrado em Química

Departamento de Química e Bioquímica  
2023

**Orientador**

Carlos Filipe Reis Alves Costa Lima

Investigador

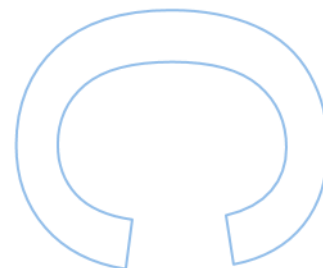
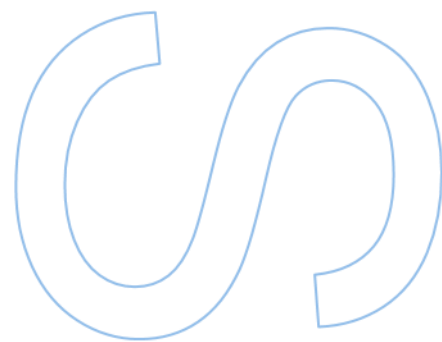
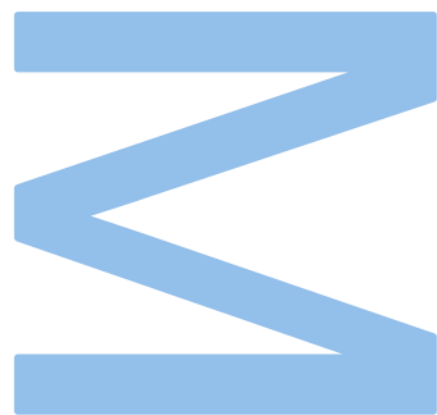
Faculdade de Ciências da Universidade do Porto

**Coorientador**

Luís Manuel das Neves Belchior Faia dos Santos

Professor Associado com Agregação

Faculdade de Ciências da Universidade do Porto

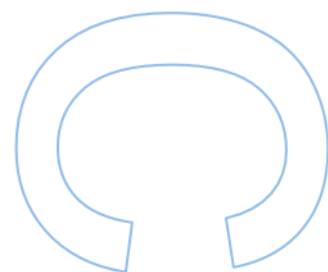
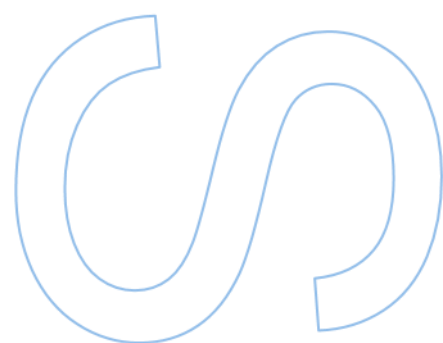
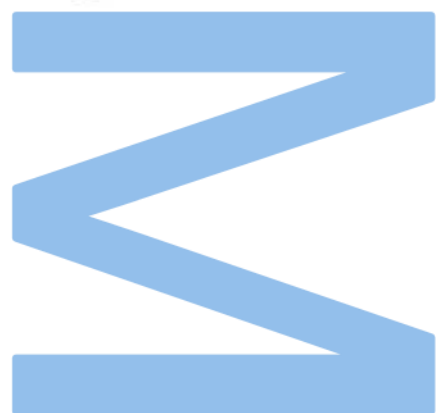








**U.** PORTO  
FC FACULDADE DE CIÊNCIAS  
UNIVERSIDADE DO PORTO





## Acknowledgements

First and foremost, I want to thank my supervisor, Dr. Carlos Lima, from the bottom of my heart for his invaluable guidance, mentoring, and unwavering support throughout my master's degree. His expertise and encouragement have been instrumental in shaping the direction and success of this research.

I'd like to express my gratitude to my co-supervisor, Prof. Luís Santos, who provided support throughout my research. I also would like to thank Prof. André Melo, who generously allowed me to utilize his computer's processors for conducting calculations, which greatly contributed to this work.

I would also like to thank my colleagues and fellow researchers at Faculdade de Ciências, especially Rita Carvalho, whose collaboration and camaraderie created a stimulating academic environment in which ideas could flourish. Their willingness to share their time and insights with me was critical to the successful completion of this study.

I am grateful to my family and friends, for their unwavering support, encouragement, and understanding during the challenges of this academic endeavor. Without them, I wouldn't be the man I am today.

To all who played a role, however small, in this academic journey, I would like to thank you for your contributions.

Thank you.

"Gratitude makes sense of our past, brings peace for today, and creates a vision for tomorrow."

– Melody Beattie



## Abstract

It has been known for more than 50 years that  $\pi$  systems can exhibit strong attractive interactions that affect a range of phenomena. Most notoriously, these include vertical interactions between DNA bases, which play a key role in stabilizing its double helix structure.

In this work, some 1,8-naphthalene and 1,8-anthracene derivatives were studied with the aim to comprehend how  $\pi\cdots\pi$  interactions in aromatic systems behaves when certain changes to the molecule structure are made. To achieve this, the compounds were firstly synthesized and characterized using a variety of techniques, including UV-Vis and NMR spectroscopy. The Knudsen-Quartz Crystal effusion (KNQ) method was employed to measure the temperature-dependent vapor pressures, and to determine the enthalpy, entropy, and Gibbs energy of sublimation for the compounds studied. The standard molar enthalpies of formation in the crystalline phase were determined by mini-bomb Combustion Calorimetry. Using these results, the standard molar enthalpies of formation in the gas phase were derived.

With the use of homodesmotic reaction schemes, the intramolecular  $\pi\cdots\pi$  interaction energy in the molecules studied was experimentally quantified and its dependence on molecular structure (interaction distance and size of the interacting partners) analyzed. Molecular energetics was tentatively described by computational calculations at the M06-2X/6-31+G(d,p) and CCSD(T)/cc-pVDZ level of theory. Most of the molecules studied exhibited significant energetic stabilization due to intramolecular  $\pi\cdots\pi$  interaction. From 1,8-diarylnaphthalenes to 1,8-diarylanthracenes, the interaction becomes more stabilizing due to the relieve of steric repulsions. However, the experimental results indicate the existence of an additional energetic effect on 1,8-diarylanthracenes. This effect has a stabilizing contribution of  $\sim 15 \text{ kJ}\cdot\text{mol}^{-1}$  in the molecules of 1,8-diarylanthracenes and is probably not related to dispersive interactions. Additional possible physical-chemical manifestations of this effect were discussed.



## Resumo

Há mais de 50 anos que se sabe que os sistemas  $\pi$  podem apresentar fortes interações atrativas que afetam uma série de fenómenos. Entre estes, destacam-se as interações verticais entre as bases do ADN, que desempenham um papel fundamental na estabilização da sua estrutura em dupla hélice.

Neste trabalho, foram estudados alguns derivados do 1,8-naftaleno e do 1,8-antraceno com o objetivo de compreender como se comportam as interações  $\pi \cdots \pi$  em sistemas aromáticos quando são feitas determinadas alterações na estrutura da molécula. Para isso, os compostos foram primeiramente sintetizados e caracterizados utilizando diversas técnicas, incluindo a espectroscopia UV-Vis e RMN. O método de efusão do cristal de quartzo de Knudsen (KNQ) foi utilizado para medir as pressões de vapor dependentes da temperatura e para determinar a entalpia, a entropia e a energia de Gibbs de sublimação para os compostos estudados. As entalpias molares padrão de formação na fase cristalina foram determinadas por Calorimetria de Combustão de mini-bomba. Utilizando estes resultados, foram derivadas as entalpias molares padrão de formação na fase gasosa.

Com o uso de esquemas de reação homodésmicas, a energia de interação intramolecular  $\pi \cdots \pi$  nas moléculas estudadas foi quantificada experimentalmente e a sua dependência da estrutura molecular (distância de interação e tamanho dos parceiros em interação) analisada. A energética molecular foi descrita tentativamente por cálculos computacionais ao nível da teoria M06-2X/6-31+G(d,p) e CCSD(T)/cc-pVDZ. A maioria das moléculas estudadas exibiu estabilização energética significativa devido à interação intramolecular  $\pi \cdots \pi$ . Dos 1,8-diarilnaftalenos para os 1,8-diarilantracenos, a interação torna-se mais estabilizadora devido ao alívio das repulsões estéricas. No entanto, os resultados experimentais indicam a existência de um efeito energético adicional nos 1,8-diarilantracenos. Este efeito contribui para a estabilização de cerca de  $\sim 15 \text{ kJ}\cdot\text{mol}^{-1}$  nas moléculas de 1,8-diarilantracenos e provavelmente não está relacionado com interações dispersivas. Foram discutidas possíveis manifestações físico-químicas adicionais deste efeito.



# Index

Acknowledgements.....	I
Abstract .....	III
Resumo .....	V
Table Index .....	IX
Figure Index.....	XI
List of Abbreviations.....	XVII
Introduction.....	1
Aromatic Interactions.....	3
Aromatic interactions in the gas phase .....	6
Aromatic interactions in the liquid phase .....	11
Aromatic interactions in the solid phase .....	13
Aromatic interactions in biomolecules .....	16
Intramolecular interactions .....	18
Substituents in Aromatic systems.....	18
Torsional Strain.....	20
Intramolecular C-H···π interaction .....	23
Quantification of Aromaticity and π-π stacking.....	27
Electron Correlation.....	30
Applications of 1,8-diarylanthracenes .....	33
Objective.....	35
Compounds Studied .....	36
Experimental Techniques.....	40
Suzuki-Miyaura Cross Coupling Reaction.....	40
Purification by sublimation under reduced pressure .....	43
Gas Chromatography .....	44
Fourier-transform Infrared Spectroscopy .....	46
UV-Vis Spectroscopy.....	48

Differential Scanning Calorimetry .....	50
Knudsen-Quartz Crystal effusion .....	53
Mini-bomb Combustion Calorimetry.....	58
Quantum Chemistry Calculations .....	66
Density Functional Theory .....	69
Coupled Cluster Theory .....	70
Configuration Interaction.....	72
Møller-Plesset Perturbation theory.....	73
Material and methods .....	75
Synthesis and characterization of the compounds.....	75
Synthesis of 1,8-diarylanthracenes.....	76
Fourier-transform Infrared Spectroscopy .....	81
UV-Vis Spectroscopy.....	81
Differential Scanning Calorimetry .....	82
Knudsen-Quartz Crystal .....	82
Mini-Bomb Combustion Calorimetry .....	85
Quantum Chemistry Calculations .....	87
Discussion of the Results.....	88
Phase Behaviour.....	89
Molecular Energetics.....	107
Optical Properties.....	125
Conclusion.....	128
Future Perspectives.....	132
Bibliography.....	134

## Table Index

<b>Table 1.</b> Barriers to internal rotation in substituted 1,8-diarylnaphthalene molecules (see Figure 10) [4].....	20
<b>Table 2.</b> List of the compounds studied in this work. Throughout this dissertation, the abbreviations shown will be used instead of the IUPAC names.....	38
<b>Table 3.</b> Results of the thermodynamic properties of fusion of three different polymorphs of 1,8-diPhAnth.....	93
<b>Table 4.</b> Experimental results concerning the fusion of the compound studied and some reference compounds, at $T_{\text{average}} = 433$ K. ....	93
<b>Table 5.</b> Increments in the enthalpy and entropy of fusion per substituent in the compounds studied, at $T = 433$ K. ....	95
<b>Table 6.</b> Experimental results obtained for the sublimation of 1,8-diPhAnth, in the Knudsen-Quartz crystal effusion apparatus.....	97
<b>Table 7.</b> Experimental results obtained for the sublimation of 1,8-bismethoxyPhAnth, in the Knudsen-Quartz crystal effusion apparatus.....	98
<b>Table 8.</b> Experimental results obtained for the sublimation of 1,8-dibiPhAnth, in the Knudsen-Quartz crystal effusion apparatus.....	99
<b>Table 9.</b> Experimental results obtained for 1,8-diPhAnth, where a and b are from the Clausius-Clapeyron equation $\ln(p / \text{Pa}) = b - a \cdot (K / T)$ , and $a = \Delta_{\text{sub}}H^0 (<T>)/R$ . ....	100
<b>Table 10.</b> Experimental results obtained for 1,8-bismethoxyPhAnth, where a and b are from the Clausius-Clapeyron equation $\ln(p / \text{Pa}) = b - a \cdot (K / T)$ , and $a = \Delta_{\text{sub}}H^0 (<T>)/R$ . ....	100
<b>Table 11.</b> Experimental results obtained for 1,8-dibiPhAnth, where a and b are from the Clausius-Clapeyron equation $\ln(p / \text{Pa}) = b - a \cdot (K / T)$ , and $a = \Delta_{\text{sub}}H^0 (<T>)/R$ . ....	100
<b>Table 12.</b> Global results for the enthalpies, entropies, and Gibbs energies of sublimation at $T = 298.15$ K. ....	102
<b>Table 13.</b> Increments in the enthalpy and entropy of sublimation, at $T = 298.15$ K, per substituent in the compounds studied. ....	104
<b>Table 14.</b> Experimental results for the combustion of 1,8-diphenylanthracene, at $T = 298.15$ K. ....	108
<b>Table 15.</b> Experimental results for the combustion of 1,8-bis(4-methoxyphenyl)anthracene, at $T = 298.15$ K.....	109
<b>Table 16.</b> Experimental results for the combustion of 1,8-di([1,1'-biphenyl]-4-yl)anthracene, at $T = 298.15$ K.....	110

**Table 17.** Raw computational data obtained for each compound.  $H_{298.15}$  corresponds to the sum of electronic,  $E_{el}$ , and thermal enthalpies. Optimization and frequency calculations were made using M06-2X/6-31+G(d,p). The CCSD(T) results are single-point energy energy calculations on MP2/cc-pVDZ optimized geometries. .... 112

**Table 18.** Standard molar enthalpies of combustion, as measured by mini-bomb combustion calorimetry, and derived standard molar enthalpies of formation of the compounds studied in the crystal phase, at  $T = 298.15$  K. .... 113

**Table 19.** Experimental values of  $\Delta_f H^0(g)$  for the compounds studied. .... 114

**Table 20.** Experimental and theoretical calculated, M06-2X/6-31+G(d,p) and CCSD(T)/cc-pVDZ, enthalpies of reaction in the gas phase, at  $T = 298.15$  K..... 116

**Table 21.** Experimental and theoretical calculated, M06-2X/6-31+G(d,p) and CCSD(T)/cc-pVDZ, enthalpies of reaction in the gas phase, at  $T = 298.15$  K..... 118

**Table 22.** Experimental and theoretical calculated, M06-2X/6-31+G(d,p) and CCSD(T)/cc-pVDZ, enthalpies of reaction in the gas phase, at  $T = 298.15$  K..... 120

## Figure Index

<b>Figure 1.</b> Interaction energies as a function of the Hammett meta-constant, $\sigma_m$ , for $C_6H_5X \cdots C_6H_6$ sandwich dimers, for which X is from a set of 25 diverse substituents [6].	5
<b>Figure 2.</b> Interaction energies as a function of the Hammett meta-constant, $\sigma_m$ , for $HX \cdots C_6H_6$ sandwich dimers, for which X is from a set of 25 diverse substituents [6].	5
<b>Figure 3.</b> Visual representation of benzene (left) and hexafluorobenzene (right).	7
<b>Figure 4.</b> The configurations of benzene dimer in the gas phase: the parallel (P), T-shaped (T) and parallel-displaced (PD) configurations [11].	8
<b>Figure 5.</b> MP2 and CCSD(T) potential energy curves for the sandwich configuration of the benzene dimer using counterpoise (CP) correction [11].	9
<b>Figure 6.</b> MP2 and CCSD(T) potential energy curves for the T-shaped configuration of the benzene dimer, using counterpoise (CP) correction. $\Delta$ CCSD(T) denotes the difference between CCSD(T) and MP2 [11].	10
<b>Figure 7.</b> Visual representation of the conformations of the benzene dimer: Parallel face-to-face sandwich (S); parallel displaced (PD); perpendicular T-shaped (T); perpendicular Y-shaped (Y) [13].	12
<b>Figure 8.</b> The arrangement of benzene and hexafluorobenzene in a stacked configuration [18].	14
<b>Figure 9.</b> The four basic aromatic crystal packings. Naphthalene – herringbone structure; Pyrene – sandwich-herringbone packing; Coronene – $\gamma$ packing; Tribenzopyrene – $\beta$ packing [19].	15
<b>Figure 10.</b> (a) A dynamic equilibrium approach was employed to assess the impact of substituents on aromatic stacking interactions between phenyl rings bearing different substitutions (X = OMe, Me, H, Cl, CO <sub>2</sub> Me, NO <sub>2</sub> ); (b) Fluorination of the 1,8-diarylnaphthalene derivatives changes the quadrupole moment of the aromatic ring and consequently the trends in stacking interaction energy [5].	19
<b>Figure 11.</b> Ring-opening strategy for atropisomer synthesis. The increase of torsional strain decreases the amount of energy needed for the ring-opening process [25].	21
<b>Figure 12.</b> Three distinct types of helically twisted ribbons. I) the stereogenic axis doesn't have an intersection with the ribbon (helicene-type); II) the stereogenic axis is identical to the main axis of the ribbon (twistacene-type); III) the stereogenic axis is identical to the black edge of the ribbon (bannister-type). In types I and III, the blue edge is longer than the black one, while in type II, the blue and black edges have the same length [26].	22

<b>Figure 13.</b> O-hydroxyacyl aromatic compounds used in the study mentioned [34].....	24
<b>Figure 14.</b> Illustration of the labelling of atoms, and the thermal motions of atoms in <b>1</b> (a), <b>2</b> (b), and <b>4</b> (c) are depicted. The numbering schemes for <b>1</b> and <b>2</b> are derived from the one used for <b>3</b> [34]. .....	26
<b>Figure 15.</b> (a) The acyl group in <b>4</b> exhibits an out-of-plane deformation; (b and c) In the crystal lattice of <b>4</b> , there are Me···π-electron interactions [34].....	26
<b>Figure 16.</b> Isodesmic reaction to study the stabilization of benzene [39]. .....	27
<b>Figure 17.</b> Homodesmotic gas phase reaction of 1,8-diphenylnaphthalene to assess the intramolecular aromatic interactions. The reported values, indicated as experimental (in bold), DFT (B3LYP/6-311++G(d,p)), and MP2 (SCS-MP2/cc-pVDZ), represent the corresponding energy values in kJ·mol <sup>-1</sup> [41]. .....	28
<b>Figure 18.</b> Visual representation of 1,8-diarylanthracene.....	33
<b>Figure 19.</b> Visual representation of a 1,8-diarylnaphthalene, in this case 1,8-di([1,1'-biphenyl]-4-yl)naphthalene [41]. .....	35
<b>Figure 20.</b> Visual representation of naphthalene. ....	36
<b>Figure 21.</b> Visual representation of anthracene. ....	36
<b>Figure 22.</b> From the left to the right: phenyl; 4-methoxyphenyl; 4-formylphenyl; biphen-4-yl group.....	37
<b>Figure 23.</b> Schematic of the widely accepted mechanism of C-C cross-coupling reactions. ....	42
<b>Figure 24.</b> Schematic of the widely accepted reaction mechanism for the Suzuki-Miyaura cross-coupling reaction. A <sup>+</sup> and Nu <sup>-</sup> stands for, respectively, a cation and a nucleophile. ....	42
<b>Figure 25.</b> Schematic representation of 1,1':4',1'':4'',1''':4'''-quaterphenyl (p-quaterphenyl). .....	43
<b>Figure 26.</b> Low pressure sublimator used in this work. ....	44
<b>Figure 27.</b> Visual representation of a basic schematic of a gas chromatograph [52]....	45
<b>Figure 28.</b> Agilent 4890D Gas Chromatograph used in this work.....	46
<b>Figure 29.</b> Schematic diagram of the components of a Michelson interferometer [53].	47
<b>Figure 30.</b> GLADIATR™ FTIR spectrometer used in this work. ....	48
<b>Figure 31.</b> Agilent 8453 UV-Vis Spectrophotometer (a) used in this dissertation. The spectrophotometer is linked to a refrigeration system (b) and to a pc interface (c) for data acquisition. ....	50
<b>Figure 32.</b> Perkin Elmer-PYRIS Diamond-Differential Scanning Calorimeter. ....	52
<b>Figure 33.</b> Schematics of the furnaces of a Perkin Elmer-PYRIS Diamond-Differential Scanning Calorimeter [59].....	52

**Figure 34.** Schematic diagram of the effusion process in the KNQ apparatus. a) Quartz crystal holder; b) mass flow; c) Knudsen effusion cell [60]. ..... 54

**Figure 35.** Knudsen effusion device that detects mass loss using both gravimetric and quartz crystal microbalance methods..... 57

**Figure 36.** Schematic of the Knudsen effusion apparatus with quartz-crystal mass loss detection [60]. ..... 57

**Figure 37.** Graphical representation of an isoperibol calorimetry experiment..... 59

**Figure 38.** Thermodynamic cycle used for the derivation of  $\Delta U_{IBP}$ . ..... 62

**Figure 39.** Thermodynamic cycle used for the derivation of  $\Delta_c u^0$  from  $\Delta U_{IBP}$ . ..... 64

**Figure 40.** Left) Schematic of the mini-bomb calorimeter. A) isolating polystyrene; B) water bath thermostat; C) thermostat stirring motor; D) temperature controller (Tronac PTC40); E) 612 digits multimeter (Keithley 2000); F) firing unit; G) personal computer and monitor; H) water-cooling source (Julabo F12-ED); I) insulating calorimeter block support; J) calorimeter block with the bomb; K) DB25 wire connector [61]; Right) Visual representation of the schematics of the bomb, DC motor and the support. A) bomb body; B) Viton O-ring; C) retaining stainless steel ring; D) DC motor; E) electrical terminals; F) bomb and motor support; G) resistor in parallel with the firing circuit; H) firing electrical contact; I) head of the bomb; J) platinum support and electrodes; K) head of the calorimeter block; L) calorimeter block body; M) thermistor; N) DB25 electrical connector; O) thermal insulator [61]. ..... 65

**Figure 41.** Schematic of the bomb assembling. A) bomb body; B) platinum sheet; C) bomb head; D) retaining ring; E) crucible with the sample; F) Viton O-ring [61]..... 65

**Figure 42.** Mini-bomb calorimeter used in this work (left image) and the components of a mini-bomb calorimeter (right image). A) bomb body; B) piece with a bomb head, Viton O-ring, where the crucible with the sample will be positioned and where the platinum sheet must be put over; C) bomb and motor support with DC motor, electrical terminals, and a firing electrical contact..... 66

**Figure 43.** Visual representation of the change of gradient,  $\nabla \rho_{exact} - \nabla \rho_{HF}$  (y axis), due to correlation. The horizontal axis indicates the distance from the center of the Hooke atom [63]. ..... 67

**Figure 44.** Representation of the change of electron density due to correlation:  $\rho_{exact} - \rho_{HF}$  (y axis). The horizontal axis indicates the distance from the center of the Hooke atom [63]. ..... 68

**Figure 45.** Visual representation of graphical examples of selected single  $\Phi_{ia}$ , double  $\Phi_{ijab}$ , triple  $\Phi_{ijkabc}$  excitations due to the  $T_1(C_1)$ ,  $T_2(C_2)$  and  $T_3(C_3)$  operators, respectively [68]. ..... 71

**Figure 46.** Visual representation of the catalyst, otherwise known as PEPPSI. .... 76

<b>Figure 47.</b> <sup>1</sup> H NMR spectrum of 1,8-diphenylanthracene in CDCl <sub>3</sub> .	78
<b>Figure 48.</b> <sup>13</sup> C NMR spectrum of 1,8-diphenylanthracene in CDCl <sub>3</sub> .	78
<b>Figure 49.</b> <sup>1</sup> H NMR spectrum of 1,8-di([1,1'-biphenyl]-4-yl)anthracene in CDCl <sub>3</sub> .	79
<b>Figure 50.</b> <sup>13</sup> C NMR spectrum of 1,8-di([1,1'-biphenyl]-4-yl)anthracene in CDCl <sub>3</sub> .	79
<b>Figure 51.</b> <sup>1</sup> H NMR spectrum of 1,8-bis(4-methoxyphenyl)anthracene in CDCl <sub>3</sub> .	80
<b>Figure 52.</b> <sup>13</sup> C NMR spectrum of 1,8-bis(4-methoxyphenyl)anthracene in CDCl <sub>3</sub> .	80
<b>Figure 53.</b> DSC thermogram of 1,8-diPhAnth, performed at a heating rate of 5 K/min and showing the fusion and crystallization processes. Graph made with Statistica Software.	89
<b>Figure 54.</b> DSC thermogram of 1,8-diPhAnth, performed at a heating rate of 5 K/min and one time at a heating rate of 30 K/min (~260 min). This thermogram shows the fusion and crystallization processes of the compound. Graph made with Statistica Software.	90
<b>Figure 55.</b> DSC thermogram of heat flow as a function of temperature of 1,8-diPhAnth, performed at a heating rate of 5 K/min and one time at a heating rate of 30 K/min (~260 min). This thermogram shows the fusion and crystallization processes of the compound. Graph made with Statistica Software.	90
<b>Figure 56.</b> Single-crystal structures of two 1,8-diPhAnth polymorphs. Left) face-to-edge; Right) face-to-face [77].	92
<b>Figure 57.</b> X-Ray taken on 1,8-diphenylanthracene that shows the packing of the compound and its molecular structure in the solid phase.	96
<b>Figure 58.</b> X-Ray taken on 1,8-diphenylnaphthalene that shows the packing of the compound and its molecular structure in the solid phase.	96
<b>Figure 59.</b> Graphical representation of the $\ln(P/Pa)=f(1/T)$ for the experiments of 1,8-diPhAnth using the Knudsen-Quartz Crystal method.	101
<b>Figure 60.</b> Graphical representation of the $\ln(P/Pa)=f(1/T)$ for the experiments of 1,8-bismethoxyPhAnth using the Knudsen-Quartz Crystal method.	101
<b>Figure 61.</b> Graphical representation of the $\ln(P/Pa)=f(1/T)$ for the experiments of 1,8-dibiPhAnth using the Knudsen-Quartz Crystal method.	102
<b>Figure 62.</b> X-Ray taken on 1,8-bis(4-methoxyphenyl)naphthalene that shows the packing of the compound and its molecular structure in the solid phase.	104
<b>Figure 63.</b> X-Ray taken on 1,8-di([1,1'-biphenyl]-4-yl)naphthalene that shows the packing of the compound and its molecular structure in the solid phase.	105
<b>Figure 64.</b> X-Ray taken on 1,8-bis(4-methoxyphenyl)anthracene that shows the packing of the compound and its molecular structure in the solid phase.	106
<b>Figure 65.</b> View from the top of the molecular structure of 10-bromo-1,8-diphenylanthracene [84].	111

**Figure 66.** Left) Graphical representation of PES for the configurations T-shaped and Parallel displaced. Right) Visual representation of two configurations: up) T-shaped configuration; down) Parallel displaced [11,14,41,83]..... 115

**Figure 67.** M06-2X/6-31+G(d,p) optimized geometry of 1,8-dibiPhAnth..... 119

**Figure 68.** Visual representation of 10-bromo-1,8-diphenylanthracene..... 122

**Figure 69.** Left) 1,8-diarylanthracene; Right) <sup>1</sup>H NMR spectra of 1,8-dibiPhAnth, 1,8-bismethoxyPhAnth and 1,8-diPhAnth. The spectra, recorded in CDCl<sub>3</sub> at T = 298 K, show the differences between the chemical shifts of the two protons in ppm. .... 123

**Figure 70.** Visual representation of the possible electronic effect between two substituents and the hydrogen atom bonded to C-9, in 1,8-diarylanthracene. .... 124

**Figure 71.** Plot of UV-Vis spectra, in CH<sub>2</sub>Cl<sub>2</sub> at T = 298.1 K, comparing 1,8-diPhNaph, 1,8-diPhAnth and 9,10-diPhAnth analogs. The small hump centered at ~ 290 nm is a prominent feature of 1,8-diPhAnth. .... 125

**Figure 72.** Plot of UV-Vis spectra, in CH<sub>2</sub>Cl<sub>2</sub> at T = 298.1 K, comparing 1,8-bismethoxyPhNaph and 1,8-bismethoxyPhAnth analogs. .... 125

**Figure 73.** Plot of UV-Vis spectra, in CH<sub>2</sub>Cl<sub>2</sub> at T = 298.1 K, comparing 1,8-dibiPhNaph and 1,8-dibiPhAnth analogs. .... 126

**Figure 74.** Plot of UV-Vis spectra, in CH<sub>2</sub>Cl<sub>2</sub> at T = 298.1 K, comparing the three 1,8-diarylnaphthalene studied. .... 126

**Figure 75.** Plot of UV-Vis spectra, in CH<sub>2</sub>Cl<sub>2</sub> at T = 298.1 K, comparing the three 1,8-diarylanthracenes studied and 9,10-diPhAnth. .... 127



## List of Abbreviations

- 1-([1,1'-biphenyl]-4-yl)naphthalene – 1-biPhNaph
- 1-(-4-methoxyphenyl)naphthalene – 1-methoxyPh
- 1,8-bis(4-methoxyphenyl)anthracene – 1,8-bismethoxyPhAnth
- 1,8-bis(4-methoxyphenyl)naphthalene – 1,8-bismethoxyPhNaph
- 1,8-di([1,1'-biphenyl]-4-yl)anthracene – 1,8-dibiPhAnth
- 1,8-di([1,1'-biphenyl]-4-yl)naphthalene – 1,8-dibiPhNaph
- 1,8-diphenylanthracene – 1,8-diPhAnth
- 1,8-diphenylnaphthalene – 1,8-diPhNaph
- 1-phenylnaphthalene – 1-PhNaph
- 4-(naphthalen-1-yl)benzaldehyde – 4-Naph-1-BenzAl
- 4,4'-(anthracene-1,8-diyl)dibenzaldehyde – 4,4'-Anth-1,8-diBenzAl
- 4,4'-(naphthalene-1,8-diyl)dibenzaldehyde – 4,4'-Naph-1,8-diBenzAl
- Configuration Interaction – CI
- Coupled cluster singles and doubles – CCSD
- Coupled Cluster Theory – CC
- Density Functional Theory – DFT
- Dibenzyl ketone – DBK
- Differential Scanning Calorimetry – DSC
- Fourier-transform Infrared Spectroscopy – FTIR
- Gas Chromatography – GC
- Hartree-Fock – HF
- Knudsen-Quartz Crystal – KNQ
- Møller-Plesset perturbation theory – MP2
- Potential energy surface – PES



## Introduction

Aromatic groups are found in countless chemical systems in nature, for example, in most biomolecules such as DNA or proteins, in a lot of types of drugs, supramolecular aggregates, etc. Therefore, the properties of aromatic molecules and the type of interactions they can form are fundamental to defining the behavior of such systems [1].

In chemistry, a compound being aromatic means that it is unsaturated and contains several double bonds. When the terms aromatic and aromatic character are mentioned, most tend to think of benzene, since benzene is the simplest aromatic compound, but the definition of aromaticity is much broader than just being a derivative of benzene.

The issue of defining aromaticity has become so significant that there were around 60,000 scientific papers between 1981 and 2000 that discussed the concept of aromaticity in chemistry using the terms "aromaticity" or "aromatic" [2].

Aromaticity is not directly measurable, and its quantification is a challenge since aromaticity influences various chemical-physical properties, which makes it difficult to separate this phenomenon from other interferences.

While electron delocalization is a key factor associated with aromaticity in molecules, it is not the sole determinant of aromaticity. For a system to be called aromatic, the delocalization needs to obey some rules, these being [2]:

- The geometry of the aromatic system is planar, or close to planar.
- In cases where the stability of a system is greater than that of its cyclic, acyclic, or conjugated unsaturated counterparts, the additional stability was once referred to as "resonance energy" and later termed "aromatic stabilization energies" based on homodesmotic reactions.
- The cyclic C-C bond lengths are generally between the values typical for single and double bonds. Scientists use several measurements to quantify this effect. One of these is called the geometric index. Among these measurements, the harmonic oscillator model of aromaticity (HOMA) is the most accurate. It provides information about how aromatic a molecule is and is easy to calculate.

- A diatropic  $\pi$  ring current is generated by the presence of an external magnetic field.
- The  $4n+2$  rule, also known as Hückel's rule, determines aromaticity in cyclic conjugated hydrocarbon rings. Aromatic rings have  $4n+2$   $\pi$  electrons.

Aromaticity can be considered a multi-dimensional phenomenon, with it being characterized by 4 points: Energetics; geometry; magnetism; reactivity [1].

- Energetics – the additional stability of the system, given by the aromaticity, is manifested, by the electron delocalization.
- Geometry - The arrangement of the nuclei in an aromatic system results in similar internuclear distances. Additionally, aromatic systems are typically planar in structure.
- Magnetism - When aromatic rings are exposed to an external magnetic field, they exhibit a pronounced diatropic electronic ring current. This phenomenon is responsible for the shielding of aromatic protons in nuclear magnetic resonance (NMR) and prevents their detection or observation.
- Reactivity - Aromatic systems generally show significantly lower reactivity when the reaction somehow involves a loss of aromaticity.

The main feature that distinguishes aromatic compounds from other substances is their increased stability, which is due to the presence of cyclic  $\pi$ -electron delocalization. This increased stability is defined as the energy difference between a compound with cyclic  $\pi$ -electron delocalization and a reference system with minimal  $\pi$ -electron delocalization. This concept has been extended to other cyclic  $\pi$ -electron systems, and the term "aromatic stabilization energy" (ASE) is now commonly used to describe this enhanced stability. Various methods, such as isodesmic and homodesmotic reactions, can be used to estimate ASE. However, it is important to note that different approaches may give different results for a given system [3]. It has been noted that the ASE values can offer valuable insights into the degree of  $\pi$ -electron delocalization, given that the

model reaction is carefully designed and consistent in terms of structural variations across the entire set of systems.

Methods based on molecular geometry, such as HOMA (harmonic oscillator model of aromaticity), can calculate the quantity that can correlate with the aromaticity using the following equation [3]:

$$HOMA = 1 - \frac{\alpha}{n} \cdot \sum (R_{opt} - R_i)^2 \quad \text{Eq. 1}$$

Where  $n$  is the number of chemical bonds that enter the summation,  $R_{opt}$  is the optimal bond length,  $R_i$  is the current bond length, and  $\alpha$  is a parameter chosen under the form of HOMA=0 for a non-aromatic model and HOMA=1 for a model where all  $R_i$  are equal to  $R_{opt}$ .

The nuclear independent chemical shift (NICS) is often used as a depiction of aromaticity from the magnetic point of view. The index is determined by taking the negative value of the absolute magnetic shielding calculated at specific points within the molecule, often at the centroid of the aromatic ring (NICS) or slightly above (NICS1). This value indicates the degree of shielding that the molecule provides against an external magnetic field. This value is taken into account, and a more negative NICS value indicates a stronger ring current and higher aromaticity within the system [2,3]. Rings characterized by significantly negative NICS values are classified as aromatic, while those with positive values are considered anti-aromatic [3].

## Aromatic Interactions

To understand the behavior of aromatic systems, one must understand the properties of aromatic molecules and the types of interactions they can establish. These systems exhibit relatively high polarizability and generate quadrupole moments due to the interaction between the  $\sigma$  and  $\pi$  frameworks of the aromatic groups. As a result, significant dispersive van der Waals interactions and electrostatic interactions can occur [1]. Generally, the two structures that are observed in interactions between two aromatic

systems are the T-shaped and parallel-displaced forms. Although aromatic complexes can also adopt a stacked structure, it is rarely observed since this form is unstable.

Aromatic groups are usually observed covalently bonded to other molecular groups. This bond influences the electrical properties of the aromatic structures and the way they interact inter- and intramolecularly [1]. Because of this, it is important to know how different substituents affect aromatic interactions.

There are several effects to be considered when non-covalent interactions between two molecules occur [4]:

- Van der Waals, which is the sum of repulsion/attraction and dispersion energies.
- Electrostatic interactions between the static molecular charge distributions.
- Induction energy, which in the interaction between the static molecular charge distribution of one molecule and the induced charge distribution of the other.
- Charge transfer, which is a stabilization due to the mixing of the ground state with an excited charge-separated state.
- Desolvation, where two molecules that form a complex in solution must release some solvent molecules before complexation can occur.

To dig into this further, there was a computational study made on the influence that different substituents have in noncovalent interaction involving the simplest aromatic system, benzene. In this study, the authors showed that both electron donors and acceptors strengthen the interaction, and that the unsubstituted benzene dimer was determined to be the outlier. It was proposed that the general trend that both types of substituents have is correlated to electrostatic interactions [6].

In the case of the nonzero  $y$ -intercept in Figure 1, it shows the stabilization of all substituted dimers in relation to the unsubstituted benzene, which is attributed to dispersion interactions.

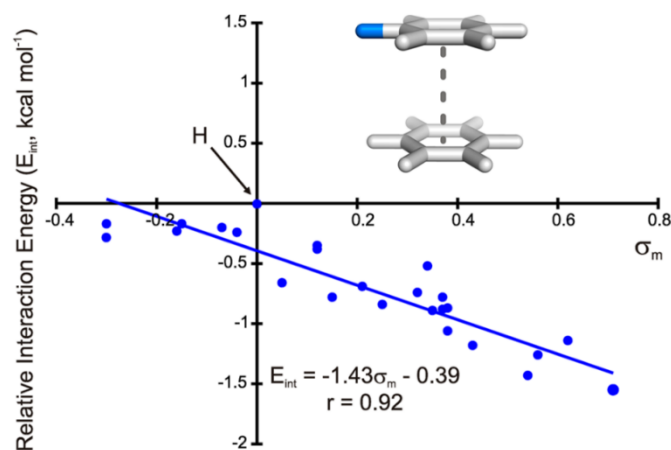


**Figure 1.** Interaction energies as a function of the Hammett meta-constant,  $\sigma_m$ , for  $C_6H_5X \cdots C_6H_6$  sandwich dimers, for which X is from a set of 25 diverse substituents [6].

The authors also show that the correlation with  $\sigma_m$  becomes less reliable for polysubstituted dimers, as the significance of dispersion interactions increases [6].

It was also shown in this study that the substituent effects in the benzene dimer follow the same trend if the substituted ring is replaced with a hydrogen atom (Figure 2).

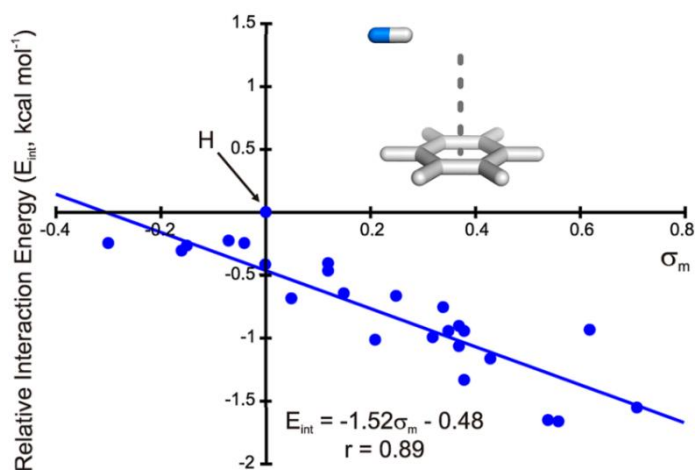


**Figure 2.** Interaction energies as a function of the Hammett meta-constant,  $\sigma_m$ , for  $HX \cdots C_6H_6$  sandwich dimers, for which X is from a set of 25 diverse substituents [6].

The substituent effects in  $C_6H_5X\cdots C_6H_6$  dimers are correlated with those in  $HX\cdots C_6H_6$  dimers at the same monomer separation (Figure 1 and Figure 2). The fact that the substituent effects are similar when the aryl ring is replaced by hydrogen suggests that the involvement of the aryl- $\pi$  system in these effects is not significant. Instead, the effects were attributed solely to direct interactions between the substituent and the unsubstituted ring [6].

### Aromatic interactions in the gas phase

The above studies were carried out in the gas phase, where the molecular species studied were isolated and subjected to detailed analyses. In this controlled environment, without intermolecular interactions or external influences, the properties and behaviour of the systems studied could be studied in detail. The gas phase provides an ideal environment to explore the fundamental properties of these molecular dimers. It allows precise spectroscopic measurements and the description of their complicated conformations and spectral features.

Kenneth Janda *et al.* conducted a study on benzene dimers using molecular beam deflection techniques [7]. In this study, the dimer was found to be polar, and this polarity was attributed to the presence of a permanent electric dipole moment in the ground vibrational state. Because of this, the equilibrium geometry of the benzene dimer is one admitting a permanent dipole moment. Since all reasonable geometries in which the planes of the two benzene molecules are parallel give a nonpolar dimer, these possibilities are eliminated [4,7]. The authors admitted that the T-shaped conformation is relevant in the gas phase.

In a separate study, hexafluorobenzene and benzene-hexafluorobenzene dimers were studied (molecular structures shown in Figure 3). While Kenneth Janda *et al.* had previously explained the polarity observed for the benzene dimer, the results for the hexafluorobenzene dimer were new and provided additional insight into its structure [7,8]. The low-frequency zero-field spectra further support this study, as asymmetric doublet transitions are expected in this region. The expected centre-to-centre distance for such a structure in the benzene dimer is about 5 Å. In contrast, the results suggest that the benzene-hexafluorobenzene dimers adopt a planar parallel conformation in the gas phase [7].

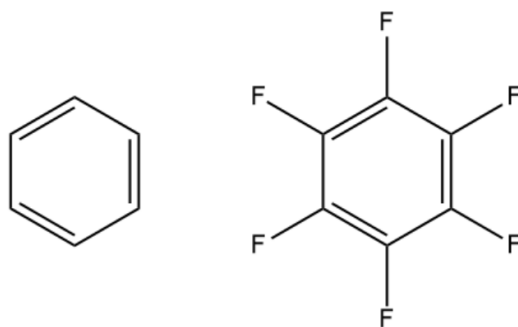


**Figure 3.** Visual representation of benzene (left) and hexafluorobenzene (right).

In addition, Levy and colleagues conducted a study on *s*-tetrazine dimers and discovered that this particular dimer is ideally suited for the study of various energy transfer processes due to its well-defined spectroscopic properties. The high-resolution electronic spectra of the dimers revealed the existence of two stable conformations in the gas phase. In one conformation, the two rings are located in a common plane, while in the other conformation, the two rings are arranged perpendicular to each other in a T-shaped configuration [4,9]. In the planar configuration, the two monomers are identical in their translational properties, resulting in delocalization of electronic excitation in the complex. In the T-shaped conformation, on the other hand, the monomers differ in their translational properties, leading to localization of vibronic excitation within a single ring, as shown by the polarization of the high-resolution electronic spectrum [9]. Consequently, the two dimer configurations yield three distinct vibronic bands: one for the planar dimer and two for the T-shaped dimer. These three vibronic bands are clearly separated in absorption [9].

A scientific publication by Francesco Luigi Gervasio and colleagues dealt with the interactions between aromatic residues in biological molecular systems. It was found that aromatic residues can be involved in certain energetically favorable interactions. For example, base stacking plays an important role in stabilizing the helical structure of DNA, while interactions between planar aromatic side chains contribute to the stability of protein structures [10].

The preferred arrangement for the benzene dimer in the gas phase and in crystalline benzene is the T-shaped structure, in which the planes of the rings are perpendicular to each other. In addition, there are other local minima such as the "edge-displaced" structure (with parallel displacement of the ring planes) and the "sandwich" structure

(with superimposed planes) (shown in Figure 4), both of which are stabilized by dispersion interactions. In aromatic compounds with polar moieties, the energetics of these structures, which are characterized by weak and favorable dispersion interactions, are also strongly affected by electrostatic interactions and hydrogen bonds [10].

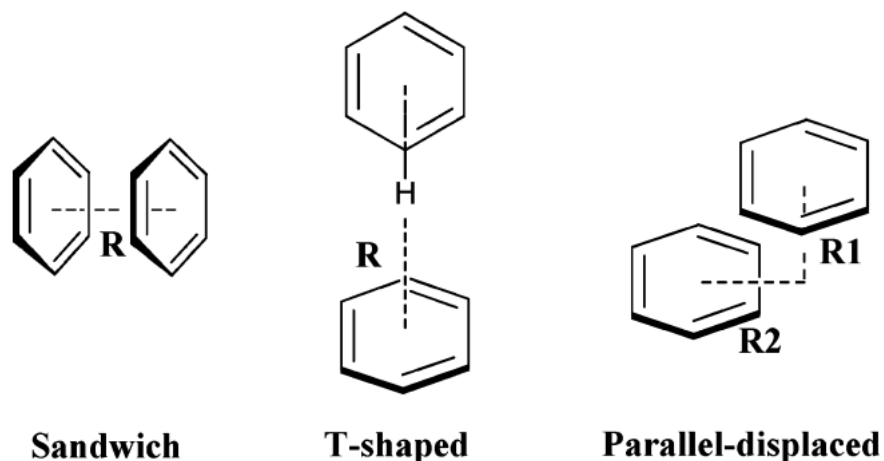


**Figure 4.** The configurations of benzene dimer in the gas phase: the parallel (P), T-shaped (T) and parallel-displaced (PD) configurations [11].

To understand the competition between T-shaped and stacked structures at finite temperatures, an accurate representation of the potential energy surface (PES) for interactions between aromatic compounds is crucial. Correlated ab initio methods can provide accurate calculations of energy and structure but are computationally intensive and limit their application to selected points on the PES. On the other hand, empirical *force fields* (FF), developed specifically for modeling protein interactions, have demonstrated their reliability in representing the PES of biological molecular interactions. Although the interaction energies obtained with empirical *force fields* are only approximations, they are computationally convenient for studying the PES in more detail using molecular dynamics simulations [10].

In their extensive study, Sinnokrot and Sherrill used advanced computational methods to calculate the geometric and energetic properties of the benzene dimer, focusing in particular on parallel, T-shaped, and parallel-displaced structures [11]. The benzene dimer was chosen as a fundamental model for aromatic  $\pi\cdots\pi$  interactions, which have already been extensively studied [11]. Their goal was to gain a comprehensive understanding of the direction and strength of  $\pi\cdots\pi$  interactions, which required theoretical analyses.

The researchers were faced with the challenge of accurately determining the binding energy of the benzene dimer in the gas phase ( $\sim 8$ - $12$  kcal.mol<sup>-1</sup>) and the complex potential energy surface associated with these interactions. Furthermore, the steric constraints imposed on the aromatic groups added complexity, as the geometries may not conform to the global potential energy minima for  $\pi \cdots \pi$  interactions. To tackle these obstacles, Sinnokrot and Sherrill employed various computational methods and diverse basis sets to simulate the potential energy curves of the benzene dimer, shown in Figures 5 and 6 [11].

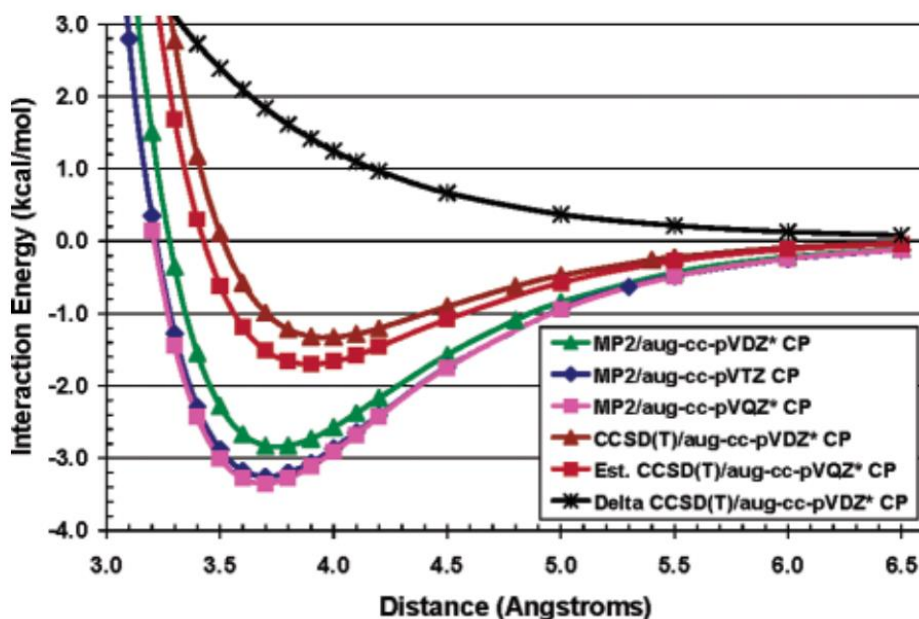


**Figure 5.** MP2 and CCSD(T) potential energy curves for the sandwich configuration of the benzene dimer using counterpoise (CP) correction [11].

The MP2 method with different basis sets (aug-cc-pVTZ, aug-cc-pVQZ, and aug-cc-pVDZ) was used to study the equilibrium distances between the monomers and the interaction energies of the dimer. The curves of aug-cc-pVTZ and aug-cc-pVQZ (shown in Figure 5) showed almost identical behavior. The aug-cc-pVDZ curve was parallel to the other curves but resulted in a slightly larger gap. Comparison of the basis sets showed that the aug-cc-pVTZ basis set stabilized the dimer at the respective minima compared to the aug-cc-pVDZ basis. The interaction energies differed by more than 1 kcal.mol<sup>-1</sup> at shorter intermonomer distances ( $\leq 3.2$  Å). The base aug-cc-pVQZ provided an additional stabilization compared with aug-cc-pVTZ at the corresponding minima and

at shorter distances. This indicates that the high-quality MP2/aug-cc-pVQZ potential energy curves approach the limit of the full basis set at the MP2 level [11].

The CCSD(T) potential energy curve was computed using the aug-cc-pVDZ basis set. By adding the  $\Delta$ CCSD(T) correction to the MP2/aug-cc-pVQZ results, an estimate of the CCSD(T)/aug-cc-pVQZ potential energy curve was obtained. The  $\Delta$ CCSD(T) correction showed significant differences at smaller intermonomer distances, remaining substantial even at the estimated CCSD(T)/aug-cc-pVQZ equilibrium geometry. This confirmed previous findings that MP2 tends to overestimate the binding compared to CCSD(T) calculations [11].

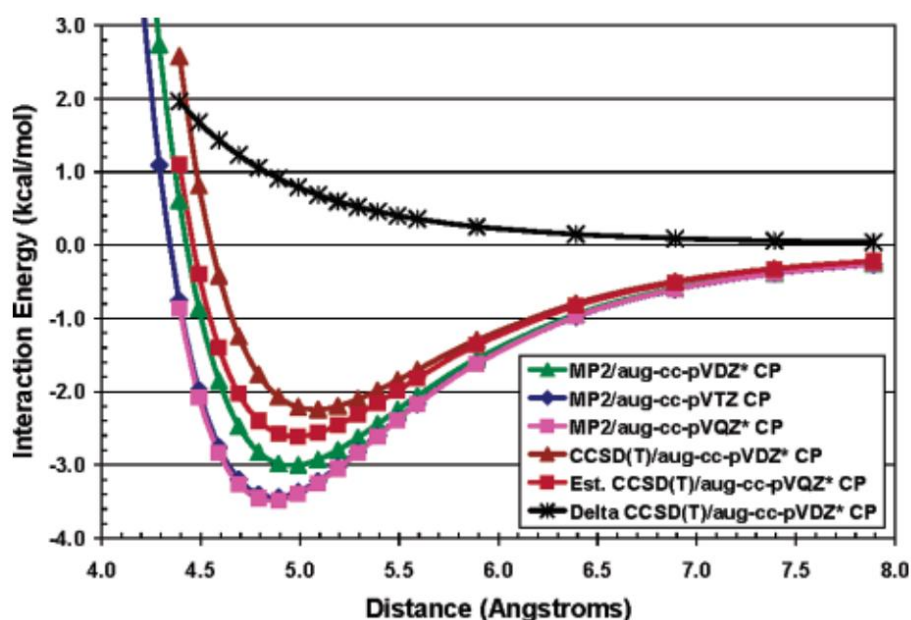


**Figure 6.** MP2 and CCSD(T) potential energy curves for the T-shaped configuration of the benzene dimer, using counterpoise (CP) correction.  $\Delta$ CCSD(T) denotes the difference between CCSD(T) and MP2 [11].

The potential energy curves (PECs) for the T-shaped configuration of the benzene dimer are shown in Figure 6, along with the  $\Delta$ CCSD(T) correction. At the MP2 level, it can be observed that the aug-cc-pVDZ, aug-cc-pVTZ, and aug-cc-pVQZ curves show nearly parallel behavior, leading to similar equilibrium distances between the monomers in the range of 5.0-4.9 Å. It is noteworthy that the aug-cc-pVTZ and aug-cc-pVQZ curves are practically indistinguishable from each other in the Figure. Examination of Figure 6 shows that the aug-cc-pVTZ basis at the MP2 level provides a higher stabilization of the dimer compared to the aug-cc-pVDZ basis at their respective minima, with a larger difference in binding energies at shorter distances. Moreover, the aug-cc-pVQZ basis

stabilizes the dimer only slightly compared to the aug-cc-pVTZ basis at equilibrium, indicating the close approximation of the MP2/aug-cc-pVQZ curves to the boundary of the complete basis set at the MP2 level [11].

At the CCSD(T)/aug-cc-pVDZ level of theory, the benzene dimer has equilibrium distances of 5.1 Å between its monomers, whereas at the estimated CCSD(T)/aug-cc-pVQZ level, the equilibrium distance is 5.0 Å. This agreement between the CCSD(T) and MP2 equilibrium geometries is consistent with the observations for the sandwich dimer, where the CCSD(T) equilibrium distances consistently exceed the MP2 values. The  $\Delta$ CCSD(T) correction is significant for intermonomer distances smaller than the equilibrium distance, reaching about 2 kcal.mol<sup>-1</sup> at R = 4.4 Å. For the estimated CCSD(T)/aug-cc-pVQZ equilibrium geometry,  $\Delta$ CCSD(T) is 0.79 kcal.mol<sup>-1</sup>, compared to a larger value of 1.42 kcal.mol<sup>-1</sup> for the sandwich configuration of the benzene bucket (Figure 5). The smaller importance of the higher order terms in the electron correlation for the T-shaped configuration is consistent with the decreased overlap between the monomers in this geometry [11].

It is noteworthy that the discrepancy between CCSD(T)/aug-cc-pVDZ and the estimated CCSD(T)/aug-cc-pVQZ\* values is more than one kcal.mol<sup>-1</sup> for smaller R, about 0.4 kcal.mol<sup>-1</sup> at equilibrium (R = 5.0 Å) and less than 0.1 kcal.mol<sup>-1</sup> for R > 6 Å [11].

## Aromatic interactions in the liquid phase

In theoretical studies of complex and extended systems, classical molecular dynamics (MD) and Monte Carlo (MC) simulations are often used because of their computational efficiency. To accurately characterize weak intermolecular interactions, particularly the  $\pi\cdots\pi$ -interactions observed in DNA and proteins, it is critical to establish a robust force field qualification procedure.

Extensive studies have been performed on molecular clusters containing benzene, a representative  $\pi$ -aromatic molecule, to uncover the effects of intermolecular aromatic  $\pi\cdots\pi$ -interactions on cluster structures and physicochemical properties. While numerous experimental and theoretical studies have investigated the stability of various configurations of benzene dimers in the gas phase, further understanding of  $\pi$ -aromatic

interactions in condensed matter has required exploration of the structure of aromatic molecular liquids.

In response to this essential need, Cen-Feng Fu and Shan Xi Tian undertook research to elucidate the characteristics of aromatic molecular liquids [12]. Despite the extensive use of MD and MC methods employing various force fields, it remains difficult to determine the optimal force field for accurately capturing the structural and thermodynamic properties of liquid benzene. Numerous studies have been conducted using different force field parameterizations to probe the behavior of liquid benzene. However, the lack of consensus among these studies highlights the complexity and challenges associated with accurately modeling the complicated interactions and dynamic behavior of liquid benzene. [12].

Despite this, Headen *et al.* obtained a full six-dimensional spatial and orientational picture of liquid benzene by means of high-resolution neutron diffraction and empirical potential structure refinement simulations [12,13].

According to their findings, the authors note that the first shell of neighboring molecules exhibits a nearly isotropic nature. At distances below 0.50 nm, the preferred nearest neighbor arrangement is the parallel displaced (PD) configuration, while at larger distances above 0.50 nm, the predominant configuration is the perpendicular Y-shaped arrangement. It is worth noting that the T configuration, which is considered the most stable configuration for the benzene dimer in the gas phase, is observed only as a saddle point in the liquid state. A visual representation of these configurations can be found in Figure 7 [12,13].

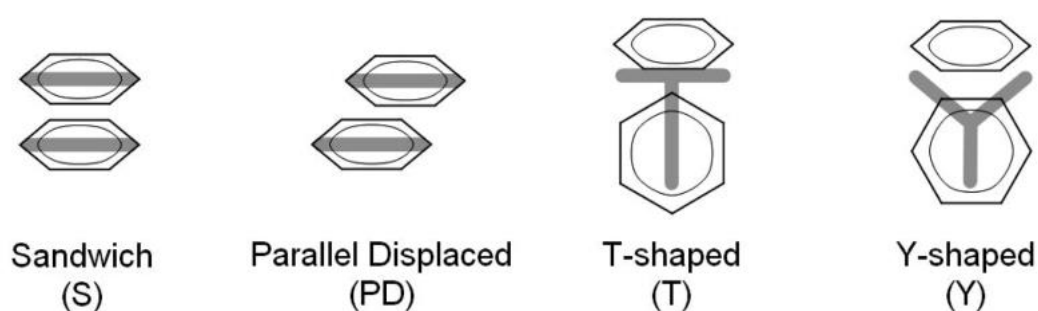


**Figure 7.** Visual representation of the conformations of the benzene dimer: Parallel face-to-face sandwich (S); parallel displaced (PD); perpendicular T-shaped (T); perpendicular Y-shaped (Y) [13].

The authors further emphasize that aromatic molecules such as benzene possess delocalized  $\pi$  electrons that contribute to the presence of a quadrupolar moment. Favorable electrostatic interactions occur when molecules are either in PD or T/Y geometry. In these configurations, the electrostatic interactions compete with attractive dispersion forces, which favor a parallel linear "sandwich" (S) orientation that maximizes molecular contact [13].

Extensive research has revealed intriguing insights into the energetics of the benzene dimer. Previous studies have shown that the PD and T configurations have nearly the same energy, with the latter (T) now recognized as the preferred global minimum. The T interaction, characterized by a shortened donating C-H $\cdots\pi$  bond, has been nicknamed the "anti-hydrogen bond" in recognition of this feature. Moreover, the Y-shaped configuration, characterized by two hydrogen atoms aligned with the aromatic acceptor ring, is in close proximity to the global energy minimum [13,14].

As Sherrill *et al.* noted, a notable result of their research is that of the three configurations (sandwich, T-shaped, and PD), only the PD configuration is identified as a local minimum in the potential energy landscape. However, the global minimum is a slightly tilted T-shaped configuration, with the tilt contributing only minimal additional energy stabilization [15].

## Aromatic interactions in the solid phase

In 1960, a scientific publication documented the formation of a molecular complex between benzene and hexafluorobenzene in the crystal phase [16]. Experimental observations of cooling curves in mixtures of these compounds indicated the formation of a 1:1 complex, which was initially attributed to charge transfer interactions. Surprisingly, no charge transfer band was detected in the UV spectrum. To elucidate the structure of the complex, neutron diffraction experiments were performed that revealed elongated arrays of stacked benzene and hexafluorobenzene molecules in an alternating pattern [4]. X-ray crystallography studies were performed on hexafluorobenzene and various xylenes, leading to the determination of their crystal structures. Remarkably, the interactions observed in these structures resemble those observed in the hexafluorobenzene-benzene complex [4,17].

The stacking of benzene and hexafluorobenzene molecules can be explained by considering their respective quadrupole moments. Benzene has a significant and negative quadrupole moment, while hexafluorobenzene has a large and positive quadrupole moment due to the electronegativity of fluorine. The arrangement of the two molecules in a stacked configuration, observable in Figure 8, maximizes the electrostatic interaction energy by aligning a positive quadrupole moment next to a negative quadrupole moment in a parallel orientation [4,18].

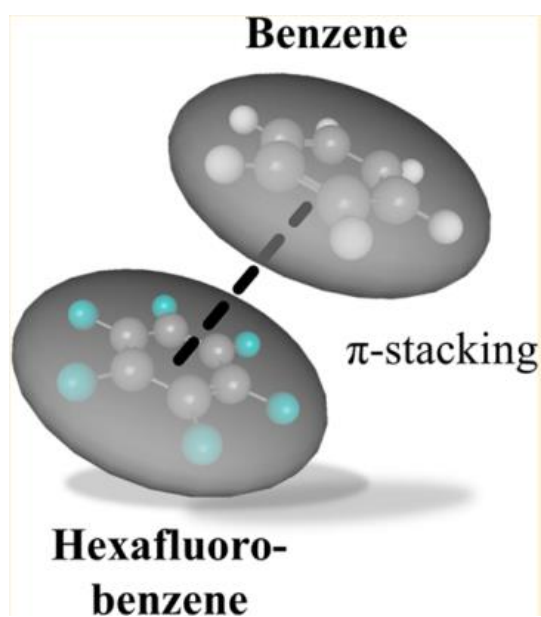


**Figure 8.** The arrangement of benzene and hexafluorobenzene in a stacked configuration [18].

Gautam R. Desiraju and A. Gavezzotti have classified aromatic compounds into four basic packing types, shown in Figure 9. The first type is the simplest herringbone structure with a short axis (s.a.) of 5.4 Å or less and consists of sandwich-like diads arranged in a herringbone motif. In the second type, referred to as sandwich-herringbone packing, the short axis (s.a.) exceeds 8.0 Å. The third type, referred to as "γ", exhibits interactions between translated molecules in parallel, with the short axis (s.a.) between 4.6 and 5.4 Å. The fourth and final type, referred to as "β", is characterized by the presence of "graphitic" planes and a short axis (s.a.) of less than 4.2 Å [19].

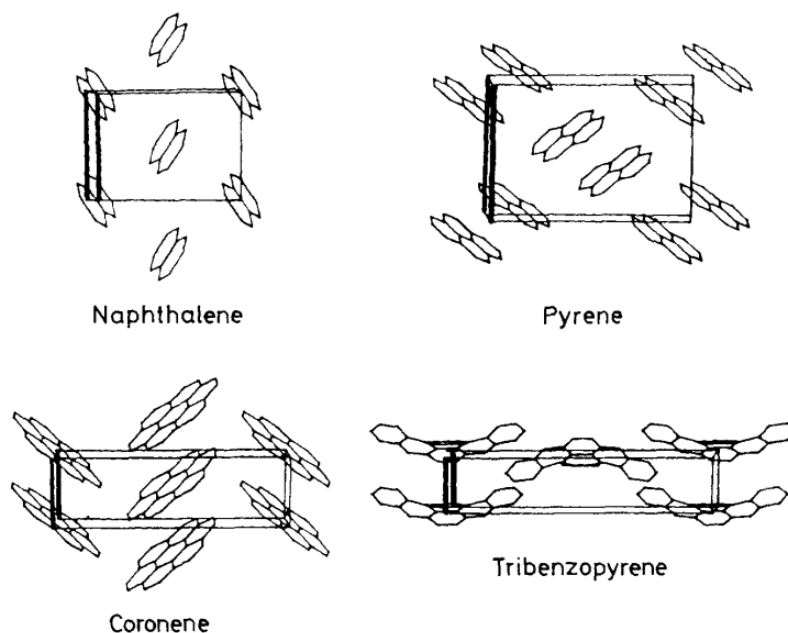


**Figure 9.** The four basic aromatic crystal packings. Naphthalene – herringbone structure; Pyrene – sandwich-herringbone packing; Coronene –  $\gamma$  packing; Tribenzopyrene –  $\beta$  packing [19].

The structural classification of aromatic compounds was supported by energetic considerations. In crystals adopting the sandwich configuration, the interaction energy with a single molecule (called the sandwich partner) is distinct. However, in herringbone,  $\beta$ - and  $\gamma$ -structures, there are always pairs of molecules that have the same cohesive energy with respect to the reference molecule. Moreover, in  $\beta$ - and  $\gamma$ -structures, but not in the herringbone motif, stabilization occurs mainly through interactions with the two nearest neighbors, which are displaced along the short axis [19].

The essential link between molecular and crystal structures lies in the relative ability of a molecule to undergo C-C and C-H interactions. C-C interactions are most favorable when parallel molecules are stacked at van der Waals distances, while C-H interactions are most effective between tilted molecules, possibly due to their presumed coulombic nature. As a result, C-C interactions play an important role in  $\beta$ - and  $\gamma$ -structures, while C-H interactions are crucial for herringbone packing. In sandwich structures, both C-C and C-H interactions are important, highlighting their combined importance [19].

## Aromatic interactions in biomolecules

Aromatic stacking interactions are ubiquitous in nature. A notable example is the phenomenon of base stacking in DNA. This crucial observation was first identified in the seminal structure elucidated by Watson and Crick in 1953 [4].

Both hydrogen bonding and base stacking play crucial roles as stabilizing non-covalent interactions within the double-helical structure of nucleic acids. While hydrogen bonding is relatively simple and well understood, base stacking, despite extensive discussions, is a more complicated phenomenon. Nonetheless, it is clear that base stacking contributes significantly to the stability of DNA and RNA helices [18].

Researchers have used the "dangling end" effect in studies of short RNA duplexes, in which the addition of a single unpaired base at the end of the duplex increases the stability of the helix through stacking interactions. This approach effectively isolates the stacking interaction of a single base from other pairing interactions [20,21]. Although there is consensus on the importance of π-π stacking as a non-covalent interaction in DNA and proteins, its exact nature remains a matter of debate [20].

These interactions include electrostatic effects such as dipole-dipole and dipole-induced dipole interactions, dispersion effects including momentary dipole-induced dipole interactions, and solvation effects, all of which contribute to base stacking stabilization. The electrostatic effects can arise from localized charges in specific regions of a given heterocyclic base or from variations in the electrostatic potentials between the faces and edges of the bases. Dispersion effects, on the other hand, are influenced by the extent of surface contact and the polarizability of the interacting species. In addition, solvent-induced effects, such as solvophobic effects, depend on the relative solvation energies of the stacked and unstacked bases, as well as the extent of desolvation that occurs during stacking, particularly with respect to the surface involved. Together, these various factors affect the energetics and stability of base stacking interactions [20].

For example, studies by Rebek and colleagues have shown that adenine analogs can form complexes with simple aromatic hydrocarbon groups through stacking interactions [22]. Remarkably, it was shown that increasing the size or surface area of such groups led to a significant increase in binding affinity [20]. In parallel, research by Dougherty and co-workers underscored the importance of the negative electrostatic potential in the center of the benzene ring surface for non-covalent interactions [20,23]. Moreover, Siegel's experimental work demonstrated how manipulation of this

electrostatic potential by substituents can modulate the strength of interactions between closely aligned aromatic surfaces [24].

In a study conducted by Kevin M. *et al.*, it was found that dispersion forces, arising from momentary dipole-induced dipole interactions do indeed play a role in the stacking of aromatic systems in aqueous solutions. These attractive forces depend on factors such as the surface area of the overlap, the degree of alignment or contact, and the polarizability of the molecules involved. The researchers also observed a striking correlation between polarizability and stacking free energy. It should be noted, however, that polarizability is affected by size, which in turn strongly influences both hydrophobic and dispersion effects [20].

Permanent electrostatic effects, such as dipole-induced dipole interactions and partial charge interactions, can also affect stacking. While polarizability does not appear to be a dominant factor, permanent electrostatic interactions likely play a role in stacking, especially for natural bases with charge localization. The quadrupolar effect may be important in face-to-face stacking, especially for non-natural bases containing strong electron-donating or -withdrawing groups. Solvent-related effects, such as the hydrophobic effect, are likely to be the dominant factor in most stacking interactions [20].

## Intramolecular interactions

Intramolecular interactions in aromatic systems play an important role in their structure and properties. These interactions occur within a single molecule and involve various forces that affect the conformation and stability of the aromatic system.

The most important aspects of intramolecular interactions in aromatic systems include torsional strain, intramolecular hydrogen bonding, aromaticity, conformational effects, and π-π-stacking. These interactions play a role in the stability of the molecule, its electronic properties, and its reactivity. Understanding intramolecular interactions is essential for studying the behavior and applications of aromatic compounds in various scientific fields.

## Substituents in Aromatic systems

There is a relationship between aromaticity and the substituents. The electronic density of an aromatic system and the integrity of its σ-skeleton are significantly affected by the addition of a substituent. This impact has been a topic of significant interest and study [2].

The substituent can be an atom or a group of atoms with bonds between each other that will substitute hydrogen in the aromatic moiety. The substituent will affect various chemical properties of the aromatic compound. It will affect the chemical bond length, the geometry of the molecules (planarity), chemical reactivity, dipole induction, and consequently aromaticity.

The way the substituents change the properties of aromatic models can be used to better understand the aromaticity of these compounds. The substituent effect is considered to be composed of two components: the resonance and inductive effects. The resonance effect of a substituent is specific to π-electron systems and varies depending on the system to which the substituent is connected. The inductive effect, on the other hand, is universal and acts through both the bonds and the space surrounding the substituent [3].

According to Hunter and Sander's model, the binding energies and equilibrium structures of aromatic complexes can be described primarily by the contributions of  $\sigma \cdots \pi$  attraction,  $\pi \cdots \pi$  repulsion, and Van der Waals forces [1,4].

In a study, made by Cozzi and Siegel and their colleagues, they used substituted 1,8-diaryl naphthalene molecules to determine the rotational barrier of phenyl rings in chloroform by dynamic nuclear magnetic resonance (NMR), as shown in Figure 10. The results obtained are shown in Table 1. The activation energy associated with the isomerism serves as an indicator of the strength of the aromatic interaction between the stacked phenyl rings in the ground state [4,5].

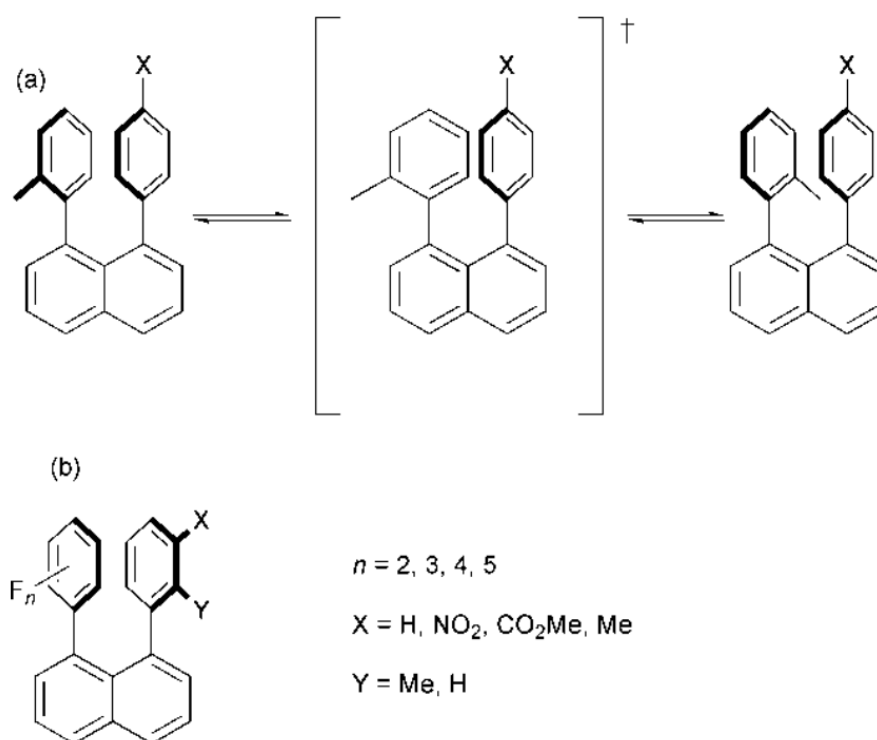


**Figure 10.** (a) A dynamic equilibrium approach was employed to assess the impact of substituents on aromatic stacking interactions between phenyl rings bearing different substitutions ( $X = \text{OMe}, \text{Me}, \text{H}, \text{Cl}, \text{CO}_2\text{Me}, \text{NO}_2$ ); (b) Fluorination of the 1,8-diaryl naphthalene derivatives changes the quadrupole moment of the aromatic ring and consequently the trends in stacking interaction energy [5].

**Table 1.** Barriers to internal rotation in substituted 1,8-diarylnaphthalene molecules (see Figure 10) [4].

Substituent (-X)	$\Delta G^\ddagger$ / kJ·mol <sup>-1</sup>
OMe	58.2
Me	60.2
H	61.5
Cl	64.9
CO <sub>2</sub> Me	70.7
NO <sub>2</sub>	72.4

A correlation was established between the results obtained and the Hammett substituent constants, revealing a linear relationship. This finding suggests that electrostatic effects play a crucial role in this system. In particular, no charge transfer interaction between the phenyl rings was observed by UV spectroscopy. Experimental evidence showed an increase in the barrier upon transition from an electron-donating group to an electron-withdrawing group, indicating the presence of a significant polar  $\pi$ -interaction between the phenyl rings [4].

## Torsional Strain

Torsional strain refers to the energy associated with the distortion or rotation of covalent bonds within a molecule. It arises when adjacent atoms or groups in a molecule attempt to occupy the same space, resulting in repulsive interactions. This strain occurs when dihedral angles deviate from their preferred values, leading to higher potential energy.

In the context of aromatic systems, torsional strain can arise when substituents or functional groups are attached to the aromatic ring. These substituents may introduce steric hindrance or alter the electron distribution within the ring, causing deviations from

the ideal conformation. As a result, the rotation around the carbon-carbon bonds in the aromatic ring becomes energetically unfavorable, leading to torsional strain.

Torsional strain affects the stability and reactivity of aromatic compounds. It can influence molecular conformation, impact electronic properties such as resonance, and affect the ease of rotation or substitution reactions. Minimizing torsional strain is important for maintaining the stability and functional properties of aromatic molecules. Strategies such as appropriate substituent selection or the use of rigid frameworks can help reduce torsional strain and optimize the molecular structure. On the other hand, a certain degree of torsional strain can help in various synthesis methods.

In a study conducted by Xue Zhang and colleagues, the researchers investigated the synthesis of biaryl atropisomers using the transition metal-catalyzed ring-opening approach. They observed that torsional strain plays a significant role in enhancing the reactivity of biaryl atropisomers during the ring-opening process, as shown in Figure 11. This increased reactivity is attributed to a decrease in the activation energy for the ring-opening step, which is achieved by elevating the energy of the ground state of these molecules [25].

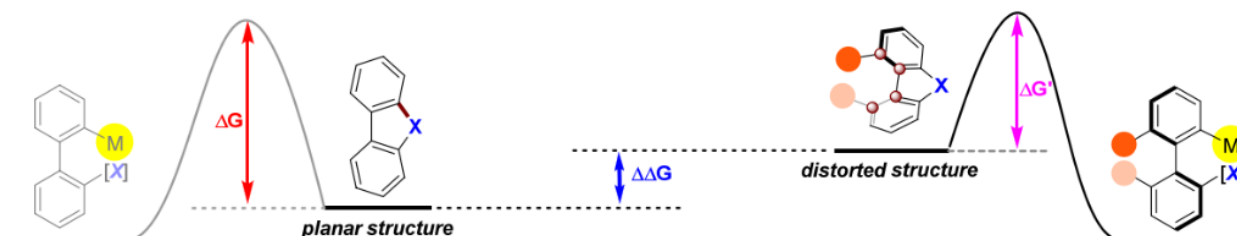


**Figure 11.** Ring-opening strategy for atropisomer synthesis. The increase of torsional strain decreases the amount of energy needed for the ring-opening process [25].

Torsional strain can also be observed in helical chirality, and it refers to the energy penalty associated with the distortion or twisting of a helical structure. Helical chirality is commonly observed in various molecular systems, such as proteins, DNA, and synthetic organic compounds. It is a property of chiral systems that don't contain stereogenic centres, in other words, asymmetric units where four non-equivalent points represent the vertices of a tetrahedron [26].

In these systems, rotation about the helical axis introduces torsional strain that can lead to steric conflicts or unfavorable interactions between adjacent substituents or

functional groups. This strain can disrupt the optimal conformation and stability of the helix and affect its properties and behavior [26].

For non-inherently helical chiral molecules, the introduction of helicity can be achieved through strategic molecular design by incorporating a steric interaction or strain into the planar conformation. This adverse strain forces the molecule to adopt a helical twist that counteracts the torsional strain of the backbone (shown in Figure 12). The magnitude of torsional strain depends on several factors, including the nature and size of the substituents or functional groups, the helix pitch, and the flexibility of the helical backbone. This interaction of forces requires a delicate balance that favors the helical conformation over the planar conformation [26].

Torsional strain in helical chirality can have both structural and energetic implications. It can affect the overall geometry and shape of the helix, leading to distortions or deviations from the ideal helical structure.

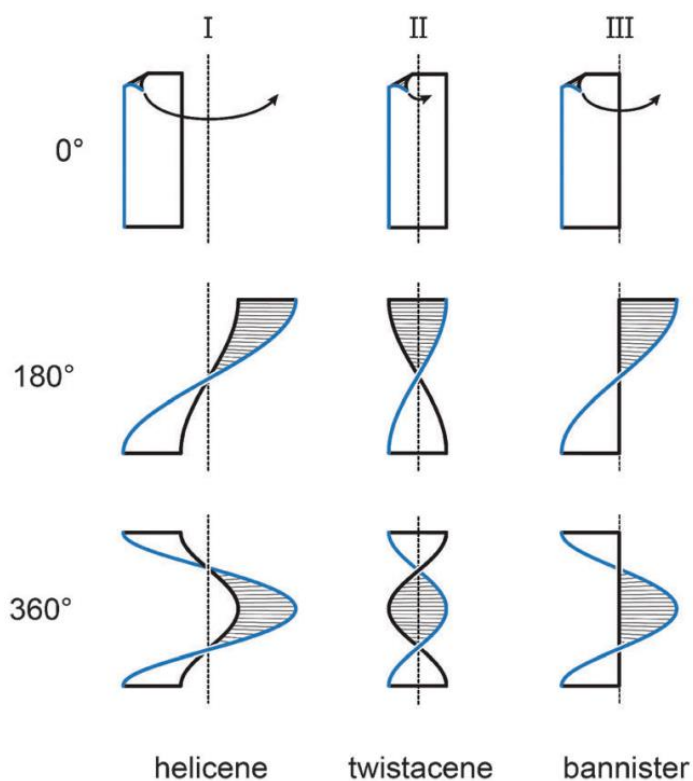


**Figure 12.** Three distinct types of helically twisted ribbons. I) the stereogenic axis doesn't have an intersection with the ribbon (helicene-type); II) the stereogenic axis is identical to the main axis of the ribbon (twistacene-type); III) the stereogenic axis is identical to the black edge of the ribbon (bannister-type). In types I and III, the blue edge is longer than the black one, while in type II, the blue and black edges have the same length [26].

## Intramolecular C-H $\cdots\pi$ interaction

The significance of intramolecular hydrogen bonds is well-established, substantiated by a plethora of physical and chemical evidence. These hydrogen bonds play a substantial role in shaping the structures, influencing the physical properties, and modulating the chemical reactivity of the molecules [27].

Ever since Tamres first observed the energetically favorable interaction between a C-H group and the  $\pi$  system of aromatic compounds, numerous references in the literature have described structures whose properties are attributed to the existence of C-H $\cdots\pi$  bonds. It is believed that the formation of certain stereoisomers in coordination compounds is primarily influenced by these interactions, while they also play an important role in the structure of clathrates and the supramolecular chemistry of certain calixarenes [28].

Other studies have determined that C-H $\cdots\pi$  interactions can play a significant role in defining the crystal structure of some non-inclusion crystals of  $\pi$ -containing molecules [28,29,30]. Thomas Steiner and company found that sufficiently acidic C-H groups with  $\pi$ -bonded acceptor groups possess the essential properties of weak hydrogen bonds [29]. Laxmi Madhavi *et al.* found that these interactions make only small contributions to the crystal binding energy, but they help in defining the structures of solvates [30]. This also happens for crystals of terminal alkynes. C-H $\cdots\pi$  contacts are also thought to be the cause for the existence of herringbone packing motifs in crystals of some aromatic molecules [28].

Theoretical analysis of benzene dimers consistently supports a T-shaped structure, characterized by the perpendicular orientation of the two benzene planes, with an approximate  $C_{2v}$  symmetry [31]. Spectroscopic studies conducted on benzene dimers have provided evidence for the existence of such intermolecular contacts in their T-shaped conformations [28,31].

Despite the recognized importance of these intermolecular interactions, the available information about them in the literature is incomplete and occasionally contradictory. While some NMR studies [32] suggest that C-H $\cdots\pi$  interactions exhibit behavior consistent with hydrogen-bonded systems, other reports have cast doubt on the hydrogen-bonded nature of these interactions based on the lack of an increase in C-H distances in certain C-H $\cdots\pi$  bonds, as typically seen in hydrogen bonds [33]. Equally important is the identification and quantification of these interactions within an aggregate. While this problem is not usually addressed in dimer systems, it is a major challenge in

molecular crystals or aggregates, where the optimal structure is determined by competition between numerous energy potentials [28].

In another study, intramolecular hydrogen bonds in *o*-hydroxyacyl aromatic compounds were explored (Figure 13). A possibility that was raised for the presence of this type of bond is the existence of resonance assisted hydrogen bonding. This type of hydrogen bonding is also found in tautomeric compounds like enolic forms of  $\beta$ -diketones [34,35].

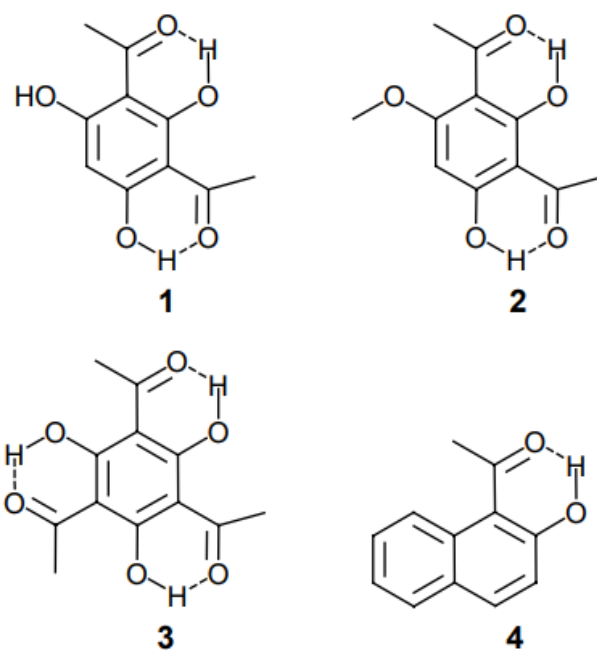


**Figure 13.** *O*-hydroxyacyl aromatic compounds used in the study mentioned [34].

The hydrogen bond, represented by the oxygen-oxygen distance ( $R_{O\cdots O}$ ), serves as an indicator of its strength. Steric compression can influence the  $R_{O\cdots O}$  distance, thereby affecting the hydrogen bond strength [34]. Deuterium isotope effects on chemical shifts have been extensively employed to characterize the strength of hydrogen bonds in intramolecularly hydrogen-bonded systems, and they demonstrate a correlation with the  $R_{O\cdots O}$  distance [34,36].

Steric interactions involving groups such as  $\text{CH}_3\text{C}=\text{O}$ ,  $\text{HC}=\text{O}$ ,  $\text{NO}_2$ , and others, which participate in hydrogen bonding, not only result in a reduction of the  $R_{O\cdots O}$  distance between heavy atoms but can also induce a twist or non-planarity in the group [34]. In the study, the authors observed that in Figure 13, molecules 1 and 2 exhibited shortened

oxygen-oxygen distances. In the case of **1**, these relatively strong hydrogen bonds are nearly coplanar with the aromatic rings, as indicated by a small deviation from planarity measured by the angle between the least-square planes of the aromatic and hydrogen-bonded molecular fragments ( $15.48^\circ$  for O4b-H4bo $\cdots$ O3b H-bond, shown in Figure 14). Additionally, due to their involvement in hydrogen bonding, the carbonyl C=O bonds exhibit increased length ranging from 1.237 to 1.249 Å as compared to acetophenone (1.216 Å) [34,37].

The electron-withdrawing or electron-donating nature of the acyl and hydroxy groups affects the aromatic ring angles, resulting in decreased ipso acyl angles ( $115\text{-}117^\circ$ ) and increased ipso OH angles ( $123\text{-}124^\circ$ ). These changes also influence the aromatic bond lengths, with those involved in the resonance-assisted hydrogen bond (RAHB) becoming longer (above 1.4 Å). A comparison with acetophenone reveals that bond lengths in general are longer in **1**, despite acetophenone also containing an electron-withdrawing group [34,37]. The data obtained for **2**, although less precise due to challenges in obtaining high-quality crystals (as evident from the crystal packing pattern), exhibit similar characteristics [34].

Apart from the hydrogen bonding, the most remarkable feature of **4** is the distortion of the acyl group, which is arranged so that the hydrogen bond O2-H2O $\cdots$ O1 forms an almost coplanar structure with the aromatic fragment. The angle between the optimal planes of the acyl and aromatic fragments was measured to be 24.58 degrees. This discrepancy appears to be due to two causes. The first is intramolecular and involves repulsive, nonbonding interactions between H8 and the methyl hydrogen atoms. The second source is intermolecular and is related to the interactions between the methyl group and the electron density of the neighboring molecule in the crystal lattice of **4**, as depicted in Figure 15 (b,c). The distortion of the molecule is further supported by the torsion angles formed by the atoms of the acyl group, which are about 10-20 degrees. This distortion allows for better co-planarity of the O1 $\cdots$ H2O-O2 hydrogen bond [34].

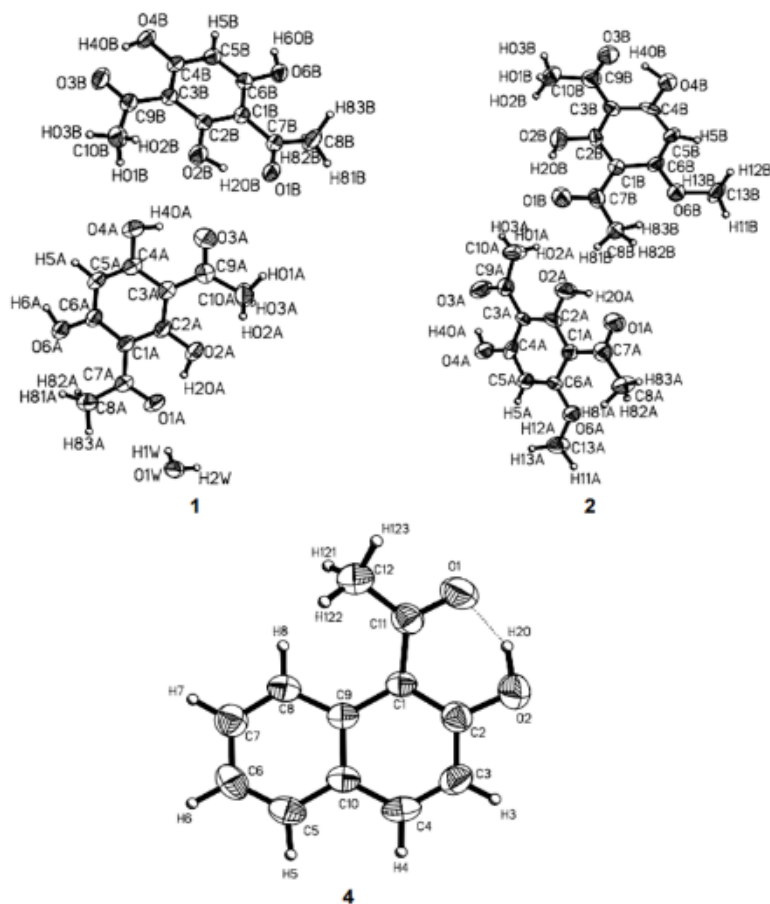


**Figure 14.** Illustration of the labelling of atoms, and the thermal motions of atoms in **1** (a), **2** (b), and **4** (c) are depicted. The numbering schemes for **1** and **2** are derived from the one used for **3** [34].

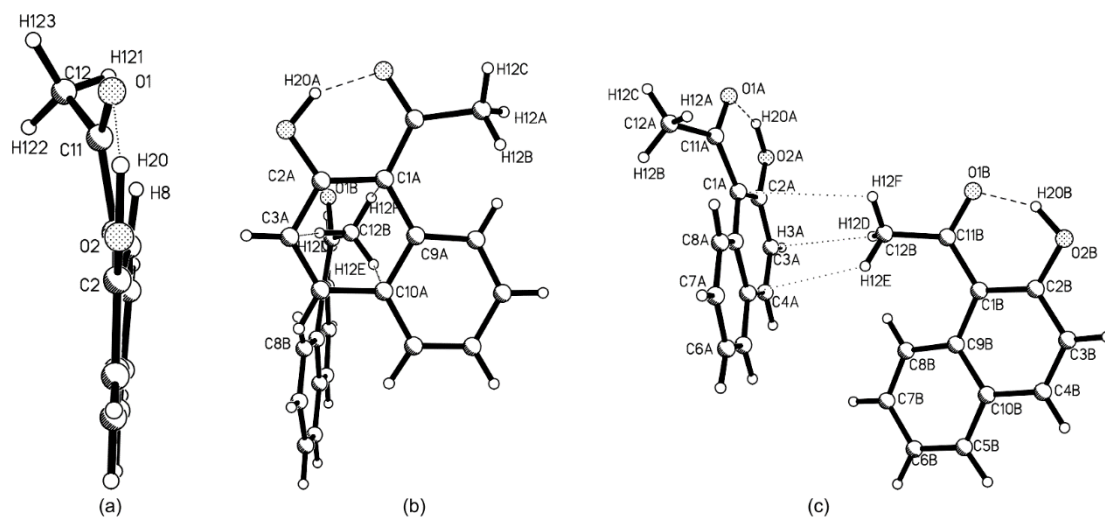


**Figure 15.** (a) The acyl group in **4** exhibits an out-of-plane deformation; (b and c) In the crystal lattice of **4**, there are  $\text{Me}\cdots\pi$ -electron interactions [34].

## Quantification of Aromaticity and $\pi$ - $\pi$ stacking

Aromaticity, resulting from cyclic conjugation, is a fundamental concept in modern organic chemistry. It was originally introduced to explain the stability, reactivity, molecular structure, and other properties of numerous unsaturated cyclic and polycyclic compounds. In addition, aromaticity plays a central role in various reactions in biological systems. Several approaches have been proposed to characterize aromaticity qualitatively and quantitatively, including energetic, geometric, electronic, magnetic, and spectroscopic criteria. Distinguished approaches include magnet-based aromaticity calculations, the harmonic oscillator model of aromaticity index (HOMA), magnetic field-induced current density analysis, electron localization function study, and nuclear independent chemical shift (NICS) determination [38].

In general, aromatic molecules are characterized by having multiple unsaturated carbon atoms and a cyclic arrangement of delocalized  $\pi$ -electrons. The fundamental essence of aromaticity lies in the cyclic delocalization of  $\pi$ -electrons. In contrast, antiaromatic systems exhibit a more localized distribution of electrons within the cycle, which makes them highly unstable. A classic example of an aromatic system is benzene, while cyclobutadiene serves as a prime example of an antiaromatic system [39].

In the field of energetic analysis, isodesmic and homodesmotic reactions serve as common tools for studying aromaticity. In isodesmic reactions, the bond types between reactant and product are matched while maintaining their formal nature (single, double, or triple bond). A representative isodesmic reaction used to study the stabilization of benzene is the bond separation reaction shown in Figure 16 [39].

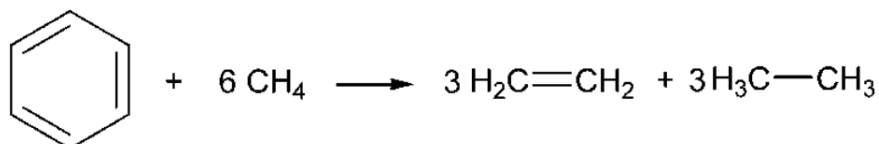


**Figure 16.** Isodesmic reaction to study the stabilization of benzene [39].

Homodesmotic reactions establish a structural correspondence between reactants and products based on the number and type of carbon-carbon bonds and carbon-heteroatom bonds, as well as the number of hydrogen atoms bonded to each carbon atom (C4, C3, and C2) and each heteroatom. As a subset of isodesmic reactions,

homodesmotic reactions emphasize the maximum correspondence of structural elements in reactants and products in terms of the number of formal single, double, and triple bonds. By using homodesmotic reaction schemes, various electronic effects that have an impact on the energetic properties of the molecules under study can be effectively detected and quantified [40,41]. An example of a homodesmotic reaction scheme can be observed in Figure 17. This reaction effectively quantifies the intramolecular interaction between the two phenyl rings in the peri-positions of naphthalene.

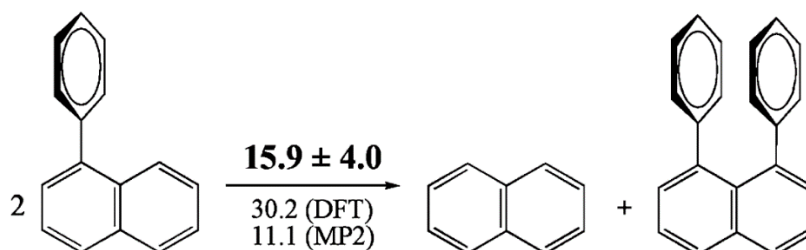


**Figure 17.** Homodesmotic gas phase reaction of 1,8-diphenylnaphthalene to assess the intramolecular aromatic interactions. The reported values, indicated as experimental (in bold), DFT (B3LYP/6-311++G(d,p)), and MP2 (SCS-MP2/cc-pVDZ), represent the corresponding energy values in  $\text{kJ}\cdot\text{mol}^{-1}$  [41].

With respect to interactions between neighboring aromatic rings, it has become customary to refer to these as " $\pi$ -stacking" forces or " $\pi$ - $\pi$  interactions". The influential work of Hunter and Sanders introduced a recognized model that provides qualitative guidelines for understanding and predicting aromatic-aromatic interactions [43]. These guidelines are based primarily on assumptions about polarized  $\pi$  systems and electrostatic considerations. Other authors have also recognized that aromatic rings have a  $\pi$  electron density that leads to a quadrupole moment with partial negative charge over both sides and partial positive charge around the periphery. When two such quadrupole moments are close together, they tend to favor perpendicular edge-to-face interactions or off-centered parallel stacking over face-centered parallel stacking. The terms " $\pi$ -stacking" and " $\pi$ - $\pi$  interactions" may imply face-centered stacking, but the actual interactions involve more complex configurations [42,43].

According to Hunter and Sanders, the strength of the  $\pi$ - $\pi$  interaction between porphyrins is influenced by the metallicity of the porphyrin molecule. The presence of a metal atom increases the magnitude of the interaction but does not change its geometry.

The degree of intramolecular polarization between the porphyrin and the metal directly affects the strength of the  $\pi$ - $\pi$  interaction between two porphyrin molecules. On the other hand, when the metal is coordinated by a ligand, the strength of the  $\pi$ - $\pi$  interaction in metalloporphyrins is reduced, often leading to disaggregation. It is worth noting that the  $\pi$ - $\pi$  attractions of porphyrins are not limited to self-aggregation;  $\pi$  stacking interactions are also observed between porphyrins and various covalently bound  $\pi$  systems in organic solvents. In particular, the presence of zinc enhances this interaction [43].

In a general context, the interaction energy between two molecules can be expressed as follows:

$$E_{total} = E_{electrostatic} + E_{induction} + E_{dispersion} + E_{repulsion} \quad \text{Eq. 2}$$

In their studies, Hunter and Sanders overlooked certain factors such as short-range effects and induction [43]. They emphasized that the primary contributions to the interaction energy come from electrostatic and van der Waals components, while induction plays a secondary role as a second-order term. When considering the apparent energy of interaction between two molecules in a solution, it includes both the association of the molecules and the displacement of the solvent. In nonpolar organic solvents, the electrostatic interactions with the solvent are minimal, so the association energy is the dominant electrostatic interaction. Nevertheless, both the association and desolvation energies are likely to involve significant van der Waals interactions [43].

The authors explain that the interactions between  $\pi$ -systems polarized by heteroatoms have certain features. According to their findings, the face-to-face stacking configuration is preferred due to van der Waals interactions and solvophobic effects. However, this configuration is generally hindered by  $\pi$ - $\pi$  repulsion. It is worth noting that the presence of strongly polarizing atoms significantly affects the electrostatic interaction [43]. When both atoms have high charges, it means that like polarizations repel each other, while unlike polarizations attract. For neutral atoms in this configuration, the primary interaction is governed by  $\pi$ -electron repulsion, so a  $\pi$ -acceptor atom stabilizes the interaction by decreasing the repulsion. On the other hand, a  $\pi$ -donor atom would further destabilize the interaction [43].

In general, experimental and computational works agree that the interaction energy between two benzene rings, in either the parallel displaced or T-shaped configurations, is in the order of  $12 \text{ kJ} \cdot \text{mol}^{-1}$  [1,11,14,15,33,41].

## Electron Correlation

The electron correlation has been a widely studied topic within the scientific literature, with numerous studies and papers published throughout the past century and continuing into recent literature. In quantum chemistry, the correlation energy refers to the energy discrepancy of the Hartree-Fock wavefunction, which is the deviation between the Hartree-Fock limit energy and the accurate resolution of the nonrelativistic Schrödinger equation [44]:

$$E_{corr} = \varepsilon_{exact} - E_{HF}^{\infty} \quad \text{Eq. 3}$$

The  $E_{corr}$  is the correlation energy,  $\varepsilon_{exact}$  being the exact energy and  $E_{HF\infty}$  being the Hartree-Fock energy for a molecular system using a complete basis set.

In quantum chemistry, different types of electron correlation are often classified, encompassing dynamic and non-dynamic variations, radial and angular correlation for atoms, left-right, in-out, and radial correlation for diatomic molecules, and weak and strong correlation for solids [44].

The widely recognized categorization of electron correlation types is based on dynamic and non-dynamic electron correlation.

A method is said to be dynamically correlated if its wavefunction, as determined by a configuration interaction (CI) expansion, contains primarily a single dominant configuration, with other configurations making only minor contributions. In contrast, nondynamic correlation occurs when there are two or more important configurations, typically in scenarios with degeneracies or near-degeneracies. Non-dynamic correlation is considered a contribution that is specific to the system in question, while dynamic electron correlation is generally considered a more universal factor [45].

In dynamic correlation, the tightly bound electron pair, as seen in the closed-shell helium configuration, exhibits a distinct electronic arrangement. In this state, the electrons are paired and form a representative electronic configuration. In this correlation type, there is no single configuration within the CI wavefunction that strongly interacts with the HF configuration, leading to gradual CI convergence [46].

Dynamic correlation methods describe electronic correlation by considering the effects of electron-electron repulsion beyond the mean-field approximation used in Hartree-Fock theory. In dynamical correlation methods, the electronic wavefunction is extended in terms of determinants that include excited states of the system. This extension allows the inclusion of nonlocal electron correlation effects that cannot be accounted for when using wavefunctions with only one determinant [46]. Dynamic correlation methods, such as configuration interaction and coupled cluster methods, are among the most accurate approaches for describing electronic correlation in molecules.

Non-dynamic correlation involves a reduction in energy due to the interaction between the HF configuration and lower-lying excited states. This phenomenon occurs in a nearly degenerate state and can be accurately calculated by diagonalizing the corresponding secular matrix [46].

Static correlation methods are used to describe electronic correlation in molecular systems where the wavefunction contains significant contributions from more than one electronic configuration. This is in contrast to dynamic correlation methods, which are used to describe correlation effects arising from the movement of electrons between orbitals [46].

Mok, Neumann and Handy defined the nondynamical correlation energy (NDCE),  $E_{ND}$ , as [46]:

$$E_{ND} = E_{CASSCF} - E_{HF} \quad \text{Eq. 4}$$

$E_{CASSCF}$  stands for the energy of a complete active space self-consistent field (CASSCF), while  $E_{HF}$  stands for the energy of Hartree-Fock.

The presence of near-degeneracy correlation plays a crucial role in the accurate dissociation of a molecule into its individual atoms. This is evident from the fact that molecular orbitals can be described as linear combinations of atomic orbitals. Such correlation effects extend over long distances and cause electrons to disperse to individual atoms as the molecule dissociates. An illustrative example of this behavior can be observed in the  $H_2$  molecule [46].

Since the dynamic correlation energy (DCE),  $E_D$ , must be such that:

$$E_{corr} = E_D + E_{ND} \quad \text{Eq. 5}$$

Then

$$E_D = E_{corr} - E_{ND} \quad \text{Eq. 6}$$

The definition of DCE is possible only after NDCE has been defined. Subsequently, it becomes clear that DCE is a short-range effect characterized by the decrease of the repulsion energy when two electrons approach each other, leading to a decrease of the wavefunction expectation value [46].

Understanding dynamic correlation in aromatic systems is critical for accurately describing and predicting aromatic interactions. Aromatic interactions, such as π-π stacking, are driven by the movement of electrons within aromatic rings. Dynamic correlation accounts for electron mobility and fluctuations in electron distribution, which play a crucial role in dispersion forces, an important component of aromatic interactions.

## Applications of 1,8-diarylanthracenes

Recently, interest in anthracene derivatives has increased significantly due to their versatility in various chemical, and photophysical. Moreover, anthracene derivatives, which are characterized by high fluorescence quantum yield and robust chemical photostability, have a valuable role in the field of organic light-emitting diodes (OLEDs) [47]. However, it should be noted that unsubstituted anthracenes have remarkably low fluorescence quantum yield and tends to crystallize in the form of thin films, limiting its utility in solid-state devices [47].

Derivatives of anthracene, specifically 1,8-diarylanthracenes (Figure 18), exhibit mechanofluorochromic properties. Mechanofluorochromic materials change their emission color in response to mechanical perturbations like compression, grinding, or crushing and have garnered significant attention due to their potential applications in fields such as sensors, memory chips, and security inks [48].

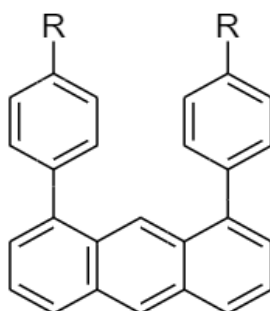


**Figure 18.** Visual representation of 1,8-diarylanthracene.

Unlike other organic mechanochromic compounds, which often have complicated structures requiring multiple synthetic steps to prepare, 1,8-diarylanthracenes have a distinct advantage due to their simpler structure and ease of synthesis through the Suzuki-Miyaura cross-coupling reaction [48]. This inherent simplicity makes them highly desirable compounds. Moreover, the mechanochromic luminescence of an organic fluorophore is usually attributed to the phase transition between the crystalline and amorphous states. In this regard, 1,8-diarylanthracenes offer an even greater advantage, as this phase transition is associated with changes in molecular packing modes (such as  $\pi$ - $\pi$  stacking) and intramolecular planarity (conformational changes and adjustments

in  $\pi$ -conjugation). These specific features of anthracene contribute significantly to its mechanofluorochromic properties [48].

## Objective

A previous experimental and computational study of 1,8-diarylnaphthalenes (Figure 19) aimed to elucidate the relationship between their structure and energetics [41]. The results indicated a pronounced presence of repulsive interactions between the substituents and torsional strain, primarily due to their extremely close distance ( $\sim 3.0$  Å). This proximity prevented the formation of significant  $\pi$  interactions between the substituents, which ultimately led to the destabilization of the molecules.

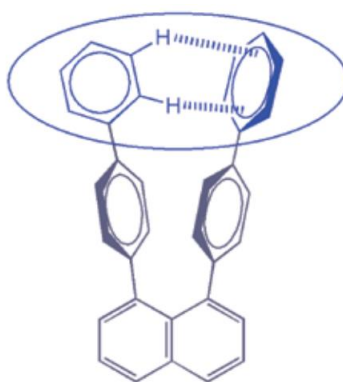


**Figure 19.** Visual representation of a 1,8-diarylnaphthalene, in this case 1,8-di([1,1'-biphenyl]-4-yl)naphthalene [41].

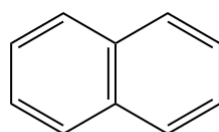
Considering the previous results, it was decided to increase the distance between interacting groups ( $\sim 5.1$  Å) and conduct a similar study but to various 1,8-diarylanthracenes (Figure 18) (R = H, OCH<sub>3</sub>, CHO, Phenyl).

Through a combined experimental and computational thermodynamic investigation, this thesis endeavors to uncover the impact of distance on the strength of aromatic interactions, while also exploring the potential influence of additional interactions on aromatic systems.

## Compounds Studied

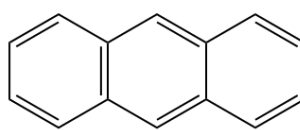
In the field of aromatic systems, especially in the context of substituent effects, fascinating phenomena occur when different substituents interact. These effects can vary depending on the specific aromatic system and the nature of the substituents involved. The resulting effects on the stability of the molecule, phase behavior, electrical charge conductivity, and molecular energetics can either amplify or attenuate, adding a dynamic dimension to the complicated interplay.

To better understand these behavioral changes, a number of aromatic molecules that can be readily modified and juxtaposed with a smaller or larger counterpart, such as naphthalene (Figure 20) and anthracene (Figure 21), were studied. The simple configuration of naphthalene and anthracene provides a favorable advantage and allows comparison of interactions between substituents in disubstituted naphthalene and disubstituted anthracene. The basic requirement is that the substituents in both aromatic molecules must be identical to ensure a valid and accurate comparison.



naphthalene

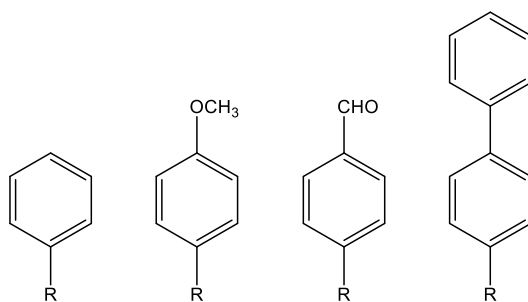
**Figure 20.** Visual representation of naphthalene.



anthracene

**Figure 21.** Visual representation of anthracene.

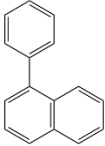
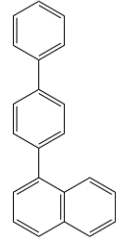
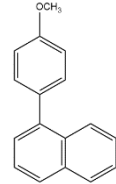
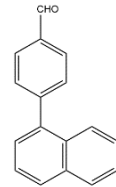
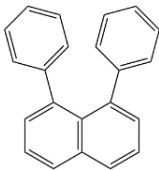
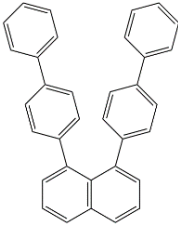
In this study, various types of substituents were selected to replace the core molecules. Despite their differences, these substituents share commonalities as they are derived from phenyl and biphenyl groups. In Figure 22, the substituents studied are shown.



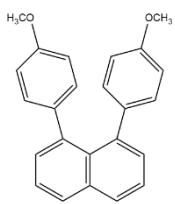
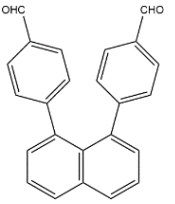
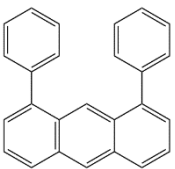
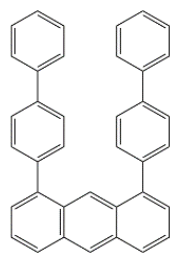
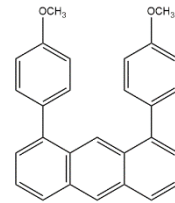
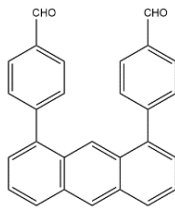
**Figure 22.** From the left to the right: phenyl; 4-methoxyphenyl; 4-formylphenyl; biphen-4-yl group.

Table 2 showcases the compounds studied, which are formed when incorporating the substituents illustrated in Figure 22 into the naphthalene and anthracene frameworks [1,41]. Since the naphthalene derivatives were already reported in the literature, the experimental studies were focused on the anthracene compounds.

**Table 2.** List of the compounds studied in this work. Throughout this dissertation, the abbreviations shown will be used instead of the IUPAC names. The naphthalene derivatives are already reported in the literature. The anthracene derivatives were subjected to experimental and theoretical studies.

IUPAC name	Abbreviation	Molecular Formula	Structural formula
1-phenylnaphthalene	1-PhNaph	C <sub>16</sub> H <sub>12</sub>	
1-([1,1'-biphenyl]-4-yl)naphthalene	1-biPhNaph	C <sub>22</sub> H <sub>16</sub>	
1-(4-methoxyphenyl)naphthalene	1-methoxyPhNaph	C <sub>17</sub> H <sub>14</sub> O	
4-(naphthalen-1-yl)benzaldehyde	4-Naph-1-BenzAl	C <sub>17</sub> H <sub>12</sub> O	
1,8-diphenylnaphthalene	1,8-diPhNaph	C <sub>22</sub> H <sub>16</sub>	
1,8-di([1,1'-biphenyl]-4-yl)naphthalene	1,8-dibiPhNaph	C <sub>34</sub> H <sub>24</sub>	

**Table 2.** Continued.

1,8-bis(4-methoxyphenyl)naphthalene	1,8-bismethoxyPhNaph	$C_{24}H_{20}O_2$	
4,4'-(naphthalene-1,8-diyl)dibenzaldehyde	4,4'-Naph-1,8-diBenzAl	$C_{24}H_{16}O_2$	
1,8-diphenylanthracene	1,8-diPhAnth	$C_{26}H_{18}$	
1,8-di([1,1'-biphenyl]-4-yl)anthracene	1,8-dibiPhAnth	$C_{38}H_{26}$	
1,8-bis(4-methoxyphenyl)anthracene	1,8-bismethoxyPhAnth	$C_{28}H_{22}O_2$	
4,4'-(anthracene-1,8-diyl)dibenzaldehyde	4,4'-Anth-1,8-diBenzAl	$C_{28}H_{18}O_2$	

## Experimental Techniques

To reach the goal of this dissertation, various methods and techniques were utilized to better understand the compounds studied.

Some were used for the synthesis and characterization of the compounds:

- Suzuki-Miyaura cross-coupling reaction.
- Purification by sublimation under reduced pressure.
- Gas Chromatography.
- Fourier-transform Infrared Spectroscopy.
- UV-Vis Spectroscopy.

Others were used with the objective to better understand the thermodynamical properties of the compounds:

- Differential Scanning Calorimetry.
- Knudsen-Quartz Crystal effusion.
- Mini-bomb Combustion Calorimetry.
- Quantum Chemistry Calculations.

### Suzuki-Miyaura Cross Coupling Reaction

The Suzuki-Miyaura reaction (SMR), in which an organoboron reagent and an organic halide or pseudohalide are brought together with the aid of a palladium or nickel catalyst and a base, has undoubtedly proven to be one of the most widely used

techniques for the preparation of robust C-C bonds. In the field of C-C bond catalytic formation, the Suzuki-Miyaura reaction is a prominent and widely used category [49,50].

The reaction proceeds via a catalytic cycle of oxidative addition, transmetalation, and reductive elimination, with the use of electron-donating and sterically imposing ligands facilitating the initial and final phases. The distinct advantages over alternative palladium-catalyzed cross-coupling reactions are [50,51]:

- Operation under mild reaction conditions.
- Easy accessibility of organoboron reagents, which are also resistant to water, other solvents, and oxygen, and usually exhibit thermal stability.
- Tolerance to various functional groups.
- Preparation from easily accessible starting materials and generation of byproducts with low toxicity.

Irrespective of the conditions applied in each cross-coupling reaction, a common fundamental reaction mechanism is a prevailing characteristic among these reactions. The widely acknowledged cross-coupling reaction mechanism is illustrated in Figure 23. The Suzuki-Miyaura reaction is a unique type of cross-coupling reaction, where the [ct] = Pd and M = B (boron). In this manner, this process leads to the coupling of an organometallic boron compound, R-[B], with an organic electrophile, R'-X, under the influence of a Pd catalyst and a base, resulting in the formation of a new C-C bond.

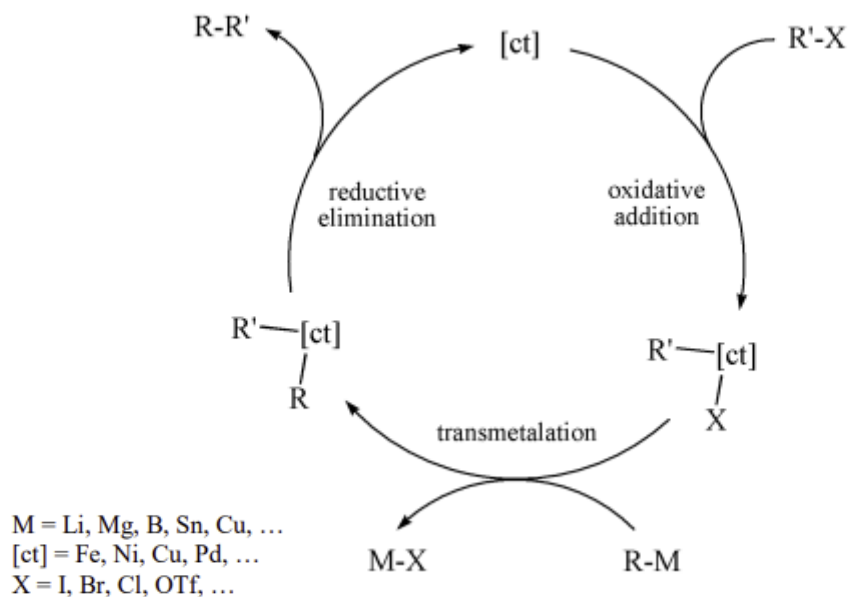


**Figure 23.** Schematic of the widely accepted mechanism of C-C cross-coupling reactions.

The broadly acknowledged catalytic cycle for the Suzuki coupling reaction encompasses four primary stages, as shown in Figure 24.

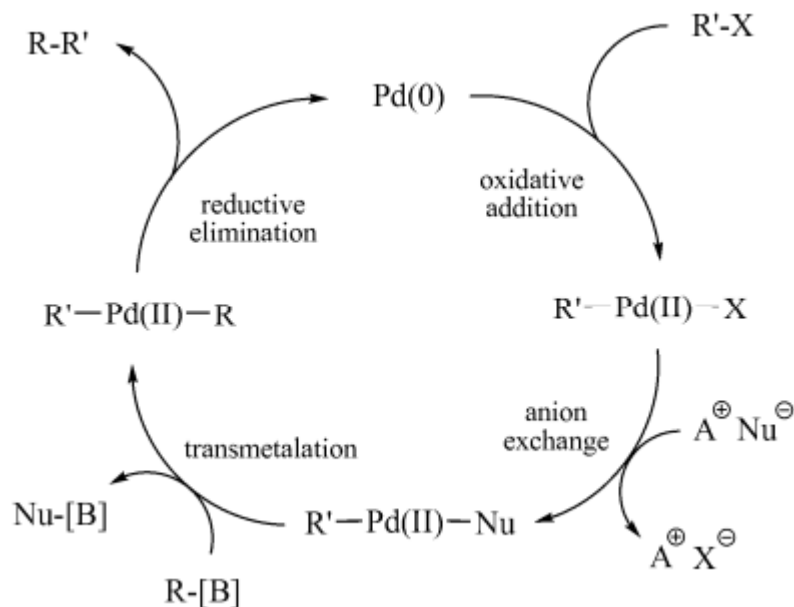


**Figure 24.** Schematic of the widely accepted reaction mechanism for the Suzuki-Miyaura cross-coupling reaction.  $A^+$  and  $Nu^-$  stands for, respectively, a cation and a nucleophile.

In cross-coupling reactions, especially in Suzuki coupling, the use of Pd is most commonly achieved by Pd(0)-organometallic complexes such as  $\text{Pd}(\text{PPh}_3)_4$  and its variants.  $\text{PPh}_3$  here stands for a monovalent triphenylphosphine ligand. In addition, organometallic Pd(II) complexes such as  $\text{PdCl}_2(\text{dppe})$  and  $\text{Pd}(\text{OAc})_2$ , where dppe stands for the divalent 1,2-bis(diphenylphosphino)ethane ligand, are frequently used. The Pd(0) complexes used typically belong to the category of coordinatively saturated  $\text{Pd}(0)\text{L}_4$  species, where L stands for a general ligand. These can dissociate in solution and transform into unsaturated  $\text{Pd}(0)\text{L}_2$  complexes. These have unoccupied sites available for complex formation, which makes them reactive in oxidative addition. Pd(II) complexes exhibit comparable catalytic efficiency because they are resistant to air and are readily reduced to active  $\text{Pd}(0)\text{L}_2$  species in solution.

The entirety of the compounds studied in this dissertation were synthesized by the application of the Suzuki-Miyaura cross-coupling reaction.

## Purification by sublimation under reduced pressure

Upon the synthesis of the compounds, a purification process became imperative to eliminate impurities. Notably, among these impurities was *p*-quaterphenyl (shown in Figure 25), in the synthesis of 1,8-dibiPhAnth (resulting from the homocoupling of 4-biphenylboronic acid).

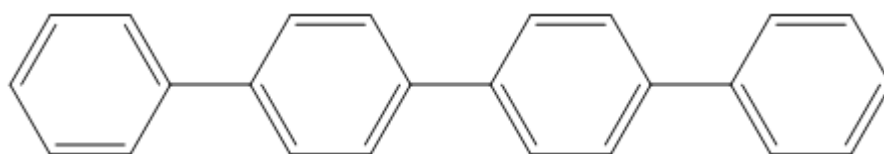


**Figure 25.** Schematic representation of 1,1':4',1'':4'',1''':4''',1''''-quaterphenyl (*p*-quaterphenyl).

Additional impurities, stemming from the reagents employed in the synthesis, were readily eliminated through liquid-liquid extraction and sublimation under elevated temperatures and low pressure. However, *p*-quaterphenyl emerged as a particularly stubborn impurity, requiring multiple rounds of purification to successfully separate it from 1,8-dibiPhAnth.

A low-pressure sublimator was used to assist in this purification process (shown in Figure 26). This sublimator was specially assembled to purify small samples (50-400 mg) of solid compounds. It has a cooling mechanism consisting of two tubes through which water circulates and which are connected to a cold finger. This cold finger is inserted into a glass ampoule containing the substance to be purified. The sublimator is placed in an oven, which is responsible for increasing the temperature of the substance and facilitates sublimation. The sublimator is connected to a vacuum system. At reduced pressure and increased temperatures, the compound sublimates and condenses on the cold finger.

This low pressure sublimator was used to purify all compounds synthesized in this work.



**Figure 26.** Low pressure sublimator used in this work.

## Gas Chromatography

At the heart of the gas chromatographic process is the chromatography column itself. This is a slender tube whose interior is covered with a thin film of liquid. The column serves as a separation medium that allows the components of a mixture to be

differentiated. When the mixture is introduced, a carrier gas, usually helium or nitrogen, flows through the column. This gas carries the components of the mixture through the column. As the components of the mixture pass through the column, partitioning takes place between the stationary phase (liquid-coated inside) and the mobile phase (carrier gas). This partitioning, due to different affinities for the stationary phase and to different volatilities, results in different retention times for each component. After leaving the column, the separated components are detected and quantified. A key element in gas chromatography is precise temperature control. Working at elevated temperatures often ensures efficient separation as the components spend less time in the column [52].

The following Figures (Figure 27 and Figure 28) show a basic schematic of a gas chromatograph and the Agilent 4890D Gas Chromatograph used in this dissertation. This Gas Chromatograph is equipped with a HP-5 column, cross linked, diphenyl (5%), and dimethylpolysiloxane (95%), length = 15 m, inner distance = 0.530 mm, film thickness = 1.50 μm, and a FID detector.

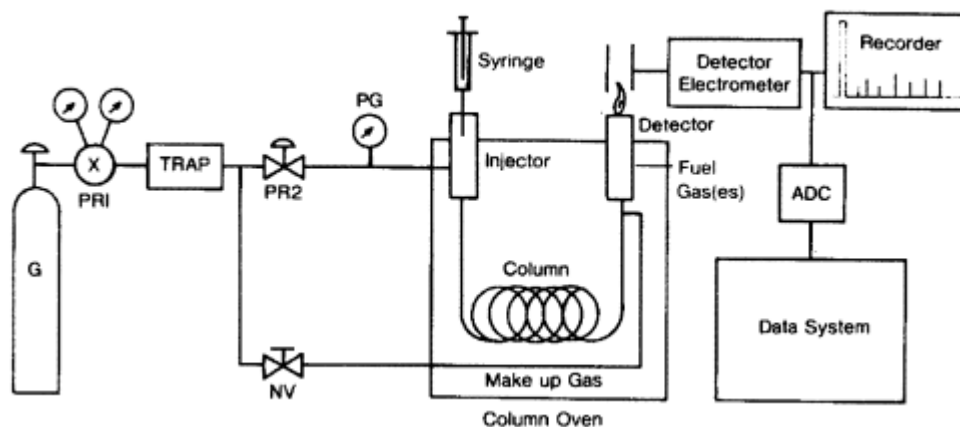


**Figure 27.** Visual representation of a basic schematic of a gas chromatograph [52].



**Figure 28.** Agilent 4890D Gas Chromatograph used in this work.

The purity of the compounds was determined by gas chromatography. It was already established that the desired compounds had longer retention times compared to the impurities. Therefore, checking the purity of the solution by comparing the retention time with that of the compound did not pose much of a challenge. An intriguing case occurred with 1,8-dibiPhAnth. Its remarkably long retention time led to the decision to determine its purity based on the average retention times of other anthracene derivatives. Fortunately, 1,8-dibiPhAnth exhibited negligible impurities.

## Fourier-transform Infrared Spectroscopy

In the field of IR spectroscopy, a sample is exposed to infrared radiation. This radiation comes into contact with the sample through absorption and transmission processes. The result is a spectrum that visually reflects these interactions, creating a unique molecular fingerprint of the sample. This uniqueness is significant because no two molecular structures produce identical IR spectra. This property makes IR spectroscopy an adaptable tool for a wide range of analyses. FTIR spectroscopy has garnered preference for several compelling reasons [53]:

- It preserves sample integrity because it is non-destructive.

- It offers a precise measurement method that not only eliminates the need for external calibration but also contributes to accurate measurements.
- It makes the process faster by acquiring scans at a rate of one per second.
- The improved sensitivity results from the accumulation of scans, reducing the influence of random noise.
- This ensures higher optical throughput.
- Its mechanical simplicity is embodied in a single moving component.

A FTIR spectrometer consists of three basic components: a radiation source, an interferometer, and a detector. The job of the interferometer is to split beams, create an optical path difference between those beams, and then detect interference signals. These signals, quantified by the detector in terms of optical path difference, contain valuable IR spectral data generated as the beam passes through the sample [53,54,55].

The most popular type of interferometer is the Michelson interferometer (Figure 29), which consists of three functional elements: a movable mirror, a fixed mirror, and a beam splitter. The mirrors are arranged at right angles to each other [53,55].

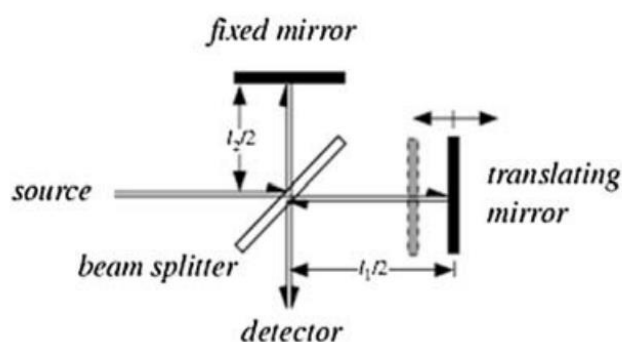


**Figure 29.** Schematic diagram of the components of a Michelson interferometer [53].

The FTIR spectrometer used is a GLADIATR™ FTIR spectrometer (shown in Figure 30). This spectrometer was used to characterize and, in conjunction with gas chromatography, to check the purity of the compounds studied.

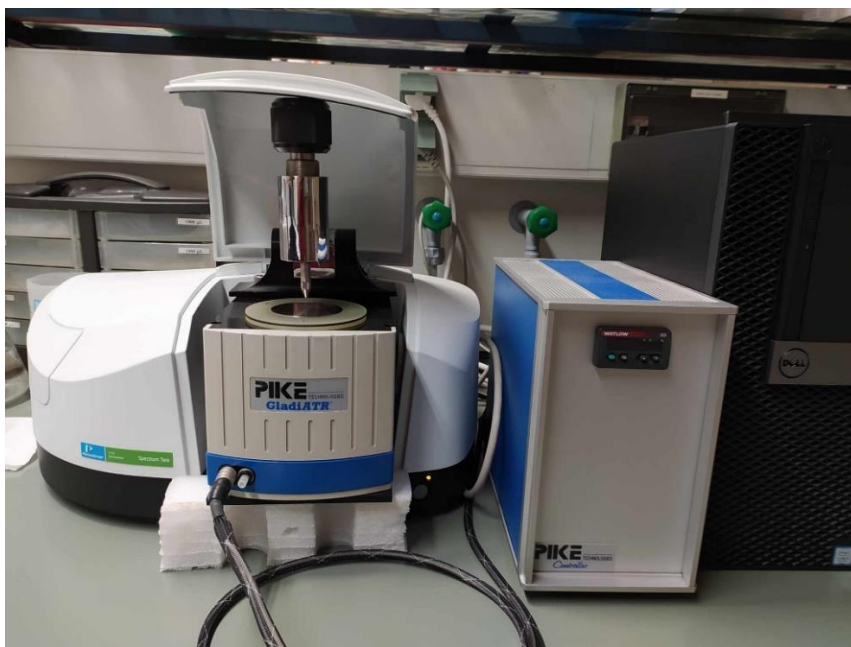


**Figure 30.** GLADIATR™ FTIR spectrometer used in this work.

## UV-Vis Spectroscopy

Ultraviolet-visible spectroscopy analyzes interactions between matter and electromagnetic radiation in the UV and visible range. The UV range is divided into UVA (320-380 nm), UVB (280-320 nm), and UVC (100-280 nm), while the visible range is from 380 to 750 nm. UV-Vis spectroscopy primarily excites the outermost electrons of atoms involved in the formation of molecules, hence it's called "electronic spectroscopy" [56].

When ultraviolet and visible radiation strikes a surface, it can interact with matter through various mechanisms. It can pass through the material, be diffusely transmitted, bounce off the surface, be absorbed, be emitted as photoluminescence (including fluorescence and phosphorescence), or even scatter laterally at wavelengths different from the incident monochromatic radiation due to the Raman effect. When the frequency

of the incident radiation matches the energy difference between two energy levels, the material absorbs that specific frequency, resulting in resonance excitation. This excitation leads to changes in the distribution of electronic density [56].

This effect is represented by the Bohr model:

$$\Delta E = E_2 - E_1 = h\nu \rightarrow h\nu = hc\bar{\nu} = \frac{hc}{\lambda} \quad \text{Eq. 7}$$

Where  $E_1$  and  $E_2$  are the initial and final energies respectively;  $h$  corresponds to Planck's constant;  $\nu$  is the frequency of one photon;  $c$  is the speed of light in vacuum;  $\bar{\nu}$  corresponds to the wavenumber and  $\lambda$  the wavelength.

This phenomenon, as seen in electronic spectroscopy, induces changes in the distribution of electronic density within the outermost orbitals of an individual atom, group of atoms or a molecule. In molecular orbitals, it corresponds to an electronic transition from occupied to unoccupied energy levels. As a result, Bohr's relation establishes a connection between the energy levels of atoms or molecules and the frequency of the incoming radiation [56].

When matter absorbs some of the incident radiation and becomes energetically excited, this state is inherently unstable and causes the substance to return to its original equilibrium state. The return to the ground state is accompanied by "deactivation" processes" that can unfold via various mechanisms: without the emission of radiation (e.g., internal energy conversion leading to thermal equilibrium or heat release), with spontaneous emission of radiation with lower energy compared to the absorbed radiation (fluorescence, phosphorescence), or via photochemical reactions.

Lambert and Beer formulated a relationship linking the intensity of absorption to the concentration and thickness of the absorbing material [56,57]:

$$A = \varepsilon lc = -\log T = \log (1/T) \quad \text{Eq. 8}$$

Where  $A$  corresponds to the absorbance;  $\varepsilon$  corresponds to the molar absorptivity;  $l$  corresponds to the thickness of the sample;  $c$  is the concentration;  $T$  corresponds to the transmittance.

HOMO-LUMO gap energies can be experimentally measured by absorption and reflectance spectroscopy, as well as, by photoconductivity measurements and electrical conductivity techniques. This shows that the UV-Vis absorption study of organic semiconductors can be used as an easy and simple method to evaluate the electronic structure and estimate bandgap energies of organic  $\pi$ -conjugated materials [56].

In this work, the Agilent 8453 UV-Vis Spectrophotometer was used (shown in Figure 31). With this spectrophotometer, a substantial collection of spectra was obtained for the compounds studied, complementing the findings from other studies. Essentially, UV-Vis was used to evaluate the degree of conjugation in the molecules studied.

Temperature control is achieved by means of a circulating water bath Julabo F25



**Figure 31.** Agilent 8453 UV-Vis Spectrophotometer (a) used in this dissertation. The spectrophotometer is linked to a refrigeration system (b) and to a pc interface (c) for data acquisition.

## Differential Scanning Calorimetry

Differential scanning calorimetry (DSC) is a powerful thermoanalytical method that takes advantage of the difference in heat required to raise the temperature of a sample and a reference, which is monitored across different temperatures. In practice, the sample and reference are intentionally kept at equal temperatures, during a DSC analysis. When the experiment begins, both the sample and the reference are exposed

to the same temperature regime. This technique is particularly valuable for understanding thermal properties, phase transitions, and energy change in a material.

In DSC analysis, the sample to be analyzed is positioned in a crucible that is identical in every aspect to the reference crucible. The signal acquired from the reference crucible is subtracted from the signal of the sample, introducing a differential aspect to the methodology. This approach results in a smoother baseline and effectively eliminates confounding factors such as from temperature variations, electrical irregularities, or from humidity variations that are attenuated by signal subtraction. However, despite these efforts, the system remains inherently asymmetric due to discrepancies in the making of the furnace block, placement of temperature sensors, and variations in the crucibles themselves. Therefore, the need for baseline corrections still exists.

DSCs can be divided into two main types based on their operating mechanisms: DSCs with heat flow and DSCs with power compensation.

In a heat flow DSC configuration, a sample material enclosed in a crucible and an empty reference crucible are located on a thermoelectric disk enclosed by a single furnace. The furnace is heated at a uniform rate, and heat transfer to the sample and reference trays is facilitated by the thermoelectric disk. However, due to the heat capacity ( $C_p$ ) of the sample, there is a temperature difference between the sample and reference. This temperature difference is measured by area thermocouples, and the resulting heat flow is determined by the thermal counterpart of Ohm's law [58]:

$$q = \frac{\Delta T}{R} \quad \text{Eq. 9}$$

Where  $q$  is the sample heat flow,  $\Delta T$  is the difference in temperature between the sample and reference, and  $R$  is the resistance of thermoelectric disk.

In a power-compensated DSC setup, the sample and reference crucibles are positioned in distinct furnaces, each equipped with its own heater. This ensures that the sample and reference are always maintained at a null temperature variation. The crucial aspect of this is the measurement and representation of the difference in heat output required to maintain this temperature equilibrium. This discrepancy is tracked as a function of either temperature or time [58].

The use of DSC technique allows the analysis of heat-producing processes and phase transitions such as melting of solids, phase transformations, and glass transitions.

It serves a broader purpose by also allowing the determination of heat capacities. This method provides valuable insight into the energetics and behavior of materials during temperature changes.

The DSC used in this work was a power-compensation DSC, namely the Perkin Elmer-PYRIS Diamond-Differential Scanning Calorimeter (shown in Figure 32). The schematic of the furnaces in this DSC model is in Figure 33. The apparatus contains a platinum resistance thermometer (PRT) for the measurement of the sample and reference temperature. As the temperature of the sample material rises or falls, energy is added to the calorimeter to maintain the system in a "thermal equilibrium" state. Consequently, the energy required to maintain this equilibrium is directly related to the energy changes occurring in the sample. A DSC with power compensation directly quantifies the energy transfer to and from the sample [59].

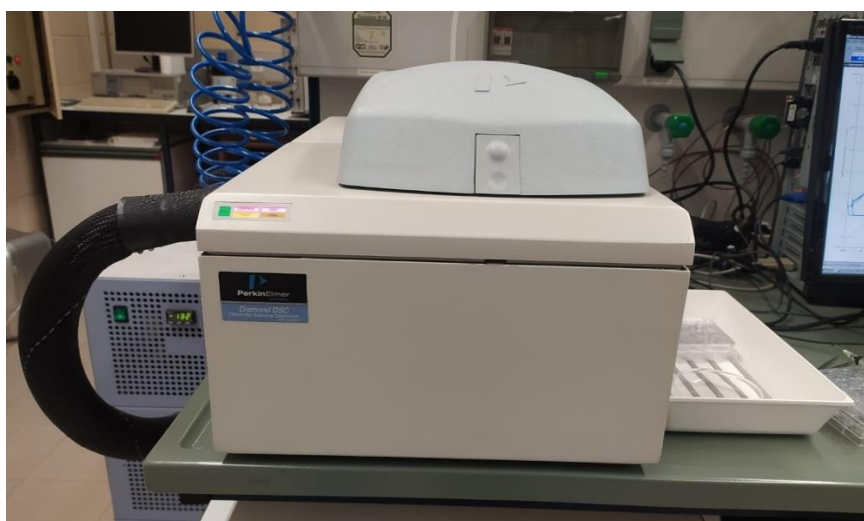


**Figure 32.** Perkin Elmer-PYRIS Diamond-Differential Scanning Calorimeter.

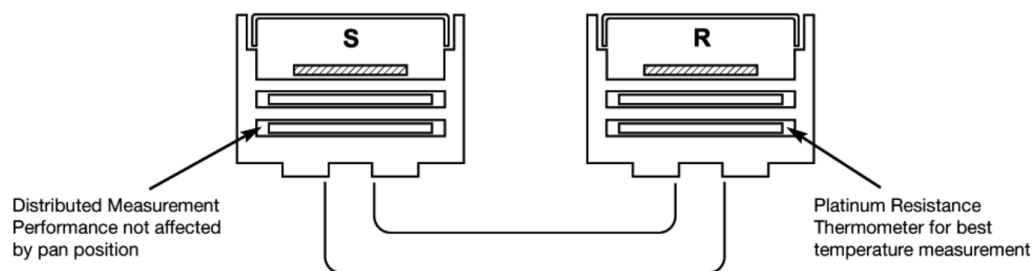


**Figure 33.** Schematics of the furnaces of a Perkin Elmer-PYRIS Diamond-Differential Scanning Calorimeter [59].

Unfortunately, not all compounds could be studied by this method, mainly because of time constraints.

## Knudsen-Quartz Crystal effusion

Aromatic interactions, in conjunction with van der Waals interactions, exert a significant influence on the energy and configuration of aromatic molecules in the solid phase. These orientation-dependent interactions have significant influence on the crystal structure and stability of aromatic compounds. The Knudsen-Quartz Crystal effusion (KNQ) method was employed to measure the temperature-dependent vapor pressures, and to determine the enthalpy, entropy, and Gibbs energy of sublimation for the compounds studied.

This approach relies on simultaneous gravimetric and quartz crystal microbalance mass loss measurements to reduce sample volume and effusion time. This is different to a normal Knudsen effusion method, where mass loss is only determined gravimetrically, and a significant duration of effusion is required to achieve a significant change in mass within the effusion cell [60].

The determination of the equilibrium vapor pressure at a specific temperature,  $T$ , is achieved by allowing the vapor to effuse from a Knudsen cell, similar to a conventional Knudsen experiment. A portion of this vapor condenses onto the surface of a cooled quartz crystal positioned above the cell and intercepting the gaseous flow (shown in Figure 34).

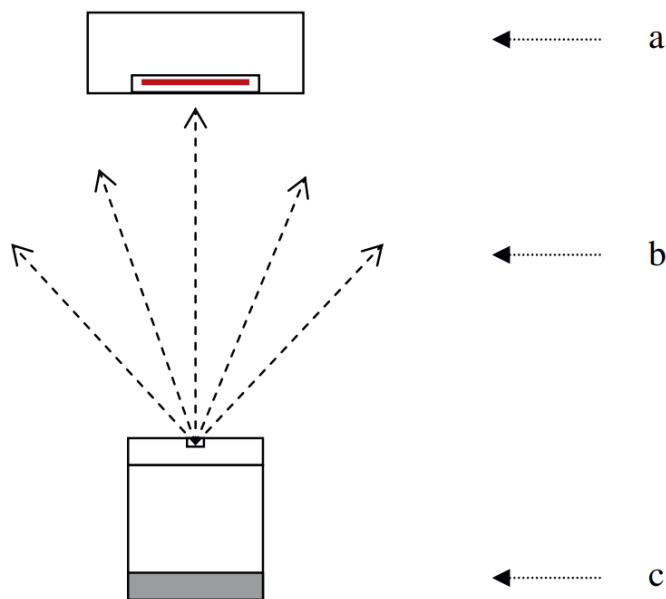


**Figure 34.** Schematic diagram of the effusion process in the KNQ apparatus. a) Quartz crystal holder; b) mass flow; c) Knudsen effusion cell [60].

Thus, the effusion of compound from the Knudsen cell generates two separate measurement indicators: the initial and final gravimetric measurement of the Knudsen cell's mass, and the change in the resonant frequency of the crystal due to the condensation of the effusing vapor onto its surface.

The determination of the vapour pressure by a Knudsen method is based on the measurement of the effusion rate,  $\nu_{eff}$ , of the vapour inside the cell from a small orifice of known area  $A_o$  into the vacuum. By calculating the collision frequency of the gaseous molecules with a wall,  $Z_{wall}$ , of area  $A_o$ , using the following equation,  $\nu_{eff}$  can be obtained [60]:

$$\nu_{eff} = \frac{dN}{dt} = w_o \cdot Z_{wall} \cdot A_o = w_o \cdot \frac{p \cdot N_A}{(2 \cdot \pi \cdot R \cdot T \cdot M_M)^{0.5}} \cdot A_o \quad \text{Eq. 10}$$

Where  $(dN/dt)$  is the number of molecules,  $N$ , effusing from the cell in the time interval  $dt$ ,  $w_o$  is the transmission probability factor and  $p$  is the pressure inside the cell.

While a fraction of the vapor released from the cell's opening condenses onto the quartz crystal's surface, the vapor pressure of the sample at temperature  $T$  can be quantified. This condensation is translated into an electrical signal on the quartz crystal

resonator. As the sample continues to condense on the quartz crystal, there is a decrease in the resonance frequency ( $f$ ) [60].

For that reason, the rate of change of the frequency with time, ( $df/dt$ ), is proportional to the mass,  $m$ , of vapor effused from the cell during the time interval,  $t$ , allowing the calculation of vapor pressure at equilibrium, at a given temperature  $T$ :

$$p = \left( \frac{\Delta m}{\Delta t \cdot A_o \cdot w_o} \right) \cdot \left( \frac{2\pi RT}{M_M} \right)^{0.5} \quad \text{Eq. 11}$$

Using the Dushman equation,  $w_o$  was calculated:

$$w_o = \frac{1}{1 + \frac{3 \cdot l}{8 \cdot r_o}} \quad \text{Eq. 12}$$

Where  $r_o$  is the radius of the orifice, and  $l$  is the thickness. For the orifice used in this work:  $r_o = 0.5000$  mm,  $l = 0.0125$  mm, giving  $w_o = 0.9907$ .

An extra mass deposition on the crystal, will take place during the experiment at a relatively constant rate, referred to as  $\left( \frac{df}{dt} \right)_{drift}$ , that needs to be subtracted [60]:

$$\left( \frac{df}{dt} \right)_{corr} = \left( \frac{df}{dt} \right)_{exp} - \left( \frac{df}{dt} \right)_{drift} \quad \text{Eq. 13}$$

Where the notation “corr” was chosen to specify a corrected value and the notation “exp” to specify the ( $df / dt$ ) signal directly measured during a KNQ experiment.

The Eq. 13 can be rewritten as:

$$\left( \frac{df}{dt} \right)_{corr,T} = -W \cdot \left( \frac{dm_{eff}}{dt} \right)_T \quad \text{Eq. 14}$$

Where  $W$  is the effective mass sensitivity coefficient, and  $dm_{\text{eff}}$  represents the mass of compound deposited on the crystal's surface that comes exclusively from the Knudsen cell.

Integrating for a defined time interval, and considering that  $W$  is constant during an experiment, this yields:

$$W = -\frac{\Delta f_{\text{corr}}}{\Delta m_{\text{eff}}} \quad \text{Eq. 15}$$

Where  $\Delta f_{\text{corr}}$  is the total change observed in the crystal's frequency, corrected for the drift contribution, during the whole KNQ experiment;  $\Delta m_{\text{eff}}$  is the total mass loss from the Knudsen cell, which is measured gravimetrically by weighing the cell in the beginning and in the end of each experiment.

Eq. 11 can then be applied to calculate vapour pressure as a function of  $T$  for the compounds studied. Eq. 11 can be expressed as:

$$p = -\left(\frac{df}{dt}\right)_{\text{corr},T} \cdot \left(\frac{1}{W \cdot A_0 \cdot w_0}\right) \cdot \left(\frac{2\pi RT}{M_M}\right)^{0.5} \quad \text{Eq. 16}$$

Using the Clausius-Clapeyron equation and measuring,  $(df / dt)$ . At varying temperatures one obtains the molar enthalpy,  $\Delta H_{\text{sub}}$ , and entropy,  $\Delta S_{\text{sub}}$ , of sublimation [60]:

$$\ln\left(\frac{p}{p^0}\right) = -\frac{\Delta H_{\text{sub}}}{R} \cdot \frac{1}{T} + \frac{\Delta S_{\text{sub}}}{R} \quad \text{Eq. 17}$$

In the Clausius-Clapeyron equation,  $p$  is the vapor pressure at the temperature  $T$ .

The KNQ used in this work was built through customization (shown in Figure 35) and its schematics are shown in Figure 36.

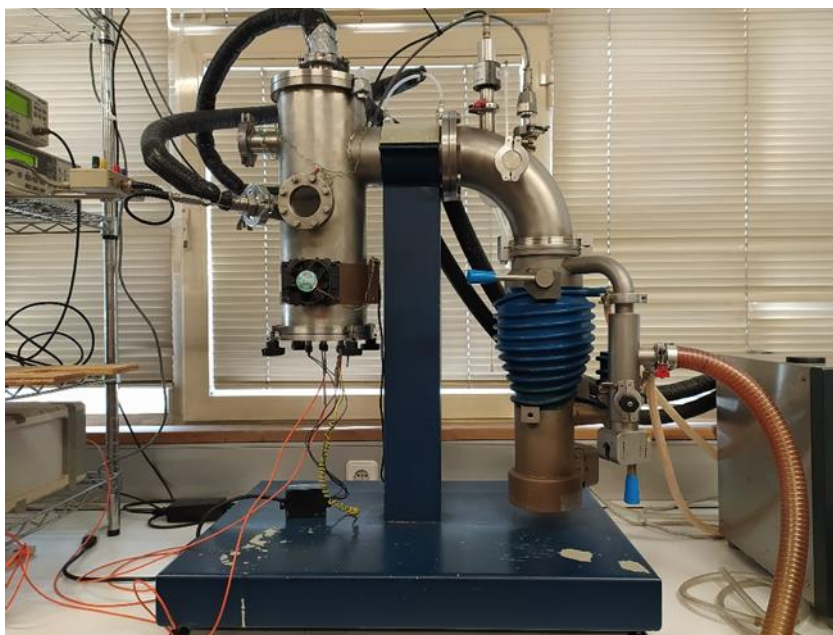


**Figure 35.** Knudsen effusion device that detects mass loss using both gravimetric and quartz crystal microbalance methods.

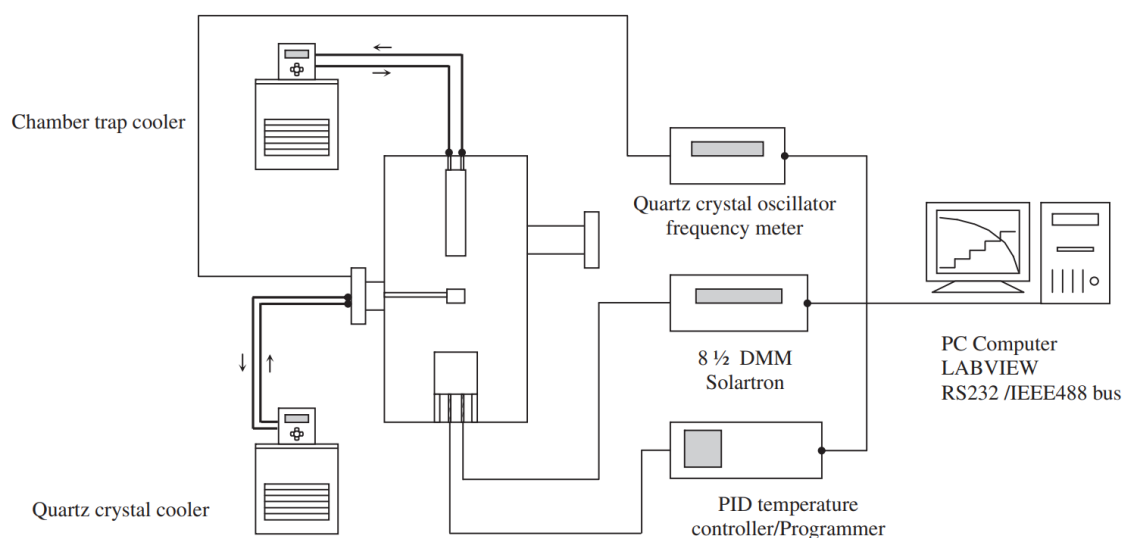


**Figure 36.** Schematic of the Knudsen effusion apparatus with quartz-crystal mass loss detection [60].

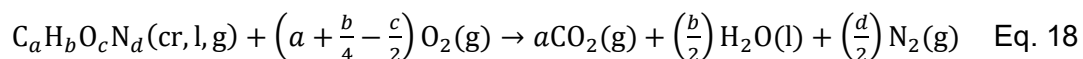
This method was used to study the various thermodynamic properties of sublimation for all the compounds synthesized and studied in this work.

The detailed description of the KNQ apparatus and associated methodology is described in the literature [60].

## Mini-bomb Combustion Calorimetry

Combustion calorimetry stands as the most widely employed method for determining the standard molar enthalpies of formation in the condensed phase of organic compounds containing atoms like C, H, O, N, S, F, Cl, Br, and I. This preference stems from their complete oxidation and the well-characterized final state of the combustion reaction [61].

The combustion reaction of a solid, liquid or gaseous organic compound, containing only C, O, H and N atoms is given by the following equation:



The energy released during a combustion equates to the internal energy,  $\Delta U$ . From  $\Delta U$ , the enthalpy of combustion,  $\Delta_c H$ , can be determined if the combustion is evaluated under constant pressure conditions. The internal energy of combustion,  $\Delta_c U$ , can be determined if the combustion is evaluated under constant volume conditions. The choice between constant pressure or constant volume conditions is determined by the specific calorimetric method employed.

Mini-bomb combustion calorimetry, a subset of combustion calorimetry, requires only tiny amounts of substance, often only a few milligrams (10-20 mg) per experiment. This approach facilitates the extension of the applicability of combustion calorimetry to the study of novel organic compounds that are constantly being synthesized, thus promoting the improvement and extension of the relationship between molecular structure and energy. In today's landscape of molecular energetics, intriguing challenges arise from subtle molecular energy differences, typically on the order of a few  $\text{kJ}\cdot\text{mol}^{-1}$  (5-30  $\text{kJ}\cdot\text{mol}^{-1}$ ) [61].

The determination of  $\Delta_c U$  in these calorimeters is based on:

$$\Delta_c U = C_V(\text{system}) \cdot \Delta T_{\text{ad}} \quad \text{Eq. 19}$$

Where  $C_V(\text{system})$  is the constant volume heat capacity of the calorimetric system;  $\Delta T_{\text{ad}}$  is the corrected adiabatic temperature rise.  $\Delta T_{\text{ad}}$  corresponds to the temperature rise that would be detected in a calorimetric system if it were fully adiabatic and no processes other than combustion occurred in the calorimeter.

In the calorimetric systems used in this work, the temperature of the calorimeter,  $T_{\text{calor}}$ , is initially lower than the temperature of the surroundings,  $T_S$ . This temperature gradient produces a heat transfer from the surroundings to the calorimeter. Since  $T_S$  is constant during an experiment in isoperibol calorimetry, only  $T_{\text{calor}}$  changes. A typical  $T_{\text{calor}} = f(t)$  plot of a combustion experiment in the mini-bomb calorimeter is shown in Figure 37.

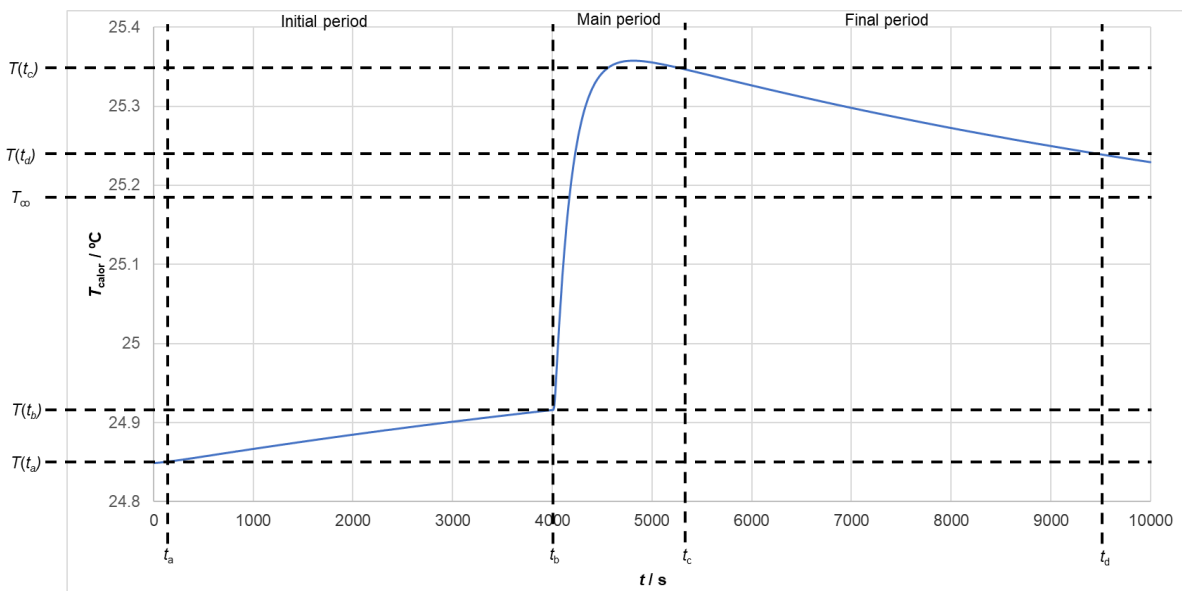


**Figure 37.** Graphical representation of an isoperibol calorimetry experiment.

In isoperibol calorimetry, a temperature profile is divided into three distinct periods:

1. Initial period,  $[t_a, t_b]$ : the variation in  $T_{\text{calor}}$  is mainly due to the heat transfer between the calorimeter and the surroundings, to the heat of stirring (this contribution does not exist in the particular case of the mini-bomb used in this work), and to the heat produced by the temperature sensor.
2. Main period,  $[t_b, t_c]$ : besides the contributions from the initial period, the variation in  $T_{\text{calor}}$  is due to the exothermic combustion process and to the heat produced by the discharge ignition.

- Final period,  $[t_c, t_d]$ : the situation is similar to the initial period, the difference being that  $T_{\text{calor}}$  is now closer to  $T_S$ , and so the rate of change of  $T_{\text{calor}}$  is smaller.

The convergence temperature,  $T_\infty$ , is the temperature that the system would reach in infinite time.  $T_\infty$  is not necessarily the same for distinct calorimetric systems, but it shows a dependency on the value defined for  $T_S$ , and on other factors like geometry of the apparatus and the type of materials used to build it.

The value of  $\Delta T_{\text{ad}}$  can be calculated using the following equation:

$$\Delta T_{\text{ad}} = (T(t_c) - T(t_b)) - \Delta T_{\text{corr}} \quad \text{Eq. 20}$$

Where  $\Delta T_{\text{corr}}$  is a corrective parameter that must be included since the observed temperature rise,  $\Delta T = T(t_c) - T(t_b)$ , has contributions other than the combustion process, and the calorimeter is not perfectly adiabatic.

Neglecting the combustion and ignition process, the global rate of change in  $T$ , ( $dT/dt$ ), in the calorimeter is calculated using the following equation:

$$(dT/dt) = (dT/dt)_{\text{stirring}} + (dT/dt)_{\text{gradient}} = \mu + k \cdot (T_S - T_{\text{calor}}) \quad \text{Eq. 21}$$

When the system reaches  $T_\infty$ , the calorimetry system is in thermal equilibrium: hence, if  $T_{\text{calor}} = T_\infty$ ,  $(dT/dt) = 0$ , then  $T_S$  can be calculated using the following formula:

$$T_S = T_\infty - \frac{\mu}{k} \quad \text{Eq. 22}$$

Substituting  $T_S$  thus derived in Eq. 21 gives for the rate of change in  $T = T_{\text{calor}}$  in the instant  $t_i$ ,  $(dT/dt)_{t_i}$ :

$$(dT / dt)_{t_i} = k \cdot (T_{\infty} - T(t_i)) \quad \text{Eq. 23}$$

Where  $T(t_i)$  is  $T_{\text{calor}}$  for instant  $t_i$ .

The cooling constant,  $k$ , translates the rate at which heat is exchanged between systems and its surroundings. It can be considered a constant if the heat capacity of the system does not alter significantly during an experiment and no perturbations occur. The constant  $k$  is calculated as:

$$k = \frac{(dT / dt)_{t_{mi}} - (dT / dt)_{t_{mf}}}{T(t_{mf}) - T(t_{mi})} \quad \text{Eq. 24}$$

When  $t_{mi}$  and  $t_{mf}$  denote the mean points of the initial and final periods, respectively.

Considering that the calorimetric system is adiabatic, and that  $\Delta T_{\text{ad}}$  corresponds to the temperature change due to the combustion process, then  $\Delta U = 0$  for this process. Usually the term  $\Delta U_{\text{IBP}}$  (isothermal bomb process) is defined, which corresponds to the change in  $U$  in the calorimeter at:  $p_{\text{initial}} = 30 \text{ bar}$ , and  $T_{\text{initial}} = T_{\text{final}} = 298.15 \text{ K}$ , considering all the chemical species that are relevant to the calorimetric process. Side processes related to the combustion reaction also contribute for  $\Delta T_{\text{ad}}$  and hence for  $\Delta U_{\text{IBP}}$ . The main contributors for  $\Delta U_{\text{IBP}}$  are:

- The combustion reaction of a given mass,  $m$ , of the compound studied:  $\Delta_c U(\text{compound}) = \Delta_c u^0(\text{compound}) \cdot m(\text{compound})$ .
- The combustion reaction of a given mass,  $m$ , of a combustion auxiliary substance. In this work benzoic acid was used for some combustion experiments:  $\Delta_c U(\text{aux}) = \Delta_c u^0(\text{aux}) \cdot m(\text{aux})$ .
- The discharge ignition:  $\Delta U(\text{ignition}) = -\frac{1}{2} \cdot C \cdot (V_i^2 - V_f^2)$ , where  $C$  is the capacitance of the discharge capacitor and  $V_i^2$  and  $V_f^2$  are the initial and final voltage of capacitor, respectively.

- The formation of carbon residues when the combustion is incomplete:  
 $\Delta U(\text{carbon}) = \Delta_c u^0(\text{carbon}) \cdot m(\text{carbon})$ , and  $\Delta_c u^0(\text{carbon}) = -33 \text{ kJ} \cdot \text{g}^{-1}$ .

Since  $\Delta U(\text{ignition})$  is an external source of energy, its contribution is subtracted from  $\Delta U_{\text{IBP}}$ . In this way,  $\Delta U_{\text{IBP}}$  only reflects the changes in  $U$  that are a consequence of the processes occurring inside the bomb.

The calculation of  $\Delta U_{\text{IBP}}$  can be carried out using the thermodynamic cycle presented in Figure 38.

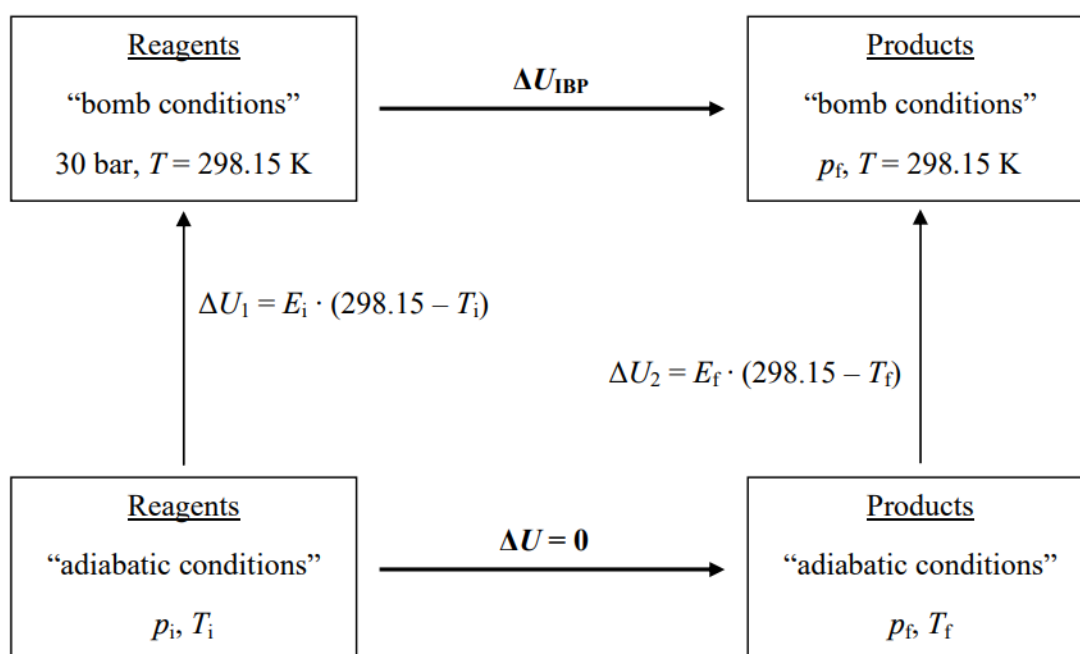


**Figure 38.** Thermodynamic cycle used for the derivation of  $\Delta U_{\text{IBP}}$ .

The “Reagents” and “Products” in Figure 38 refer to all chemical species that are present in the bomb before and after the combustion reaction. Additionally, at “bomb conditions” all the relevant equilibria involving the substances presented in the bomb (vaporization, dissolution, etc.) are considered. The “adiabatic conditions” are the real conditions at which the combustion process occurs but considering that the calorimeter is perfectly adiabatic. The terms  $E_i$  and  $E_f$  can be calculated using the following formulas:

$$E_i = \varepsilon(\text{calor}) + \varepsilon_i \tag{Eq. 25}$$

$$E_f = \varepsilon(\text{calor}) + \varepsilon_f \quad \text{Eq. 26}$$

Where  $\varepsilon(\text{calor})$  is the energy equivalent of the calorimeter and the terms  $\varepsilon_i$  and  $\varepsilon_f$  are the contributions for the total heat capacity of the calorimetric system that are not accounted for by  $\varepsilon(\text{calor})$ .

$\Delta U_{\text{IBP}}$  can be calculated as:

$$\Delta U_{\text{IBP}} = -\varepsilon(\text{calor}) \cdot \Delta T_{\text{ad}} + \varepsilon_i \cdot (T(t_b) - 298.15) + \varepsilon_f \cdot (298.15 - \Delta T_{\text{ad}} - T(t_b)) - \Delta U(\text{ignition}) \quad \text{Eq. 27}$$

To fully correct  $\Delta U_{\text{IBP}}$  from “bomb conditions” to standard conditions, Washburn corrections are employed [62].  $\Delta U_{\Sigma,i}$  and  $\Delta U_{\Sigma,f}$  are the corrective quantities for the initial and final states, respectively.

The main contributions for  $\Delta U_{\Sigma,i}$  are:

- Decompression of the bomb from 30 bar to  $10^5$  Pa.
- Dissolution of  $\text{O}_2(\text{g})$  in  $\text{H}_2\text{O}(\text{l})$ .
- Evaporation of the  $\text{H}_2\text{O}(\text{l})$  that was initially in the bomb until saturation.

The main contributions for  $\Delta U_{\Sigma,f}$  are:

- Decompression of the final bomb’s content from  $p_f$  to  $10^5$  Pa.
- Condensation of the water vapour after combustion
- Removal of the dissolved gases from the liquid phase.

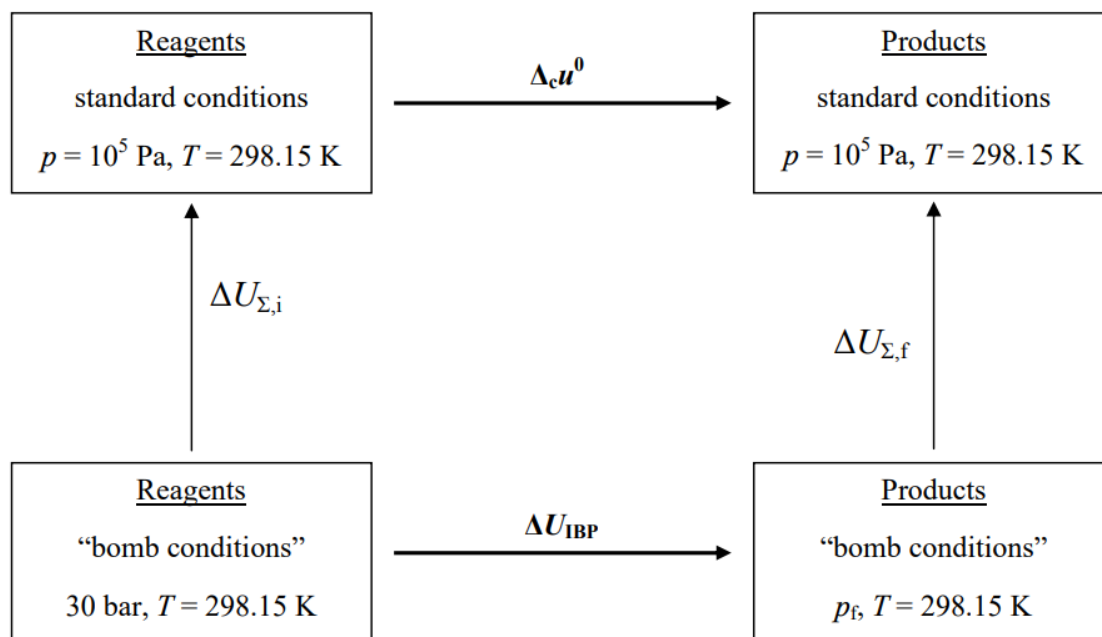


**Figure 39.** Thermodynamic cycle used for the derivation of  $\Delta_c u^0$  from  $\Delta U_{IBP}$ .

It is common practice to define the global Washburn corrections for the combustion process as:  $\Delta U_{\Sigma} = -\Delta U_{\Sigma,i} + \Delta U_{\Sigma,f}$ . Consequently, and in accordance with the thermodynamic cycle illustrated in Figure 39,  $\Delta_c u^0$  can then be calculated as:

$$\Delta_c u^0 = \frac{\Delta U_{IBP} - \Delta_c U(\text{aux}) + \Delta U(\text{carbon}) + \Delta U_{\Sigma}}{m(\text{compound})} \quad \text{Eq. 28}$$

The design and configuration of the mini-bomb combustion calorimeter (shown in Figure 40 and 41) used in this work, was guided by the primary aim of achieving the lowest possible overall uncertainty, which aligns with the precision typically achieved in modern macro-bomb combustion calorimetry setups.

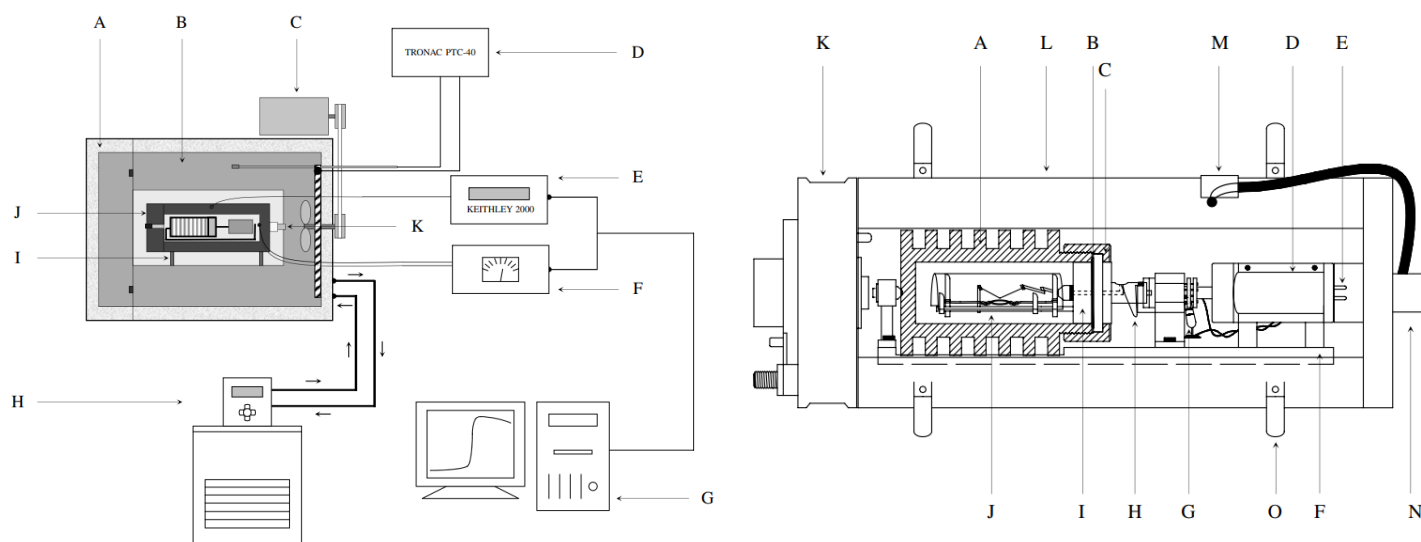


**Figure 40.** Left) Schematic of the mini-bomb calorimeter. A) isolating polystyrene; B) water bath thermostat; C) thermostat stirring motor; D) temperature controller (Tronac PTC40); E)  $6\frac{1}{2}$  digits multimeter (Keithley 2000); F) firing unit; G) personal computer and monitor; H) water-cooling source (Julabo F12-ED); I) insulating calorimeter block support; J) calorimeter block with the bomb; K) DB25 wire connector [61]; Right) Visual representation of the schematics of the bomb, DC motor and the support. A) bomb body; B) Viton O-ring; C) retaining stainless steel ring; D) DC motor; E) electrical terminals; F) bomb and motor support; G) resistor in parallel with the firing circuit; H) firing electrical contact; I) head of the bomb; J) platinum support and electrodes; K) head of the calorimeter block; L) calorimeter block body; M) thermistor; N) DB25 electrical connector; O) thermal insulator [61].

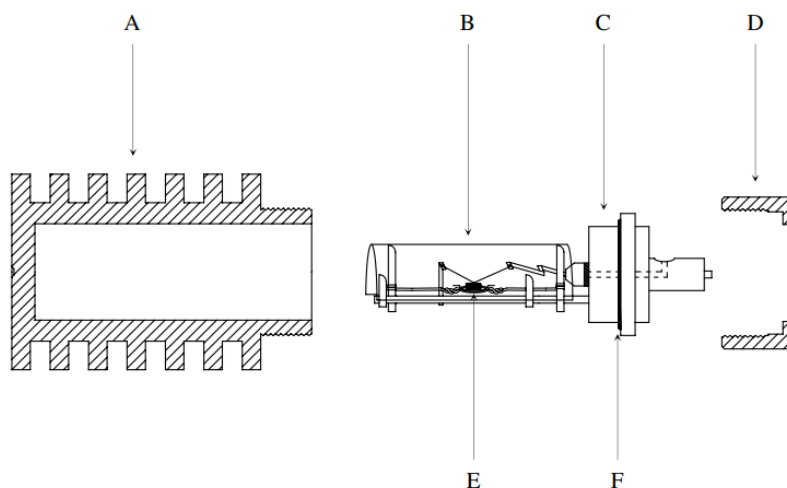


**Figure 41.** Schematic of the bomb assembling. A) bomb body; B) platinum sheet; C) bomb head; D) retaining ring; E) crucible with the sample; F) Viton O-ring [61].

The mini-bomb combustion calorimeter used is shown in Figure 42, along with the pieces for the bomb assembling.

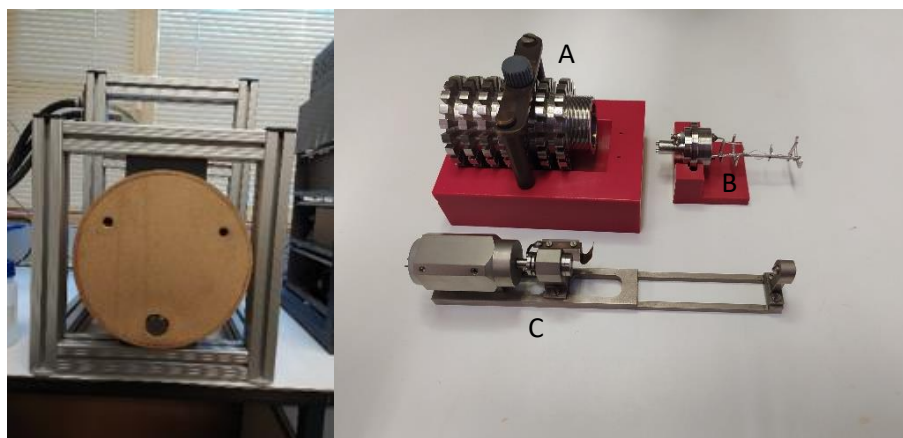


**Figure 42.** Mini-bomb calorimeter used in this work (left image) and the components of a mini-bomb calorimeter (right image). A) bomb body; B) piece with a bomb head, Viton O-ring, where the crucible with the sample will be positioned and where the platinum sheet must be put over; C) bomb and motor support with DC motor, electrical terminals, and a firing electrical contact.

The mini-bomb combustion calorimeter, depicted in Figure 42, was utilized to measure the enthalpies of combustion, at  $T = 298.15$  K, of all the synthesized compounds. The detailed description of the apparatus and associated methodology are described elsewhere [61].

## Quantum Chemistry Calculations

This section delves into the realm of quantum chemical calculations that complement the experimental data. By incorporating both the previously mentioned experimental methods and the computational approach, this study aims to gain a comprehensive understanding of the compounds under investigation. The combined use of these two approaches allows for not only experimental results to be obtained, but also computational data tailored to identify specific energies and behaviors within the compounds.

Aromatic interactions include a good deal of electron correlation, a key element that can be explored in detail through quantum chemical calculations. As stated earlier in the

subsection "Electron Correlation" in the introduction of this thesis, the correlation energy refers to the energy between the Hartree-Fock energy limit and the precise resolution of the nonrelativistic Schrödinger equation [44]:

$$E_{\text{corr}} = \varepsilon_{\text{exact}} - E_{\text{HF}}^{\infty} \tag{Eq. 29}$$

The  $E_{\text{corr}}$  is the correlation energy,  $\varepsilon_{\text{exact}}$  being the exact energy and  $E_{\text{HF}}^{\infty}$  being the Hartree-Fock energy.

Correlation energy refers to the energy that brings a system to a state resembling a uniform electron gas. This energy reaches its highest level when the density gradient is minimal. As the gradient increases, the energy is moderated by a suppression factor that has a bell-shaped curve. This factor is tailored to attenuate the energy from its peak value [63].

Figure 43 shows the change of the gradient previously mentioned,  $|\vec{\nabla}\rho|_{\text{exact}} - |\vec{\nabla}\rho|_{\text{HF}}$ , of two electrons in a Hooke atom (Helium-like atom in which the electron-nucleus Coulomb potential is replaced by a harmonic potential).

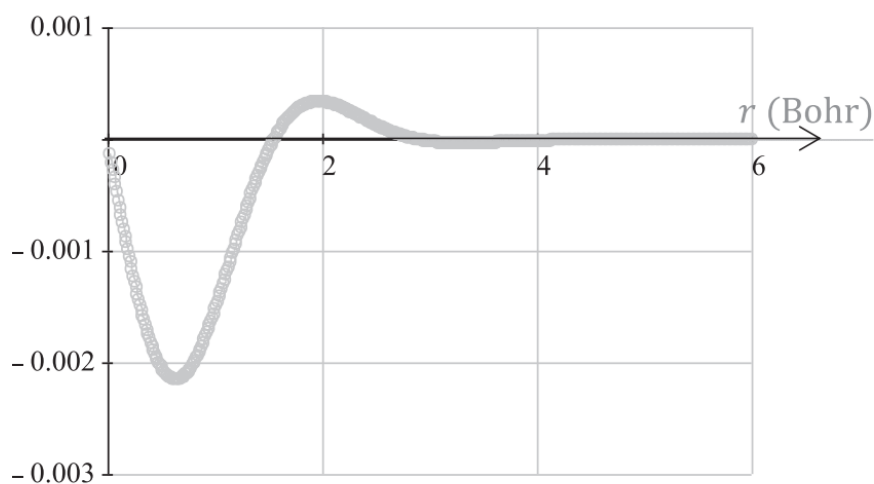


**Figure 43.** Visual representation of the change of gradient,  $|\vec{\nabla}\rho|_{\text{exact}} - |\vec{\nabla}\rho|_{\text{HF}}$  (y axis), due to correlation. The horizontal axis indicates the distance from the center of the Hooke atom [63].

In Figure 43, the gradient experiences a decrease that can be attributed to the presence of electron correlation.

Electron correlation can also change the electron density,  $\rho(\vec{r})$ , in a system, as shown in Figure 44.

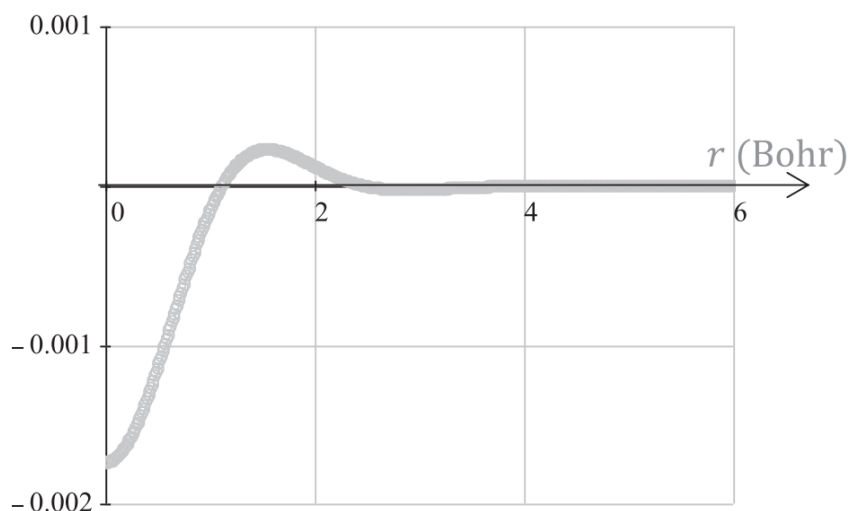


**Figure 44.** Representation of the change of electron density due to correlation:  $\rho_{exact} - \rho_{HF}$  (y axis). The horizontal axis indicates the distance from the center of the Hooke atom [63].

Many commonly used techniques involve either dynamic or non-dynamic correlation modes. Therefore, many computational methods can be classified as either dynamic or non-dynamic correlation. These include approaches such as truncated Configuration Interaction (CI) and Coupled Cluster (CC) wavefunctions, which deal primarily with dynamic correlation, and multiconfiguration (MC) wavefunctions, which consider primarily non-dynamic correlation [45].

In this work, two methods were used: mainly the density functional theory M06-2X, and also Coupled Cluster theory (CC) to better evaluate the correlation energy. The DFT method postulates a direct relationship between energy and electron density [63].

## Density Functional Theory

Density functional theory (DFT) streamlines the many-particle Hamiltonian to enhance its conceptual clarity. Precise energy components are directly computed, while the intricate energy contributions are integrated into the exchange-correlation functional (XC). DFT's straightforwardness facilitates expansion when a more extensive theory becomes necessary. DFT is based on the following function [64]:

$$F[\rho] = \min_{\Psi \rightarrow \rho} \langle \Psi | \hat{T} + \hat{V}_{ee} | \Psi \rangle \quad \text{Eq. 30}$$

Where the minimization is carried out over all properly antisymmetric trial wavefunctions  $\Psi$  that integrate to density  $\rho$ .

The ground-state energy for an external potential,  $v$ , is then found by a search over all  $\rho$  that integrate to the total number of electrons,  $N$ , as:

$$E[v] = \min_{\rho \rightarrow N} F[\rho] + \int d^3r \rho(r)v(r) \quad \text{Eq. 31}$$

Where the form of  $F[\rho]$  is unknown.

To transform Eq. 30, into a practical calculation scheme, one decomposes  $F[\rho]$  into one term that covers the majority of the total energy and can be evaluated exactly and another term that represents the many-body problem of interacting electrons [64].

Since DFT is based on electron density, it is less prone to errors in truncating the basis set. DFT lacks a systematic approach to improving the Hamiltonian and the XC ability to achieve an accurate description of all many-electron interactions in a molecule in a stepwise and well-defined manner. DFT is a correlation-corrected method, but it is unclear exactly which electron correlation effects are covered by a particular DFT approach, making it difficult to predict the reliability of DFT results for a given electronic system [64].

## Coupled Cluster Theory

The coupled cluster (CC) theory is probably the most effective approach for addressing dynamic electron correlation effects in quantum chemistry. Despite its widespread use, it is generally recognized that the coupled cluster singles and doubles (CCSD) method is not capable of providing high-precision results when exceptional accuracy is required. Computations using the CCSD(T) model (also including triple excitations) typically provide results that show remarkable agreement with the full configuration interaction results. However, the computational cost associated with CCSD(T) significantly limits its applicability in chemical studies. The search for a method that surpasses CCSD(T) in accuracy, yet less expensive than CCSD(T), has led to the development of methods that include an approximate treatment of triple excitation effects [65,66].

An extremely appealing aspect of the CC theory lies in its systematic improvement by the inclusion of higher excitation operators. When an appropriately extensive atomic orbital (AO) basis set is used, the following sequence of computational accuracy holds to a high degree [67]:

$$\text{CCSD} < \text{CCSD(T)} < \text{CCSD(TQ)} < \text{fullCI}$$

Triple (T) excitations are important in both covalent and non-covalent interactions. This underscores the importance of the CCSD(T) scheme as the first method in the series to achieve true accuracy. The CCSD(T) method, which is characterised by the iterative inclusion of single and double excitations, alongside with perturbative inclusion of triple excitations, has shown remarkable success in calculating ground-state energies and properties of systems with single-reference characteristics [67].

The fundamental equation of coupled-cluster theory may appear deceptively straightforward [68]:

$$\Psi_{CC} = \left( 1 + T + \frac{T^2}{2} + \frac{T^3}{3} + \dots \right) \Phi_0 \quad \text{Eq. 32}$$

The cluster operator  $T$  consists of interconnected operators, which can be expanded through its constituent components that introduce single  $\Phi_i^a$ , double  $\Phi_{ij}^{ab}$ , triple  $\Phi_{ijk}^{abc}$ , etc. excitations into the wavefunction, as shown in Figure 45 [68]:

$$T = T_1 + T_2 + T_3 + \cdots + T_n \tag{Eq. 33}$$

$$T_n = (n!)^{-2} \sum_{i,j,\dots}^{a,b,\dots} t_{ij,\dots}^{ab,\dots} \hat{c}_a^\dagger \hat{c}_b^\dagger \cdots \hat{c}_j \hat{c}_i \tag{Eq. 34}$$

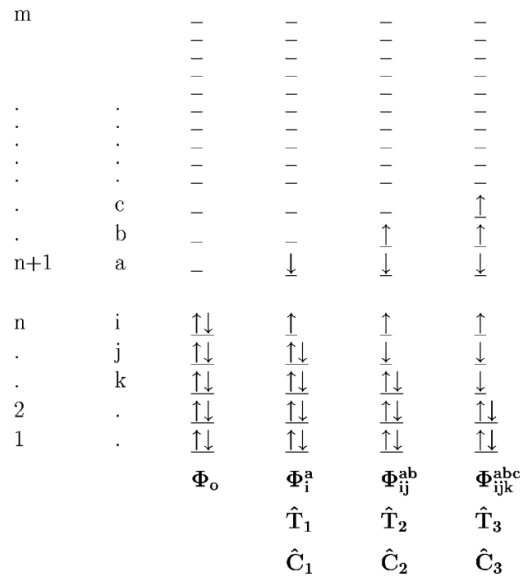


**Figure 45.** Visual representation of graphical examples of selected single  $\Phi_i^a$ , double  $\Phi_{ij}^{ab}$ , triple  $\Phi_{ijk}^{abc}$  excitations due to the  $T_1(C_1)$ ,  $T_2(C_2)$  and  $T_3(C_3)$  operators, respectively [68].

These contributions of  $T_n$  are denoted as connected, as they cannot be further reduced.

## Configuration Interaction

The improvement of Hartree-Fock calculations by superposition of several Slater determinants of different internal structures has come to be known as a "Configuration interaction" [69].

In the early days of quantum chemistry, Configuration Interaction (CI) theory developed as the first post-HF (Hartree-Fock) or post-SCF (self-consistent field) method aimed at improving the Mean-Field Approach (MFA) of HF to obtain a more accurate representation of electron-electron interactions [70].

The Hartree-Fock energy implies a minimum with respect to the mixing of filled and empty spin orbitals. Consequently, S-excited configuration state functions (CSFs) do not interact with the HF ground state (GS) wavefunction. This idea finds its expression in the Brillouin theorem [70]:

$$\langle \Phi_i^a | \hat{H} | \Phi_0 \rangle = \langle S | \hat{H} | O \rangle = 0 \quad \text{Eq. 35}$$

However, as soon as pair correlation or more complex n-electron correlation effects are integrated into the configuration interaction expansion, the optimality of the HF orbitals decreases. In scenarios such as in-out pair correlation, the use of more diffuse orbitals becomes necessary. By incorporating certain orbital expansions, S-excitations play an essential role within a CISD (CI with S and D excitations) or advanced CI wavefunction [70].

Often the orbitals that are occupied in the reference function HF are called internal orbitals. The orbitals that replace the internal orbitals in the CI extension are called external orbitals, and it is generally assumed that these external orbitals are orthogonal to the internal orbitals. Possible options for internal orbitals include HF canonical orbitals, natural orbitals, Brueckner orbitals, and localized orbitals, to name a few. External orbitals can include the virtual orbitals from a HF calculation or any form of extended virtual orbitals [70].

One of the disadvantages of CI lies in its substantial computational demands. Due to the high computational cost, a full configuration interaction (FCI) calculation is only feasible for relatively small electronic systems. Therefore, researchers have moved to using less complex CI extensions that limit the number of excitations at specific levels.

This approach leads to abbreviated CI extensions such as CID, CISD, CI including all S, D, and T excitations (CISDT), or CI including all S, D, T, and Q excitations (CISDTQ) [70].

## Møller-Plesset Perturbation theory

In a perturbative framework for determining the ground-state energy of materials, the second-order Møller-Plesset perturbation theory (MP2) turns out to be the fundamental correction to the widely used HF approximation. This correction accounts for electron correlation as well as non-covalent interactions such as van der Waals forces (which have a significant contribution from electron correlation) [74]. The MP2 method also provides a cost-effective way to integrate dynamical electron correlation into calculations of the electronic structure of molecules. Its applicability spans a variety of scenarios and successfully addresses minor drawbacks of the HF method with self-consistent fields (SCF) [71].

Moreover, MP2 achieves exceptional accuracy in computing observables for systems without degeneracy. Nevertheless, it is generally accepted that MP2 does not adequately reproduce static correlation in degenerate systems [72].

Nevertheless, conventional MP2 theory becomes computationally intensive compared to the methods of SCF when extended to large molecular systems [71,73]. It is also generally considered less accurate compared to the most advanced density functionals currently available. Moreover, its reliability decreases when used for complicated correlation problems that arise in scenarios such as biradicals, transition states, or metal-containing compounds [75].

The MP2 correlation energy is expressed as a sum of antiparallel,  $E_a$ , and parallel,  $E_p$ , spin components:

$$E_{corr}^{MP2} = E_a + E_p \quad \text{Eq. 36}$$

Where  $E_a$  and  $E_p$  are defined by the contributions from electron pairs with  $\alpha\alpha$ ,  $\beta\beta$  and  $\alpha\beta$  spins:

$$E_a = E(\alpha\beta) \quad \text{Eq. 37}$$

$$E_p = E(\alpha\alpha) + E(\beta\beta) \quad \text{Eq. 38}$$

Therefore, the MP2 energy can be expressed as:

$$E^{MP2} = E^{HF} + E(\alpha\beta) + E(\alpha\alpha) + E(\beta\beta) \quad \text{Eq. 39}$$

As apparent from the equations provided above, MP2 calculations inherently yield  $E^{HF}$ . Consequently, in quantum chemical computations conducted using the MP2 approach,  $E^{HF}$  can be directly extracted from the output files.

## Material and methods

This section will elucidate the protocols employed for implementing the previously discussed methods and will encompass the comprehensive characterization of the compounds under investigation.

### Synthesis and characterization of the compounds

In this section, the synthetic procedure, and characterization of the studied compounds are fully described. The characterization techniques encompass  $^1\text{H}$  (300 MHz) and  $^{13}\text{C}$  (75 MHz) NMR spectroscopy. The NMR spectra were recorded on a Bruker Avance 300 spectrometer, with TMS as the internal reference. The NMR spectrometers are part of the National NMR Network (PTNMR) and are partially supported by Infrastructure Project N° 022161 (co-financed by FEDER through COMPETE 2020, POCI and PORL and FCT through PIDDAC). The Agilent 4890D gas chromatograph was used to evaluate the degree of purity, which yielded a purity of more than 99.8% (m/m) for all compounds analyzed. Reaction yields (%) were determined based on the mass of isolated product obtained prior to purification, adjusted for the sample's %(m/m) degree of purity, which was assessed through GC analysis. This high degree of purity ensures reliable results for differential scanning calorimetry, mini-bomb calorimetry, and Knudsen-Quartz crystal measurements.

All the compounds, as previously mentioned, were synthesized by the Suzuki-Miyaura cross-coupling reaction.

The starting reagents 1,8-dibromoanthracene, all the boronic acids,  $\text{K}_2\text{CO}_3$ ,  $\text{Pd}(\text{PPh}_3)_4$ , pyridine-enhanced precatalyst preparation stabilization and initiation (PEPPSI, shown in Figure 46) were commercially obtained from Sigma-Aldrich and Tokyo Chemical Industry (TCI) and used without further purification. The catalyst  $\text{Pd}(\text{PPh}_3)_4$ , that was initially used, was then replaced for PEPPSI, since the latter increased the yield in the synthesis of the compounds.

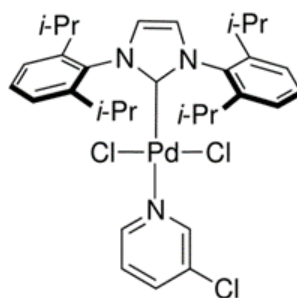


**Figure 46.** Visual representation of the catalyst, otherwise known as PEPPSI.

## Synthesis of 1,8-diarylanthracenes

Since the 1,8-diarylanthracene compounds being studied are not commercially available or are expensive, it was needed to synthesize them.

### General procedure of the synthesis

A solution of  $K_2CO_3$  (6 mol/eq), in 30 ml of water per 1 mmol of the limiting reactant, was added to a solution of 1,8-dibromoanthracene (1 mol/eq), arylboronic acid (4 mol/eq) and PEPPSI (3 mol %) in 70 ml of acetone. The resultant mixture was heated at 70~75 °C for 2 hours under stirring. The final solution was allowed to cool to room temperature and extracted with  $CH_2Cl_2$ . The organic layer was washed with water and aqueous NaOH 0.1 M, dried over anhydrous  $Na_2SO_4$ , and evaporated, yielding the product as impure 1,8-diarylanthracene.

**1,8-diphenylanthracene**: The yellowish solid obtained (0.21 g, yield = 36.8 %) was washed with MeOH and sublimed under reduced pressure to yield yellow crystals of the titled compound (m.p. = 192.2 °C). The  $^1H$  and  $^{13}C$  NMR spectra are presented in Figures 47 and 48 and confirm the identity of the compound.

**1,8-di([1,1'-biphenyl]-4-yl)anthracene**: The greenish brown solid obtained (0.52 g, yield = 59 %) was washed with MeOH and sublimed under reduced pressure to yield yellow crystals of the titled compound. The  $^1\text{H}$  and  $^{13}\text{C}$  NMR spectra are presented in Figures 49 and 50 and confirm the identity of the compound.

The melting point for this compound was not determined.

**1,8-bis(4-methoxyphenyl)anthracene**: The dark green solid obtained (0.56 g, yield = 80 %) was washed with MeOH and sublimed under reduced pressure to yield yellow crystals of the titled compound. The  $^1\text{H}$  and  $^{13}\text{C}$  NMR spectra are presented in Figures 51 and 52 and confirm the identity of the compound.

The melting point for this compound was not determined.

**4,4'-(anthracene-1,8-diyl)dibenzaldehyde**: The brown solid obtained was washed with MeOH and sublimed under reduced pressure to yield yellow crystals of the titled compound.

Regrettably, the yield was so low that it was not possible to give a percentage of the yield. Due to time constraints, it was decided to discontinue the study of this particular compound and to direct efforts to the study of other compounds.

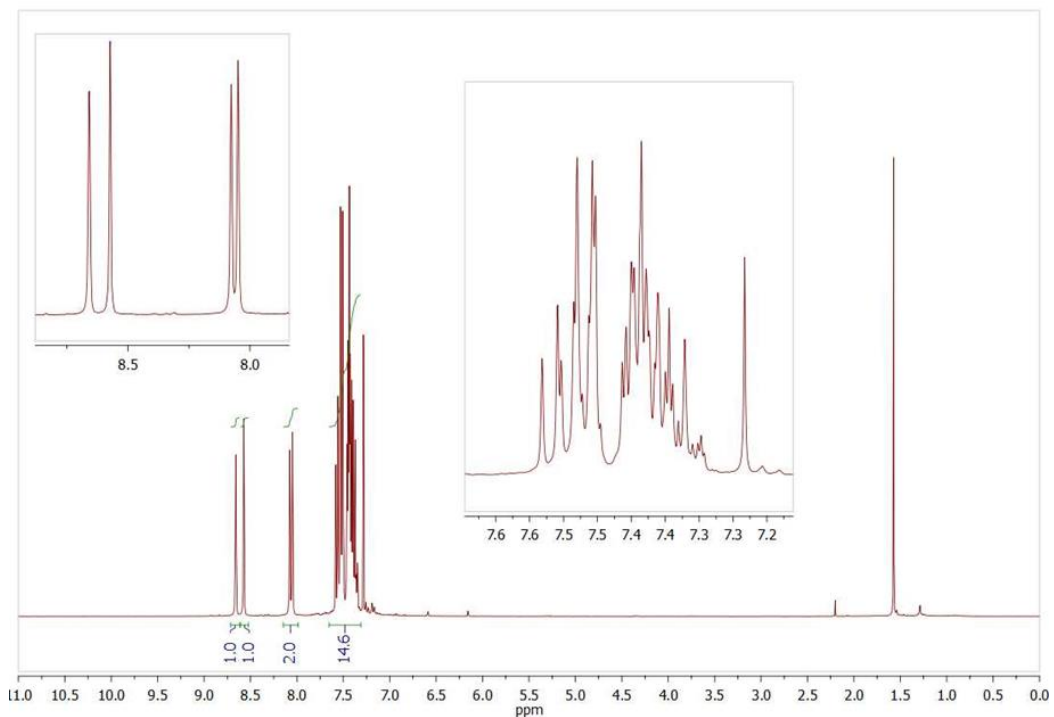


Figure 47. <sup>1</sup>H NMR spectrum of 1,8-diphenylanthracene in CDCl<sub>3</sub>.

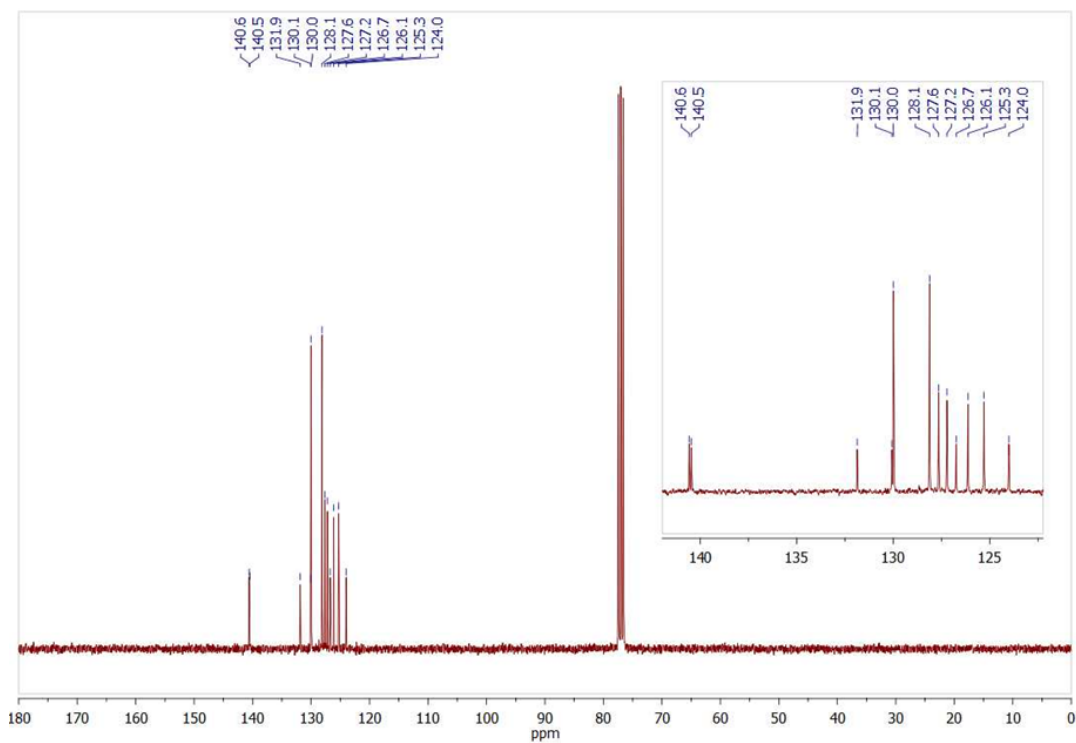
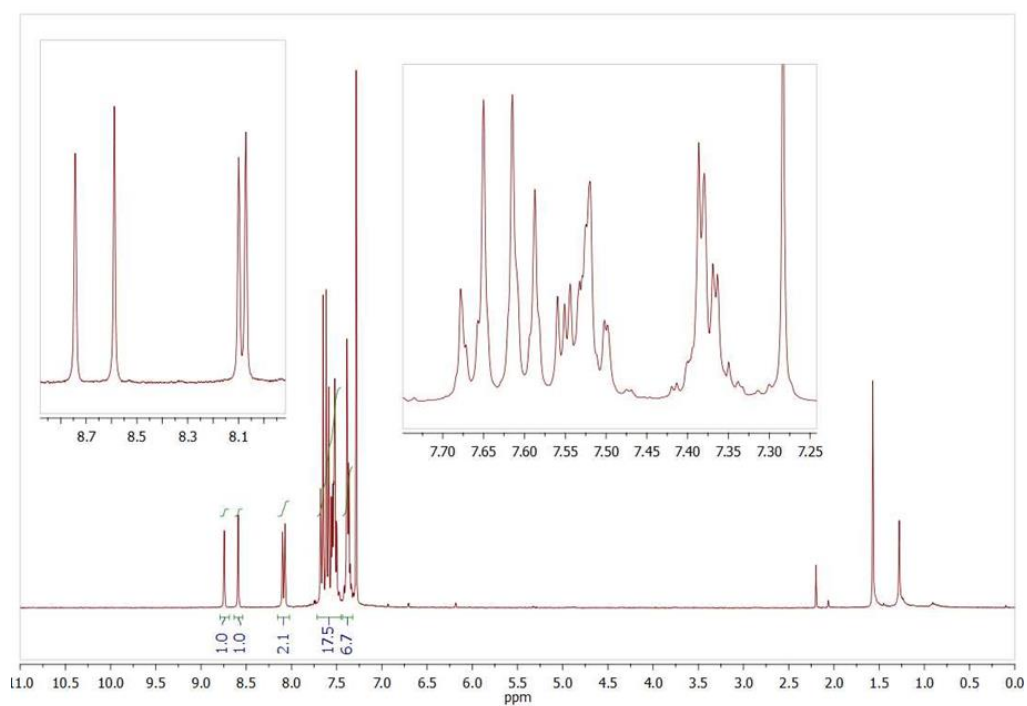
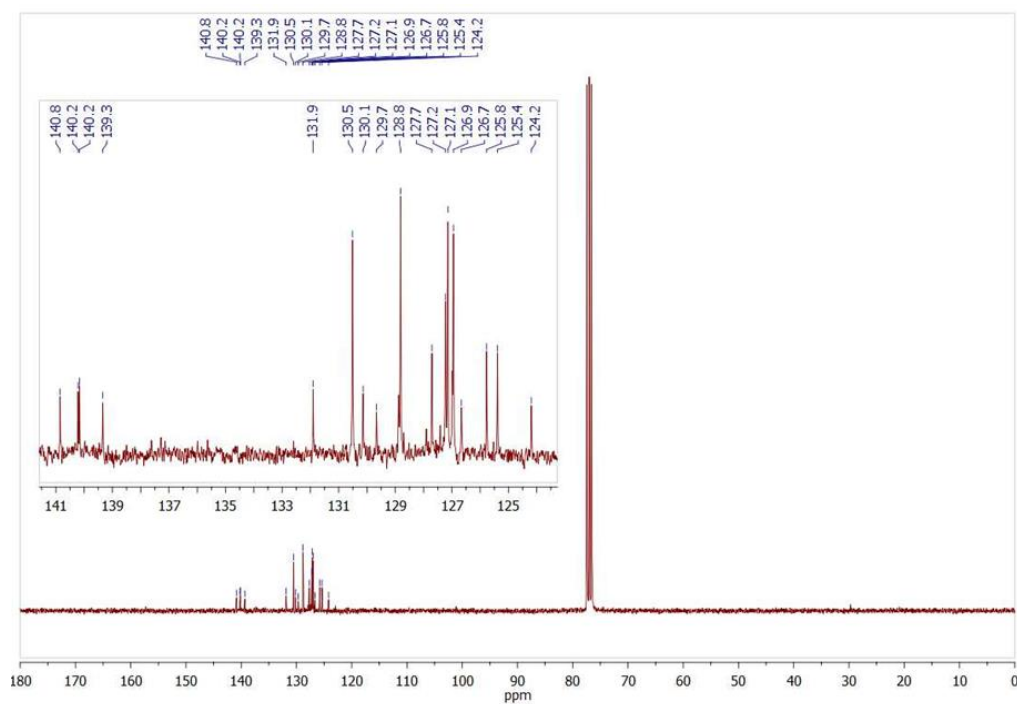


Figure 48. <sup>13</sup>C NMR spectrum of 1,8-diphenylanthracene in CDCl<sub>3</sub>.



**Figure 49.** <sup>1</sup>H NMR spectrum of 1,8-di([1,1'-biphenyl]-4-yl)anthracene in CDCl<sub>3</sub>.



**Figure 50.** <sup>13</sup>C NMR spectrum of 1,8-di([1,1'-biphenyl]-4-yl)anthracene in CDCl<sub>3</sub>.

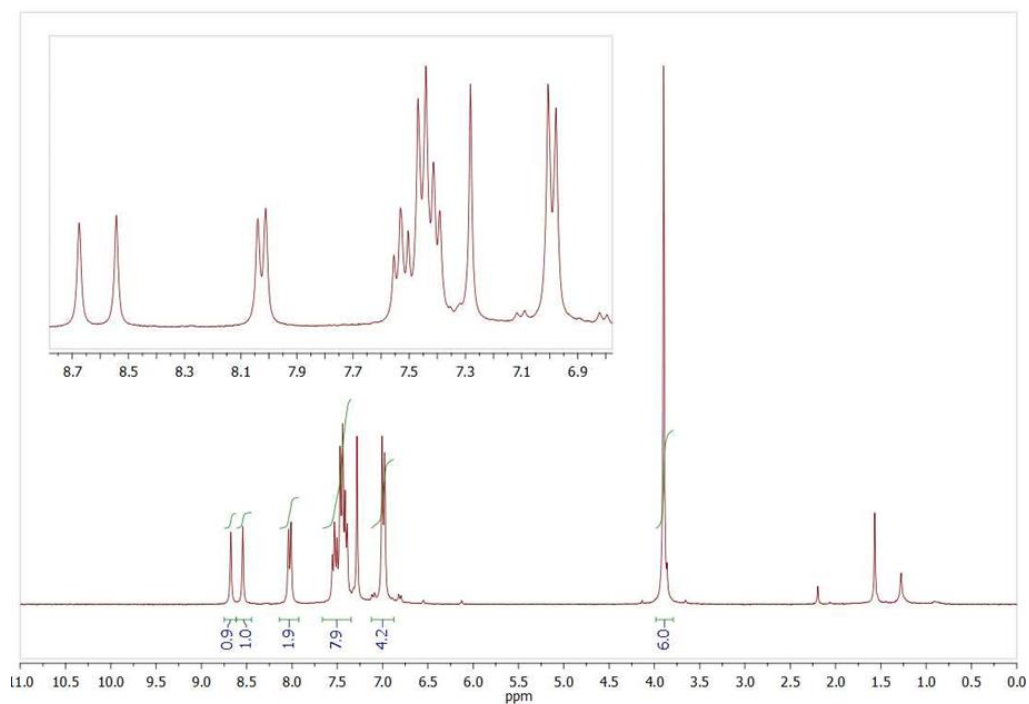


**Figure 51.** <sup>1</sup>H NMR spectrum of 1,8-bis(4-methoxyphenyl)anthracene in CDCl<sub>3</sub>.

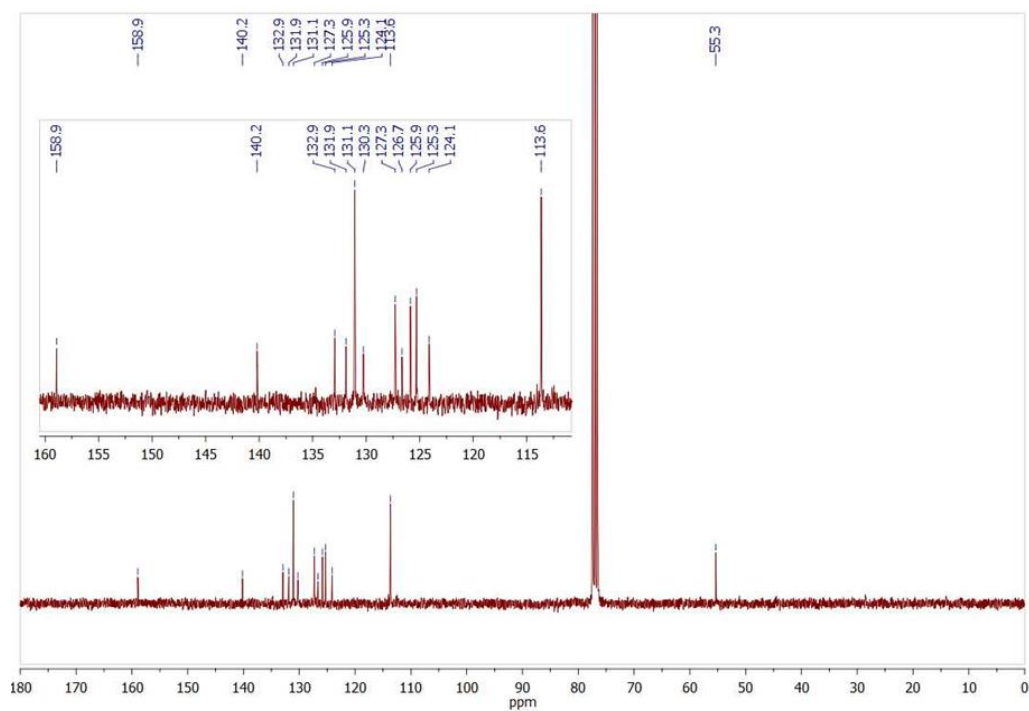


**Figure 52.** <sup>13</sup>C NMR spectrum of 1,8-bis(4-methoxyphenyl)anthracene in CDCl<sub>3</sub>.

## Fourier-transform Infrared Spectroscopy.

The FTIR spectra were acquired using a GLADIATR™ FTIR spectrometer with a monolithic diamond crystal. Thorough cleaning of the spectrometer is essential before starting the measurements.

After the spectrometer is set up, the wavelength range is selected and then a scan is performed with nothing on top of the diamond crystal to obtain a "blank value". This blank scan serves as a reference point and effectively calibrates the absorbance to zero within the specified wavelength range. After creating this blank, a tiny amount of the sample, usually a few milligrams of powder/crystal, is carefully applied to the surface of the monolithic diamond crystal. The sample is then pressed onto the crystal surface using a pressure device, after which a scan is performed to obtain the spectral data. After each scan, the sample is carefully removed from the crystal and returned to its container. The spectrometer is then cleaned so that it is ready for the next scans.

Using this method, the spectra of 1,8-diPhAnth, 1,8-bismethoxyPhAnth and 1,8-dibiPhAnth were obtained. These results were only useful to control the purity of the samples during the purification by sublimation under reduced pressure. For this reason it was as option to not present the spectra in this thesis.

## UV-Vis Spectroscopy

UV-Vis spectra were measured using a diode array spectrophotometer, an Agilent 8453 UV-Vis spectroscopy system with temperature control. Quartz cells with a path length of 10.00 mm were used to record the spectra. Dichloromethane ( $\text{CH}_2\text{Cl}_2$ ) was used as a solvent to dissolve all compounds and obtain their spectra. Beforehand, it was verified that the spectrometer was clean, the solutions studied were properly diluted, the quartz cells were clean and had no scratches that could affect the results. For the analysis, the quartz cell was washed several times with the solution under investigation to ensure that there were no contaminants from previous experiments. After selecting the wavelength range in the spectrometer, the quartz cell was scanned with the blank solution as a "blank" (defines zero absorbance in the selected wavelength range) and

then all solutions of the solute compounds were analyzed with the same quartz cell to obtain the respective spectrum.

Using this method, the spectra of 1,8-diPhAnth, 1,8-diPhNaph, 1,8-bismethoxyPhAnth, 1,8-bismethoxyPhNaph, 1,8-dibiPhAnth, 1,8-dibiPhNaph and 9,10-diPhAnth were obtained.

## Differential Scanning Calorimetry

Before making measurements in differential scanning calorimetry (DSC), it is needed to prepare two crucibles, one of which serves as a reference and the other contains the sample to be analyzed. These crucibles, made of aluminium, have been pressed with a pressing machine and drilled at the top to avoid high pressurization of the crucible at high temperatures. The drilled hole must not be too large or a significant the mass of the sample could escape from the cell.

The DSC must be clean on the outside and inside, especially on the inside, since dust or particles can affect the results of the calorimeter. For this reason, the cells must also be carefully cleaned before and after sealing. In order to perform the analysis, several options of the calorimeter program must be set beforehand, such as the order of temperature, time, etc. For the data analysis, the Pyris Data Analysis Software from PerkinElmer was used.

Unfortunately, only the thermogram for 1,8-diPhAnth was successfully acquired. Time constraints prevented the acquisition of thermograms for both 1,8-bismethoxyPhAnth and 1,8-dibiPhAnth.

## Knudsen-Quartz Crystal

The measurements made with the Knudsen-Quartz Crystal apparatus were performed in the customized Knudsen cell shown in Figure 36. Before starting the measurements, the Knudsen cell must be thoroughly cleaned to remove residues from previous experiments. Acetone and dichloromethane were used for cleaning, as these

solvents are very effective at removing organic contaminants. When using dichloromethane, it is advisable to wear several layers of latex gloves to prevent excessive drying of the hands.

After the cleaning process, the compound to be studied is weighed and properly pressed in a Knudsen cell with a brass piston. The cell is closed and weighed in a Mettler AE163 balance with a resolution of 0.01 mg and inserted into the oven of the apparatus. An aluminum disk is placed above the cell to ensure good thermal contact between the cell and the oven, and the vacuum chamber is closed.

The system is partially evacuated with a rotary pump to minimize the potential for sample decomposition. The furnace is then gradually heated to a predetermined initial temperature. Once thermal stability is achieved, the vacuum chamber is connected to a diffusion pump via a gate valve. The effusion process starts when the pressure drops below 1 Pa.

Once all preparations are complete, start the program and enter the desired temperature and time sequences. Ensure that the chamber maintains the correct pressure. Engage the lever to create a high vacuum in the chamber, start the data sequence and remember to activate a timer on a clock to accurately record the time.

LABVIEW software is used for data acquisition and control. Once the specified effusion time (usually between 4 to 8 hours) and the corresponding temperature step profile are completed, the gate valve is closed, and the vacuum chamber is purged with N<sub>2</sub> gas. After a cooling phase, the vacuum chamber is unsealed. The cell is then removed from the heating block, thoroughly cleaned, and weighed on the same analytical balance to determine the total mass loss resulting from the KNQ experiment.

An initial effusion test is usually performed to remove volatile impurities from the sample and to produce an initial compound layer on the quartz crystal. This first layer usually results in a reduction of the resonance frequency in the range of 1000 Hz. This step ensures the consistency of the effective mass sensitivity coefficient  $W$  and contributes to a more stable background signal called  $(df / dt)_{\text{drift}}$ . This drift is affected, among others, by the inevitable contamination of the walls of the vacuum chamber due to the vapor of the sample.

To assess the effect of frequency drift on the overall frequency shift during the experiment, a separate experiment is performed with an identical empty effusion cell, using a similar effusion time and temperature step profile. A slight but notable drift is usually observed. This signal is typically in the range of 0.005 to 0.015 Hz·s<sup>-1</sup> and is

dependent on the particular sample. Therefore, it is essential to perform drift experiments independently for each compound and for each individual effusion experiment.

Once the full data set of  $\ln p = f(1/T)$  is collected, the sublimation enthalpies and entropies are determined at the average temperature,  $\langle T \rangle$ , and pressure,  $\langle p \rangle$ , within the experimental range. These values are derived using the Clausius-Clapeyron equation. To bring these values from  $\langle T \rangle$  to 298.15 K, the following thermodynamic relations are applied:

$$\Delta H = \int_{T_1}^{T_2} C_p dT \quad \text{Eq. 40}$$

$$\Delta S = \int_{T_1}^{T_2} \frac{C_p}{T} dT \quad \text{Eq. 41}$$

Integration of these equations for the standard molar enthalpy of sublimation, and considering the heat capacity term independent of temperature, results in the following equations:

$$\Delta H_{\text{sub}}^{\circ}(298.15 \text{ K}) = \Delta H_{\text{sub}}^{\circ}(\langle T \rangle) + \Delta C_{p,\text{sub}}^{\circ} \cdot (298.15 - \langle T \rangle) \quad \text{Eq. 42}$$

$$\Delta S_{\text{sub}}^{\circ}(298.15 \text{ K}) = \Delta S_{\text{sub}}^{\circ}(\langle T \rangle, p(\langle T \rangle)) + \Delta C_{p,\text{sub}}^{\circ} \cdot \ln\left(\frac{298.15 \text{ K}}{\langle T \rangle}\right) - R \ln\left(\frac{p^{\circ}}{p(\langle T \rangle)}\right) \quad \text{Eq. 43}$$

Their uncertainties are obtained with the following formulas:

$$\sigma \Delta H = \frac{\sqrt{((\sigma \Delta H(\langle T \rangle) \cdot 1000)^2 + (\langle T \rangle - 298.15)^2 \cdot \sigma \Delta C_p^2)}}{1000} \quad \text{Eq. 44}$$

$$\sigma \Delta S = \sqrt{\sigma \Delta S(\langle T \rangle)^2 + \sigma \Delta C_p^2 \cdot \ln\left(\frac{298.15}{\langle T \rangle}\right)^2} \quad \text{Eq. 45}$$

The standard molar Gibbs energy of sublimation,  $\Delta G_{\text{sub}}^{\circ}$ , at  $T = 298.15$  K, is calculated as:

$$\Delta G_{\text{sub}}^{\circ} = \Delta H_{\text{sub}}^{\circ} - T \cdot \Delta S_{\text{sub}}^{\circ} \quad \text{Eq. 46}$$

The uncertainty of the standard molar Gibbs of sublimation is calculated as:

$$\sigma \Delta G_{\text{sub}}^{\circ} = \sqrt{\sigma \Delta H_{\text{sub}}^{\circ}{}^2 + 298,15^2 \cdot \left( \frac{\sigma \Delta S_{\text{sub}}^{\circ}}{1000} \right)^2} \quad \text{Eq. 47}$$

Using this technique, the sublimation properties of 1,8-diPhAnth, 1,8-bismethoxyPhAnth, and 1,8-dibiPhAnth were obtained.

## Mini-Bomb Combustion Calorimetry

To set up the calorimeter as shown in Figure 40-41, it is first necessary to ensure that the platinum support and the other platinum components of the mini-bomb are clean. This cleanliness is achieved by calcination under a butane flame.

The samples are then pressed into pellet form, carefully cleaned and placed in a platinum crucible, and their apparent mass measured using a Mettler Toledo micro-balance, model UMT2, with a sensitivity of  $\pm 10^{-7}$  g. This prepared sample is then placed on the platinum support.

The electrical ignition for the experiment is done using a 2 cm platinum wire (Goodfellow, with a mass fraction of 0.999 and  $\Phi = 0.080$  mm) attached to both electrode terminals and directed toward the pellets in a "V" shape. To concentrate the heat and minimize the formation of carbon residue, a platinum sheet is positioned in an inverted "U" shape over the crucible assembly.

A volume of ultra-pure water (0.050 cm<sup>3</sup>) is introduced into the bomb. The head is then fitted to the body of the mini-bomb using an O-ring and fixed in place with a screw ring. The bomb undergoes four rinsing cycles and is then pressurized with high-purity oxygen, reaching a pressure of 3.04 MPa.

The bomb is then carefully inserted into its holder, which is equipped with an electrical contact to trigger the electrical discharge. This assembly is then inserted into a cylindrical copper block containing a bean-shaped thermistor for temperature monitoring. To improve heat conduction between the bomb and the block, helium is introduced after purging, filling the block to a pressure of 0.2 MPa.

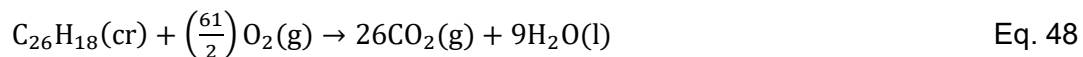
The calorimetric setup is in a temperature-controlled water bath that is maintained strictly at a stable temperature of (298.150 ± 0.001) K using a TRONAC temperature controller, specifically the PTC-40 model.

To collect data, a 6 ½ digit multimeter (Keithley, model 2000) connected to a PC is used to measure the resistance of the thermistor at 10-second intervals.

Once the mini-bomb and calorimeter are properly set up, the operator should start the calorimeter program and set the required parameters and sequences before beginning the combustion experiment. The LABTERMO software controls the ignition of the sample and is precisely tuned to calculate the adiabatic temperature rise in the bomb.

Combustion calorimetry allows the measurement of the enthalpy of combustion, which is referred to as  $\Delta_{\text{comb}}H^{\circ}_{\text{m}}$ . This measurement serves as a valuable tool for determining the change in enthalpy of formation, denoted as  $\Delta_{\text{f}}H^{\circ}_{\text{m}}$ , for the compound under study in its condensed phase. This determination is possible because the  $\Delta_{\text{f}}H^{\circ}_{\text{m}}$  values for H<sub>2</sub>O(l) and CO<sub>2</sub>(g) are already known with high accuracy.

The chemical equation for the combustion of, for example, 1,8-diPhAnth is:



In this way, the  $\Delta_f H_m^0$  of 1,8-diPhAnth can be calculated, using Hess's law, by the following equation:

$$\Delta_f H_m^0 (\text{C}_{26}\text{H}_{18}, \text{cr}) = 26 \cdot \Delta_f H_m^0 (\text{CO}_2, \text{g}) + 9 \cdot \Delta_f H_m^0 (\text{H}_2\text{O}, \text{l}) - \Delta_{\text{comb}} H_m^0 \quad \text{Eq. 49}$$

Using this method, the  $\Delta_f H_m^0(\text{cr})$ , at 298.15 K, were determined for 1,8-diPhAnth, 1,8-bismethoxyPhAnth, and 1,8-dibiPhAnth.

## Quantum Chemistry Calculations

All quantum chemical computations were executed using the Gaussian 09 software package [76]. The computational procedure begins with an examination of the Potential Energy Surface (PES) to locate the global minimum of the system through comprehensive geometry optimizations. For certain compounds, this identified global minimum is used for frequency calculations, which subsequently allows the determination of various thermodynamic properties for the gaseous species.

For the compounds included in the computational study, full geometry optimizations without symmetry constraints were performed at the M06-2X/6-31+G(d,p) and MP2/cc-pVDZ levels of theory.

Frequency calculations, at the M06-2X/6-31+G(d,p) level, were performed on the optimized molecular geometries. Additional single point energy calculations, on the MP2/cc-pVDZ optimized geometry, were performed using CCSD(T)/cc-pVDZ for some molecules. The corresponding electronic energies were corrected for the zero-point energy (ZPE) and thermal enthalpies to  $T = 298.15$  K, using no scaling factors.

Using this method, the calculations at the M06-2X/6-31+G(d,p), CCSD(T)/cc-pVDZ levels of theory for the majority of the compounds under investigation were obtained.

## Results and Discussion

This section will be divided in 3 subsections, where the results obtained with the help of the previously mentioned methods will be presented and discussed. These subsections are Phase Behaviour, Molecular Energetics and Optical Properties.

In Phase Behaviour, the results obtained through the DSC and KNQ methods will be presented. The DSC method was only applied for 1,8-diPhAnth. The thermograms and some tables, showing the melting properties not only for this compound but also for reference compounds, will be shown. As for the KNQ method, the various sublimation properties, and graphs for the three 1,8-diarylanthracenes will be presented alongside some reference compounds for comparison.

In Molecular Energetics, the results obtained through Mini-Bomb Combustion Calorimetry and Quantum Chemistry Calculations will be shown. In the context of Mini-bomb Combustion Calorimetry, the enthalpies of combustion and the corresponding enthalpies of formation in the crystal phase are presented for the three 1,8-diarylanthracenes and the selected reference compounds. The first tables contain values obtained from numerous combustion experiments for the three 1,8-diarylanthracenes. Subsequently, these results are summarized in a comprehensive table together with the results for all compounds. Concerning Quantum Chemistry Calculations, the calculated enthalpies of reaction are presented for comparison with the experimental data. These enthalpies of reaction are calculated for carefully selected homodesmotic reaction schemes.

In Optical Properties, the spectra derived from UV-Vis Spectroscopy are presented for the compounds studied. The goal of these spectra is to observe the shifts that occur when the parent structure and substituents change.

It is known that increasing the distance between two closely interacting partners leads to increased stability to a certain degree. This increased distance reduces the Pauli repulsion between substituents and thus promotes stronger interactions. In addition, the choice of substituent also affects stability. The results obtained should offer a more comprehensive explanation to address this query.

## Phase Behaviour

This section will serve to present and discuss the results obtained through the KNQ and DSC methods.

Figures 53 and 54 show the DSC thermograms obtained for 1,8-diPhAnth.

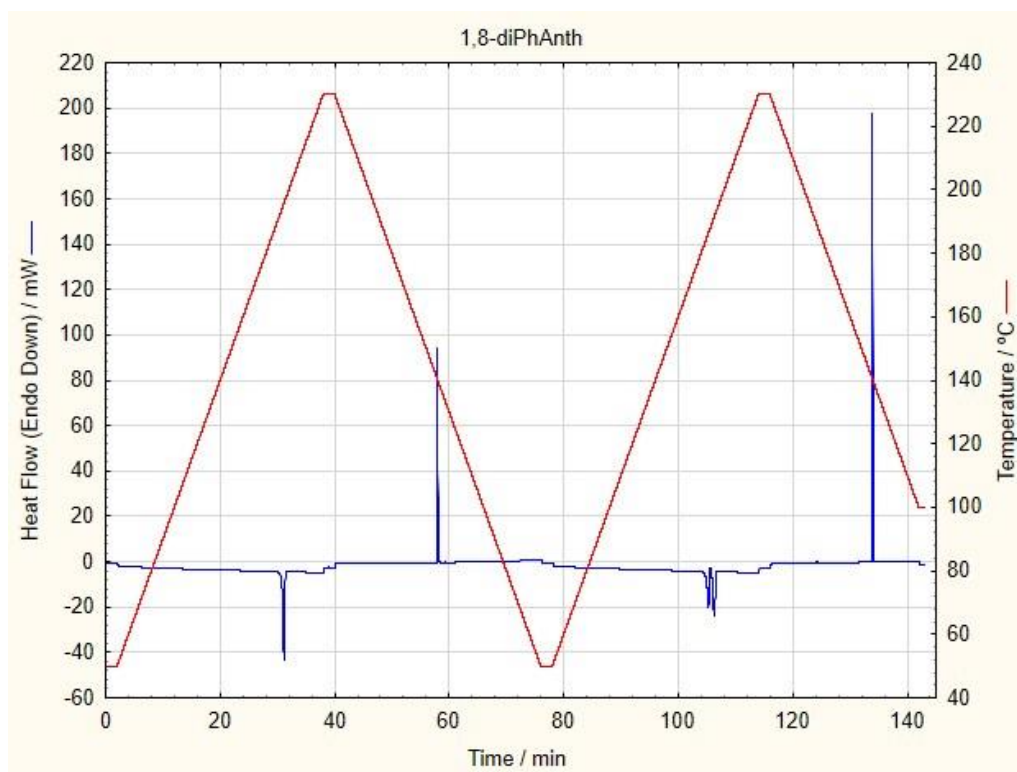


**Figure 53.** DSC thermogram of 1,8-diPhAnth, performed at a heating rate of 5 K/min and showing the fusion and crystallization processes. Graph made with Statistica Software.

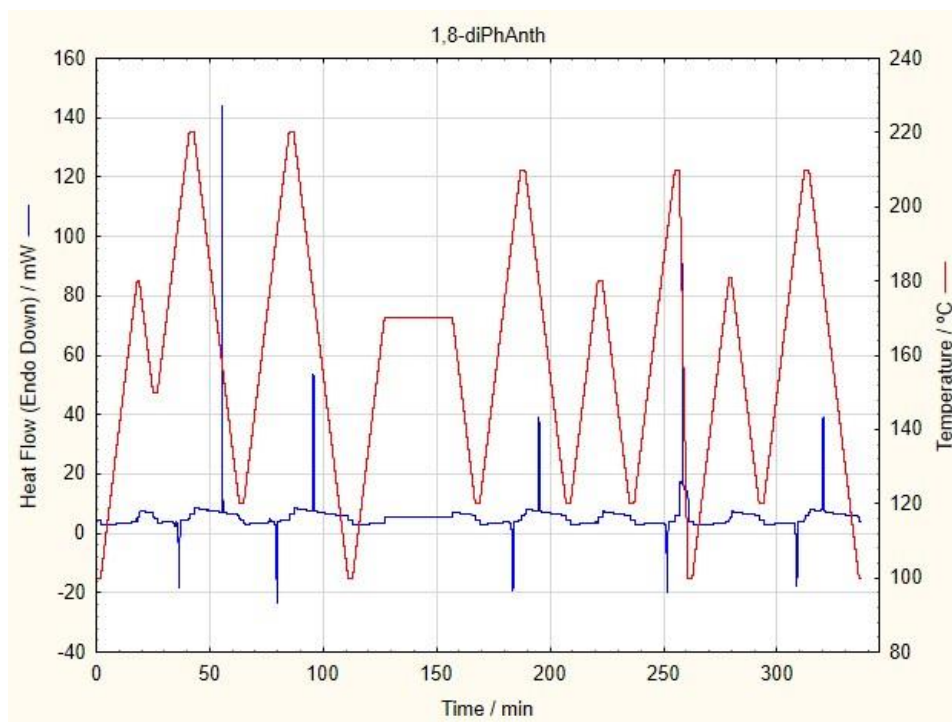


**Figure 54.** DSC thermogram of 1,8-diPhAnth, performed at a heating rate of 5 K/min and one time at a heating rate of 30 K/min (~260 min). This thermogram shows the fusion and crystallization processes of the compound. Graph made with Statistica Software.

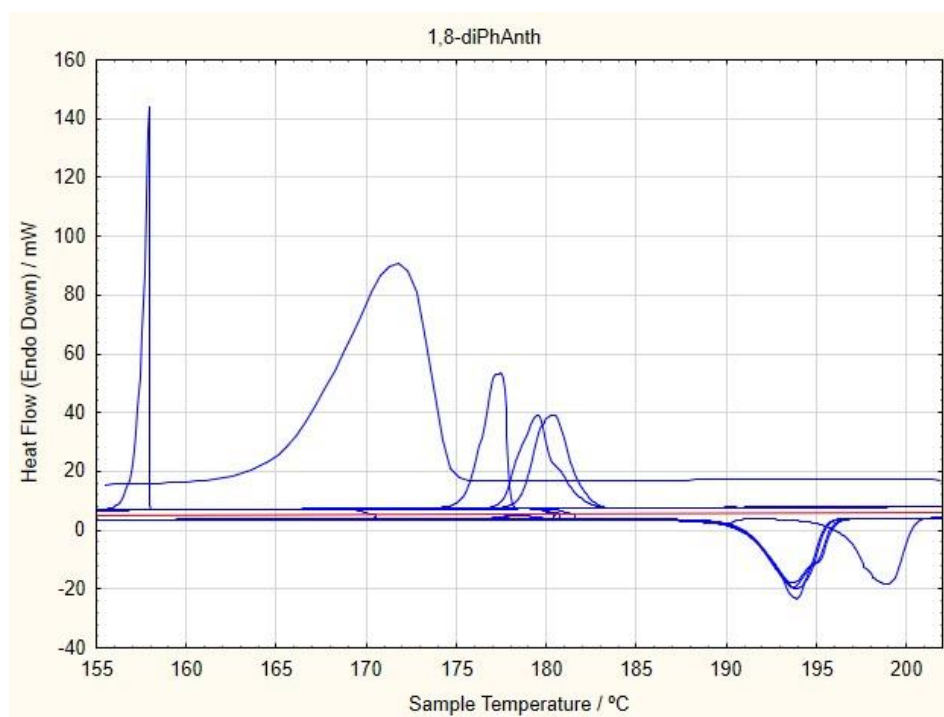


**Figure 55.** DSC thermogram of heat flow as a function of temperature of 1,8-diPhAnth, performed at a heating rate of 5 K/min and one time at a heating rate of 30 K/min (~260 min). This thermogram shows the fusion and crystallization processes of the compound. Graph made with Statistica Software.

Both thermograms were made from equal samples in the same crucible. The only difference is in the timing of their acquisition: the thermogram in Figure 53 was obtained immediately after the crucible was prepared, while the thermogram in Figure 54 and Figure 55 was recorded after a weekend had elapsed, constituting a period of ~72 hours.

In Figure 53, it is easy to see that 1,8-diPhAnth has at least three polymorphs, which is reflected in its melting peaks. While the initial melting process shows a single peak, the subsequent melting process shows two distinct peaks (both with different melting points) whose combined areas are similar to those of the first melting peak. The appearance of three polymorphs indicates that 1,8-diPhAnth, in the crystallization process, can adopt different crystalline phases. The most stable crystalline phase (here denoted polymorph  $\alpha$ ) is the one where the fusion temperature is higher, since for all cases the liquid phase is the same.

The purpose of Figure 54 and Figure 55 was to investigate the different polymorphic forms of 1,8-DiPhAnth and try to isolate them in order to better understand the conditions in which they form. For this purpose, different heating rates were used to study the behavior of the compound under different thermal conditions. Similar to the thermogram in Figure 53, Figure 54 and Figure 55 also shows the presence of three different polymorphic forms.

In a prior investigation conducted by Yuto Hino and Shotaro Hayashi, they identified two polymorphic forms of 1,8-diPhAnth, as illustrated in Figure 56 [77]. It can be observed that in both polymorphs, the molecules adopt a conformation with the phenyl rings in a V-shape.

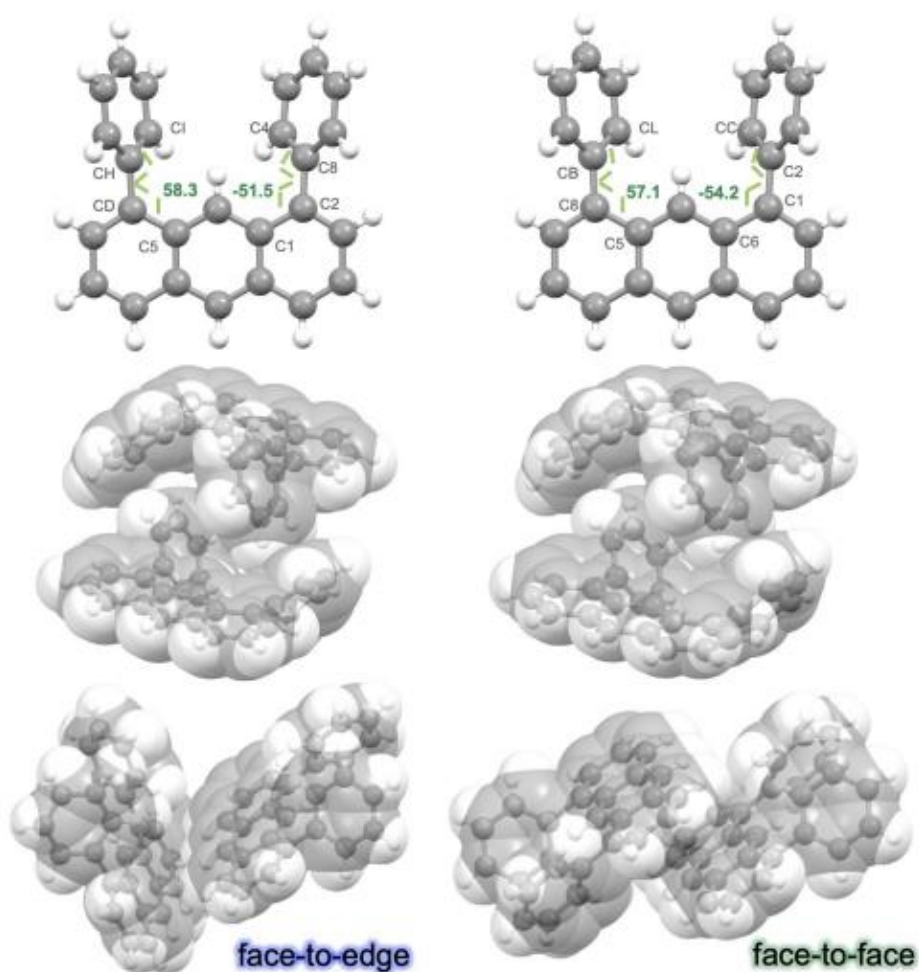


**Figure 56.** Single-crystal structures of two 1,8-diPhAnth polymorphs. Left) face-to-edge; Right) face-to-face [77].

According to the authors, the stability of the crystal system was determined primarily by the arrangement of the phenyl groups and anthracene components, which led to a discernible disorder of the crystals triggered by mechanical and thermal factors. These properties included crystal-to-crystal phase transitions and single-crystal-to-single-crystal (SCSC) phase transitions [77].

It is reasonable to assume that of the three polymorphs detected by DSC, two correspond to the polymorphs in Figure 56, while the third represents a new discovery. One possible explanation for the presence of this unique polymorph is a particular molecular arrangement or configuration (presumably one polymorph displaying the two phenyl rings parallel to each other).

Table 3 shows the fusion properties of the different polymorphs found in this dissertation.

**Table 3.** Results of the thermodynamic properties of fusion of three different polymorphs of 1,8-diPhAnth.

Compounds	$T_{fus} / K$	$\Delta_{fus}H^{\circ}(T_{fus}) / kJ \cdot mol^{-1}$	$\Delta_{fus}S^{\circ}(T_{fus}) / J \cdot K^{-1} \cdot mol^{-1}$
<b><math>\alpha</math> Polymorph</b>	465.3 $\pm$ 0.3	30.6 $\pm$ 1.9	65.7 $\pm$ 4.0
<b><math>\beta</math> Polymorph</b>	460.6 $\pm$ 0.3	32.2 $\pm$ 1.9	69.9 $\pm$ 4.0
<b><math>\gamma</math> Polymorph</b>	456.3 $\pm$ 0.3	32.0 $\pm$ 1.9	70.2 $\pm$ 4.0

The data presented in Table 3 show that the  $\alpha$  polymorph has the highest fusion temperature, indicating its superior stability among the three polymorphs in the crystal phase. Looking at the thermodynamic properties of fusion, all three polymorphs show similarities, although the  $\alpha$  polymorph has slightly lower values for both the enthalpy and entropy of fusion.

Hino and coworkers have reported similar melting points for two polymorphs of 1,8-diPhAnth [77]. According to their results, the  $\alpha$  polymorph corresponds to the face-to-edge and the  $\beta$  polymorph to the face-to-face in Figure 56. The lower  $\Delta_{fus}S^{\circ}$  is clearly the reason why  $\alpha$  has the highest  $T_{fus}$ . Comparison between the X-ray structures of the two polymorphs does suggest a larger thermal motion of the phenyl rings in the  $\alpha$  polymorph, which can explain the greater entropy of this solid [77].

The following Table 4 shows the fusion temperature and the various thermodynamic properties of fusion of 1,8-diPhAnth along with some reference compounds. The values used for 1,8-diPhAnth are from the most stable polymorph  $\alpha$ .

**Table 4.** Experimental results concerning the fusion of the compound studied and some reference compounds, at  $T_{average} = 433$  K.

Compounds	$T_{fus} / K$	$\Delta_{fus}H^{\circ}(T_{average}) / kJ \cdot mol^{-1}$	$\Delta_{fus}S^{\circ}(T_{average}) / J \cdot K^{-1} \cdot mol^{-1}$
<b>Naphthalene<sup>[78]</sup></b>	353.4	23.1 $\pm$ 1.6	64.2 $\pm$ 4.1
<b>Anthracene<sup>[78]</sup></b>	490.0	26.5 $\pm$ 1.1	53.8 $\pm$ 2.5
<b>1,8-diPhNaph<sup>[79]</sup></b>	423.2	29.9 $\pm$ 1.0	70.6 $\pm$ 2.4
<b>1,8-diPhAnth</b>	465.3 $\pm$ 0.3	29.0 $\pm$ 2.0	62.1 $\pm$ 4.3

Examining the data presented in Table 4 shows that anthracene has a higher fusion temperature and enthalpy of fusion compared to naphthalene. This observation indicates that anthracene exhibits greater stability (solid-liquid stability) than naphthalene in the context of the fusion phenomenon, which is easily explained by the bigger size of anthracene. Anthracene, consisting of three fused benzene rings, has a higher size, making it have more C-H···π interactions. In contrast, naphthalene contains only two fused benzene rings, making it have less C-H···π interactions between neighboring naphthalene molecules in the solid state, leading to weaker cohesive interactions compared to anthracene.

In the disubstituted aromatic systems, the compound 1,8-diPhNaph is found to have the expected higher fusion temperature and enthalpy of fusion compared to naphthalene. This can be attributed to the increase of intermolecular dispersive interactions. These interactions contribute to the increase of the melting point of 1,8-diPhNaph by strengthening its molecular cohesion. The increase of  $\Delta_{fus}S^{\circ}(T_{fus})$  observed with 1,8-diPhNaph results from increased molecular complexity and enhanced internal mobility due to the presence of two flexible substituents.

Despite its higher  $T_{fus}$  compared to naphthalene, 1,8-diPhNaph still falls short of anthracene's  $T_{fus}$ , probably due to a higher crystal packing efficiency of the more regular and compact structure of anthracene.

The molecule 1,8-diPhAnth has a higher  $T_{fus}$  than 1,8-diPhNaph but a lower one than anthracene. The addition of the substituents limits the amount of C-H···π intermolecular contacts that one molecule can establish, leading to an overall less robust crystal structure.

Table 5 shows the increment in the enthalpies,  $\Delta\Delta_{fus}H_m^{\circ}$ , and entropies,  $\Delta\Delta_{fus}S_m^{\circ}$ , of fusion for the compounds studied, at  $T_{average} = 433$  K, calculated as:

$$\Delta\Delta_{fus}H_m^{\circ} = \frac{(\Delta_{fus}H_m^{\circ}(\text{disubstituted compound})) - (\Delta_{fus}H_m^{\circ}(\text{parent compound}))}{2} \quad \text{Eq. 50}$$

$$\Delta\Delta_{fus}S_m^{\circ} = \frac{(\Delta_{fus}S_m^{\circ}(\text{disubstituted compound})) - (\Delta_{fus}S_m^{\circ}(\text{parent compound}))}{2} \quad \text{Eq. 51}$$

**Table 5.** Increments in the enthalpy and entropy of fusion per substituent in the compounds studied, at  $T = 433$  K.

Compound	$\Delta\Delta_{\text{fus}}H_m^0 / \text{kJ}\cdot\text{mol}^{-1}$	$\Delta\Delta_{\text{fus}}S_m^0 / \text{J}\cdot\text{K}^{-1}\cdot\text{mol}^{-1}$
<b>1,8-diPhNaph</b>	$3.4 \pm 1.3$	$3.2 \pm 3.3$
<b>1,8-diPhAnth</b>	$1.2 \pm 0.9$	$4.1 \pm 2.0$

The values obtained clearly show that  $\Delta\Delta_{\text{fus}}H_m^0$  is minimal for 1,8-diPhAnth. This slight increase suggests inefficient crystal packing, which, as mentioned earlier, leads to less robust arrangements. The suboptimal arrangement of the crystal packing is a consequence of the introduction of substituents into the parent structure. While the parent structure, anthracene, inherently has a considerable number of  $\pi \cdots \pi$  interactions, the introduction of disubstituents leads to a reduction of these interactions within the anthracene core since they are blocking the formation of these interactions, which leads to less efficient packing. Conversely, the  $\Delta\Delta_{\text{fus}}S_m^0$  value is more significant. The interplay of a small increment of enthalpy and a bigger increment of entropy causes a decrease in  $T_{\text{fus}}$ , resulting in a lower  $T_{\text{fus}}$  compared to anthracene.

The small value of  $\Delta\Delta_{\text{fus}}H_m^0$  for 1,8-diPhAnth can be further explained by the X-Ray crystallographic structure shown in Figure 57, which shows the interactions that the compound establishes in its crystal packing. It can be well observed how the presence of the phenyl substituents blocks one edge of the anthracene core.

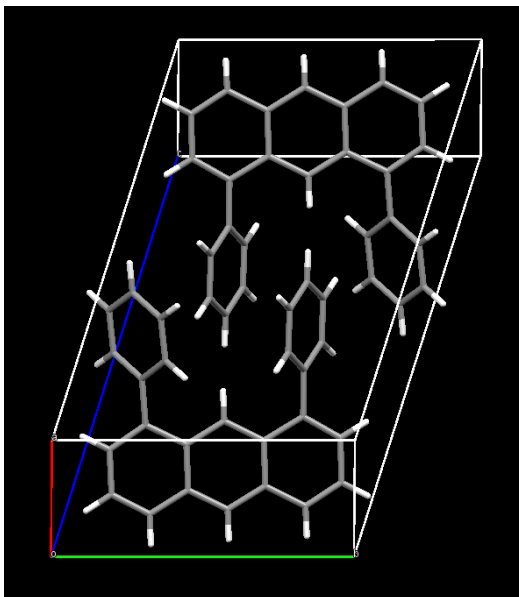


**Figure 57.** X-Ray taken on 1,8-diphenylanthracene that shows the packing of the compound and its molecular structure in the solid phase.

In the case of the compound 1,8-diPhNaph, the bigger value for  $\Delta\Delta_{\text{fus}}H_m^0$  indicates that, compared to 1,8-diPhAnth, the crystal packing of 1,8-diPhNaph is more efficient, making it more robust (shown in Figure 58). There appears to be a more substantial sacrifice of the intermolecular interactions related to the central acene core on going from anthracene to 1,8-diPhAnth than from naphthalene to 1,8-diPhNaph. The  $T_{\text{fus}}$  for 1,8-diPhNaph increases in relation to naphthalene because the  $\Delta\Delta_{\text{fus}}H_m^0$  and  $\Delta\Delta_{\text{fus}}S_m^0$  are similar, enabling the  $\Delta\Delta_{\text{fus}}H_m^0$  to rule over the increase of entropy.

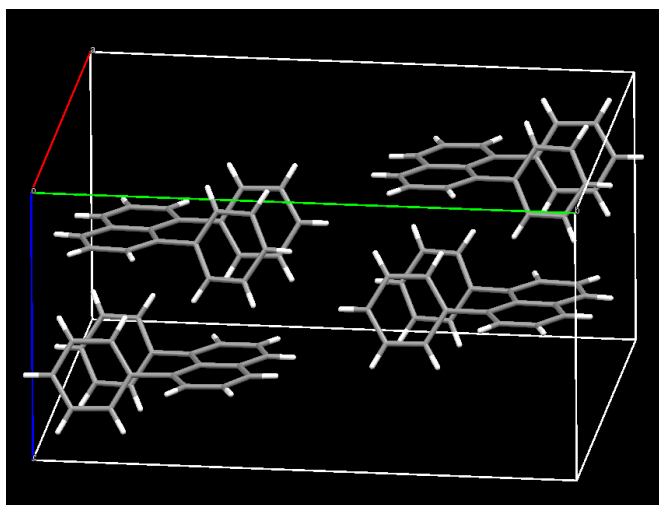


**Figure 58.** X-Ray taken on 1,8-diphenylnaphthalene that shows the packing of the compound and its molecular structure in the solid phase.

With Knudsen-Quartz Crystal, a lot of experimental data was obtained for the sublimation of anthracene derivatives. This data is presented in Table 6-8.

The Tables 9 to 11 show the sublimation properties at temperature  $\langle T \rangle$  of the 1,8-diarylanthracenes,  $\langle T \rangle$  is the average temperature of the experiments.

**Table 6.** Experimental results obtained for the sublimation of 1,8-diPhAnth, in the Knudsen-Quartz crystal effusion apparatus.

Exp.	$T / K$	$T^{-1} / K^{-1}$	$(df/dt)_{\text{corr}} / \text{Hz}\cdot\text{s}^{-1}$	$p / \text{Pa}$	$\ln(p / 1\text{Pa})$
1	410.09	0.0024385	-0.1676	0.0778	-2.5538
	412.00	0.0024272	-0.1999	0.0930	-2.3754
	413.95	0.0024157	-0.2405	0.1121	-2.1881
	415.93	0.0024043	-0.2903	0.1357	-1.9976
	417.90	0.0023929	-0.3486	0.1633	-1.8123
	419.87	0.0023817	-0.4182	0.1963	-1.6280
	421.85	0.0023705	-0.4997	0.2352	-1.4475
	423.82	0.0023595	-0.5957	0.2810	-1.2694
	425.81	0.0023485	-0.7079	0.3347	-1.0945
	$\Delta m / \text{mg}$	11.12	$W / \text{Hz}\cdot\text{mg}^{-1}$	714.5	
2	408.88	0.0024457	-0.1498	0.0659	-2.7192
	410.82	0.0024342	-0.1780	0.0785	-2.5446
	412.76	0.0024227	-0.2136	0.0944	-2.3597
	414.70	0.0024114	-0.2556	0.1133	-2.1780
	416.64	0.0024002	-0.3059	0.1359	-1.9960
	418.58	0.0023890	-0.3703	0.1648	-1.8028
	420.52	0.0023780	-0.4400	0.1963	-1.6279
	422.46	0.0023671	-0.5288	0.2365	-1.4417
		$\Delta m / \text{mg}$	7.94	$W / \text{Hz}\cdot\text{mg}^{-1}$	762.4

**Table 7.** Experimental results obtained for the sublimation of 1,8-bismethoxyPhAnth, in the Knudsen-Quartz crystal effusion apparatus.

Exp.	$T / K$	$T^{-1} / K^{-1}$	$(df/dt)_{\text{corr}} / \text{Hz}\cdot\text{s}^{-1}$	$p / \text{Pa}$	$\ln(p / 1\text{Pa})$
1	461.82	0.0021654	-0.3794	0.1718	-1.7616
	464.81	0.0021514	-0.4964	0.2255	-1.4896
	467.79	0.0021377	-0.6515	0.2968	-1.2146
	470.78	0.0021241	-0.8515	0.3892	-0.9437
	473.77	0.0021107	-1.1122	0.5100	-0.6733
	476.75	0.0020975	-1.4355	0.6603	-0.4150
	479.73	0.0020845	-1.8361	0.8472	-0.1658
	482.72	0.0020716	-2.2883	1.0592	0.0575
	$\Delta m / \text{mg}$	28.75	$W / \text{Hz}\cdot\text{mg}^{-1}$	706.9	
2	459.74	0.0021751	-0.3269	0.1	-1.9343
	462.72	0.0021611	-0.4328	0.1920	-1.6504
	465.72	0.0021472	-0.5686	0.2530	-1.3743
	468.70	0.0021336	-0.7475	0.3337	-1.0976
	471.67	0.0021201	-0.9821	0.4398	-0.8215
	474.64	0.0021069	-1.2881	0.5786	-0.5471
	477.63	0.0020937	-1.6824	0.7581	-0.2769
	480.59	0.0020808	-2.1854	0.9878	-0.0122
	483.57	0.0020680	-2.8393	1.2873	0.2526
	$\Delta m / \text{mg}$	38.58	$W / \text{Hz}\cdot\text{mg}^{-1}$	722.3	
3	456.90	0.0021887	-0.2685	0.1188	-2.1304
	458.88	0.0021792	-0.3164	0.1403	-1.9640
	460.85	0.0021699	-0.3790	0.1684	-1.7813
	462.84	0.0021606	-0.4528	0.2016	-1.6013
	464.82	0.0021514	-0.5413	0.2416	-1.4206
	466.80	0.0021422	-0.6528	0.2919	-1.2312
	468.78	0.0021332	-0.7839	0.3513	-1.0460
	470.76	0.0021242	-0.9394	0.4219	-0.8630
	472.75	0.0021153	-1.1256	0.5066	-0.6801
	$\Delta m / \text{mg}$	17.42	$W / \text{Hz}\cdot\text{mg}^{-1}$	721.5	

**Table 8.** Experimental results obtained for the sublimation of 1,8-dibiPhAnth, in the Knudsen-Quartz crystal effusion apparatus.

Exp.	$T / K$	$T^{-1} / K^{-1}$	$(df/dt)_{\text{corr}} / \text{Hz}\cdot\text{s}^{-1}$	$p / \text{Pa}$	$\ln(p / 1\text{Pa})$
1	505.93	0.0019766	-0.2272	0.0917	-2.3889
	507.96	0.0019687	-0.2741	0.1109	-2.1993
	509.97	0.0019609	-0.3279	0.1329	-2.0181
	511.98	0.0019532	-0.3917	0.1591	-1.8383
	513.99	0.0019456	-0.4688	0.1908	-1.6567
	516.00	0.0019380	-0.5592	0.2280	-1.4784
	518.00	0.0019305	-0.6693	0.2734	-1.2967
	$\Delta m / \text{mg}$	10.50	$W / \text{Hz}\cdot\text{mg}^{-1}$	770.0	
2	506.64	0.0019738	-0.2253	0.0951	-2.3530
	509.65	0.0019621	-0.2979	0.1261	-2.0707
	512.67	0.0019506	-0.3916	0.1663	-1.7942
	515.69	0.0019391	-0.5124	0.2182	-1.5224
	518.72	0.0019278	-0.6675	0.2851	-1.2551
	521.74	0.0019167	-0.8708	0.3730	-0.9863
	524.76	0.0019056	-1.1301	0.4854	-0.7228
	527.77	0.0018947	-1.4669	0.6319	-0.4590
	530.81	0.0018839	-1.8951	0.8187	-0.2001
		$\Delta m / \text{mg}$	23.80	$W / \text{Hz}\cdot\text{mg}^{-1}$	724.8
3	506.18	0.0019756	-0.2047	0.0829	-2.4903
	508.16	0.0019679	-0.2470	0.1002	-2.3005
	510.13	0.0019603	-0.2950	0.1199	-2.1209
	512.12	0.0019527	-0.3559	0.1450	-1.9313
	514.11	0.0019451	-0.4248	0.1734	-1.7524
	516.09	0.0019377	-0.5068	0.2072	-1.5740
	$\Delta m / \text{mg}$	9.21	$W / \text{Hz}\cdot\text{mg}^{-1}$	742.9	
4	506.52	0.0019743	-0.2278	0.0909	-2.3975
	508.51	0.0019665	-0.2740	0.1096	-2.2109
	510.51	0.0019588	-0.3290	0.1319	-2.0260
	512.53	0.0019511	-0.3944	0.1584	-1.8427
	514.55	0.0019434	-0.4693	0.1888	-1.6669
	516.57	0.0019359	-0.5599	0.2257	-1.4884
	518.60	0.0019283	-0.6670	0.2694	-1.3114
	520.60	0.0019208	-0.7908	0.3201	-1.1392
	522.62	0.0019134	-0.9363	0.3797	-0.9684
	$\Delta m / \text{mg}$	17.20	$W / \text{Hz}\cdot\text{mg}^{-1}$	767.4	

**Table 9.** Experimental results obtained for 1,8-diPhAnth, where  $a$  and  $b$  are from the Clausius-Clapeyron equation  $\ln(p / \text{Pa}) = b - a \cdot (K / T)$ , and  $a = \Delta_{\text{sub}}H^0 (<T>)/R$ .

Exp.	$b$	$a / \text{K}$	$R^2$	$<T> / \text{K}$	$\rho(<T>) / \text{Pa}$	$\Delta_{\text{sub}}H^0 (<T>) / \text{kJ}\cdot\text{mol}^{-1}$	$\Delta_{\text{sub}}S^0 (<T>) / \text{kJ}\cdot\text{mol}^{-1}$
1	$37.14 \pm 0.08$	$16279 \pm 32$	0.99997	417.91	0.1632	$135.4 \pm 0.3$	$213.1 \pm 0.6$
2	$37.14 \pm 0.25$	$16304 \pm 102$	0.99976	415.67	0.1250	$135.6 \pm 0.9$	$213.1 \pm 2.0$
<b>Global results</b>				416.79		$135.5 \pm 0.6$	$213.1 \pm 1.3$

**Table 10.** Experimental results obtained for 1,8-bismethoxyPhAnth, where  $a$  and  $b$  are from the Clausius-Clapeyron equation  $\ln(p / \text{Pa}) = b - a \cdot (K / T)$ , and  $a = \Delta_{\text{sub}}H^0 (<T>)/R$ .

Exp.	$b$	$a / \text{K}$	$R^2$	$<T> / \text{K}$	$\rho(<T>) / \text{Pa}$	$\Delta_{\text{sub}}H^0 (<T>) / \text{kJ}\cdot\text{mol}^{-1}$	$\Delta_{\text{sub}}S^0 (<T>) / \text{kJ}\cdot\text{mol}^{-1}$
1	$40.64 \pm 0.32$	$19580 \pm 150$	0.99965	472.27	0.4417	$162.8 \pm 1.2$	$242.2 \pm 2.6$
2	$42.47 \pm 0.09$	$20416 \pm 43$	0.99960	467.20	0.2919	$169.7 \pm 0.4$	$257.4 \pm 0.8$
3	$41.38 \pm 0.33$	$19889 \pm 151$	0.99959	464.82	0.2447	$165.4 \pm 1.3$	$248.3 \pm 2.7$
<b>Global results</b>				468.10		$166.0 \pm 1.0$	$249.3 \pm 2.0$

**Table 11.** Experimental results obtained for 1,8-dibiPhAnth, where  $a$  and  $b$  are from the Clausius-Clapeyron equation  $\ln(p / \text{Pa}) = b - a \cdot (K / T)$ , and  $a = \Delta_{\text{sub}}H^0 (<T>)/R$ .

Exp.	$b$	$a / \text{K}$	$R^2$	$<T> / \text{K}$	$\rho(<T>) / \text{Pa}$	$\Delta_{\text{sub}}H^0 (<T>) / \text{kJ}\cdot\text{mol}^{-1}$	$\Delta_{\text{sub}}S^0 (<T>) / \text{kJ}\cdot\text{mol}^{-1}$
1	$44.33 \pm 0.10$	$23637 \pm 52$	0.99998	512.00	0.1594	$196.5 \pm 0.4$	$272.9 \pm 0.9$
2	$44.88 \pm 0.04$	$23929 \pm 23$	0.99999	514.19	0.1903	$198.6 \pm 0.2$	$276.7 \pm 0.4$
3	$45.21 \pm 0.16$	$24145 \pm 81$	0.99995	511.13	0.1318	$200.8 \pm 0.7$	$280.2 \pm 1.3$
4	$43.94 \pm 0.13$	$23467 \pm 64$	0.99994	514.56	0.1887	$195.1 \pm 0.5$	$269.6 \pm 1.0$
<b>Global Results</b>				512.97		$197.7 \pm 0.5$	$274.8 \pm 0.9$

The graphical representations of the natural logarithm of the equilibrium vapor pressure,  $\ln(p/\text{Pa})$ , as a function of  $(1/T)$  were then obtained for the compounds studied. The results are presented in Figures 59-61.

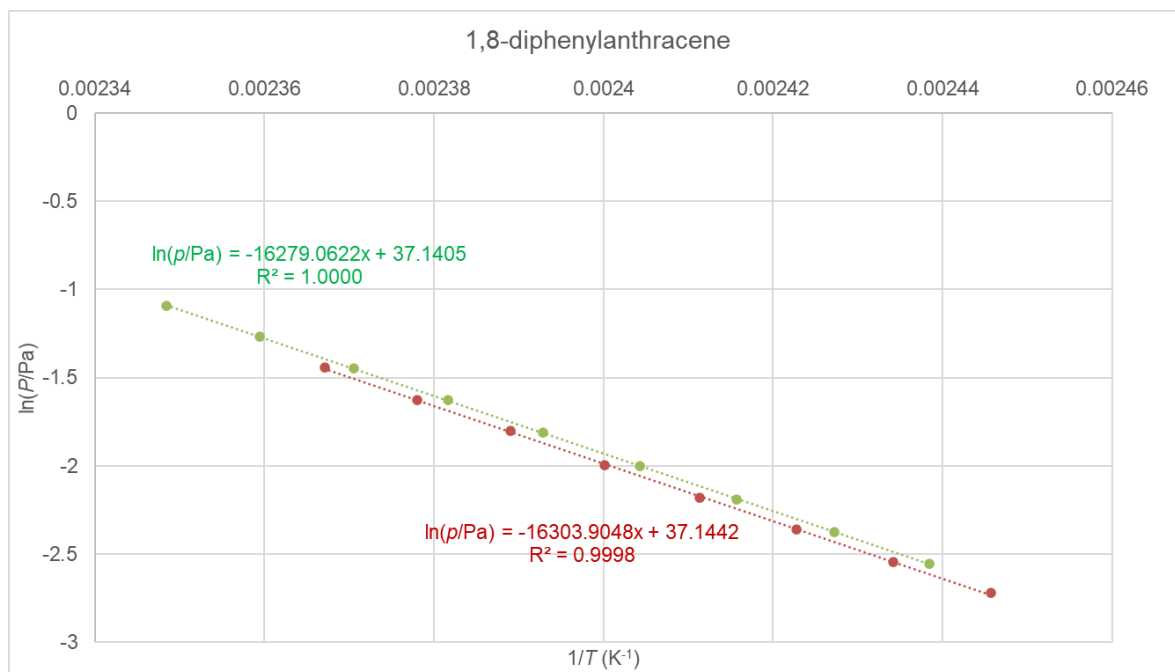


**Figure 59.** Graphical representation of the  $\ln(P/\text{Pa})=f(1/T)$  for the experiments of 1,8-diPhAnth using the Knudsen-Quartz Crystal method.

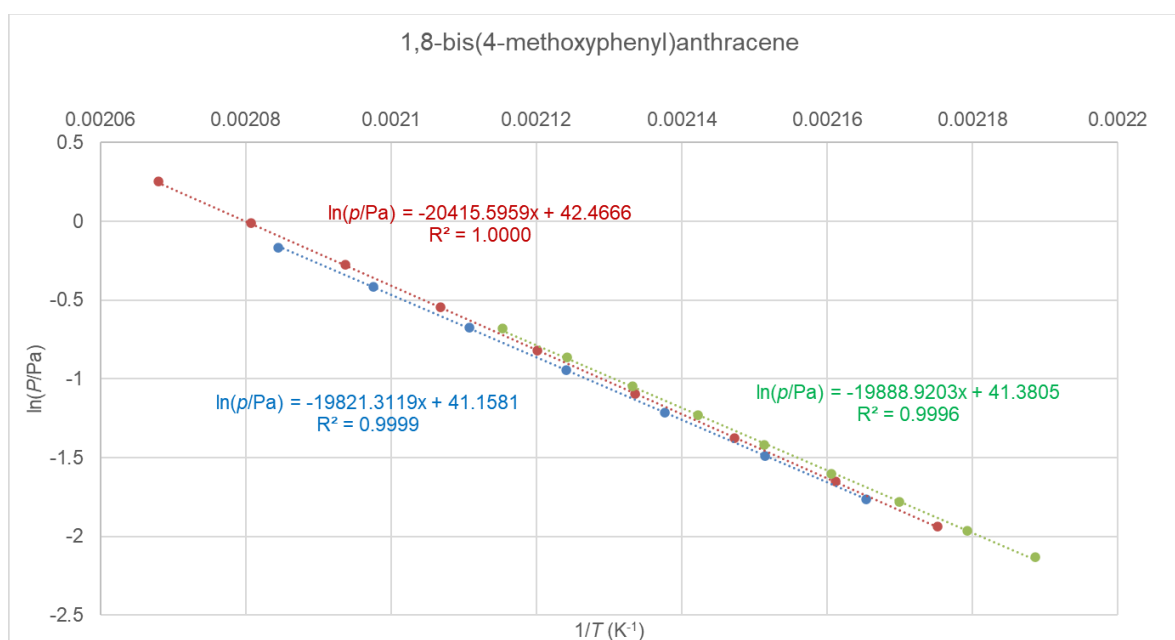


**Figure 60.** Graphical representation of the  $\ln(P/\text{Pa})=f(1/T)$  for the experiments of 1,8-bismethoxyPhAnth using the Knudsen-Quartz Crystal method.

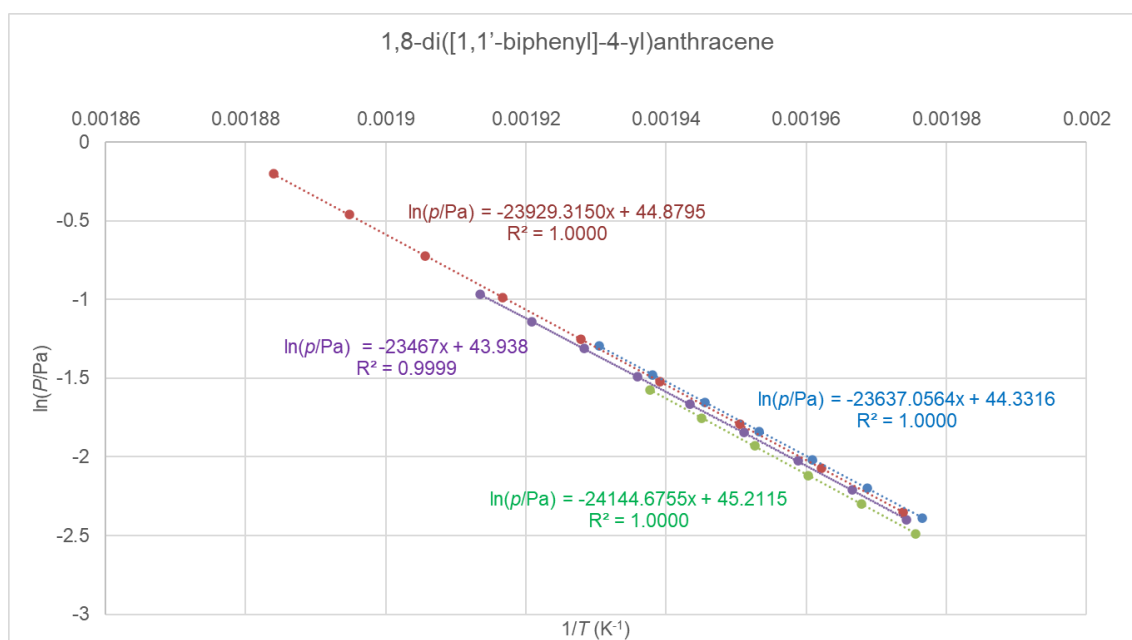


**Figure 61.** Graphical representation of the  $\ln(P/Pa)=f(1/T)$  for the experiments of 1,8-dibiPhAnth using the Knudsen-Quartz Crystal method.

The values of the changes in enthalpy, entropy, and Gibbs's energy of sublimation at 298.15 K for the compounds studied, were calculated using the equations previously mentioned (Eq. 10-17 and Eq. 84-85). The results are presented in Table 12. The thermodynamic values were corrected to  $T = 298.15$  K, using  $\Delta_{\text{sub}}Cp_m^0 = -26.1 \text{ J}\cdot\text{K}^{-1}\cdot\text{mol}^{-1}$ , a typical value for this type of compounds [41].

**Table 12.** Global results for the enthalpies, entropies, and Gibbs energies of sublimation at  $T = 298.15$  K.

Compound	$\Delta_{\text{sub}}H^0 / \text{kJ}\cdot\text{mol}^{-1}$	$\Delta_{\text{sub}}S^0 / \text{J}\cdot\text{K}^{-1}\cdot\text{mol}^{-1}$	$\Delta_{\text{sub}}G^0 / \text{kJ}\cdot\text{mol}^{-1}$
Naphthalene <sup>[80]</sup>	$72.7 \pm 0.0$	$168.1 \pm 0.1$	$22.6 \pm 0.1$
Anthracene <sup>[60]</sup>	$101.2 \pm 0.6$	$185.6 \pm 1.8$	$45.9 \pm 0.8$
1-methoxyPhNaph <sup>[1]</sup>	$122.3 \pm 0.6$	$236.9 \pm 1.9$	$51.6 \pm 0.8$
1-biPhNaph <sup>[41]</sup>	$138.9 \pm 0.8$	$245.0 \pm 2.1$	$65.9 \pm 1.0$
1,8-diPhNaph <sup>[41]</sup>	$126.4 \pm 0.5$	$230.9 \pm 1.4$	$57.6 \pm 0.7$
1,8-bismethoxyPhNaph <sup>[1]</sup>	$144.9 \pm 0.8$	$252.1 \pm 2.3$	$69.7 \pm 1.1$
1,8-dibiPhNaph <sup>[41]</sup>	$178.5 \pm 1.1$	$280.2 \pm 2.7$	$95.0 \pm 1.4$
1,8-diPhAnth	$138.5 \pm 1.1$	$222.5 \pm 3.0$	$72.2 \pm 1.4$
1,8-bismethoxyPhAnth	$171.9 \pm 1.7$	$265.1 \pm 4.2$	$92.9 \pm 2.1$
1,8-dibiPhAnth	$206.1 \pm 1.8$	$295.5 \pm 4.4$	$118.0 \pm 2.2$

In Table 12, there are no results for the compound 1-PhNaph because this compound, at room's temperature, is a liquid.

Looking at the results in Table 12, the introduction of substituents into the backbones of naphthalene and anthracene led to a noticeable increase in Gibbs energy values. This increase, in turn, resulted in the monosubstituted and disubstituted compounds derived from these parent structures being significantly less volatile. A similar trend is evident when the  $\Delta_{\text{sub}}G^0$  values of 1,8-diarylnaphthalenes are examined in comparison to their monosubstituted counterparts. Being compounds of relatively low polarity and absence of hydrogen bonds, volatility is mostly ruled by molecular size. Bigger molecules have higher  $\Delta_{\text{sub}}H^0$  and  $\Delta_{\text{sub}}S^0$ . The enthalpic contribution dominates and hence  $\Delta_{\text{sub}}G^0$  increases with molecular size.

In the range of 1,8-diarylanthracenes, it can be seen that the molecules 1,8-bismethoxyPhAnth and 1,8-dibiPhAnth exhibit significantly lower volatility compared to 1,8-diPhAnth. This lower tendency to sublime is due to the presence of additional -R groups in the substituents in the former compounds, distinguishing them from 1,8-diPhAnth in this respect. The higher polarity imported by the 4-methoxyphenyl group appears to also contribute to increase  $\Delta_{\text{sub}}H^0$ .

Table 13 shows the increment in the enthalpies,  $\Delta\Delta_{\text{sub}}H_m^0$ , and entropies,  $\Delta\Delta_{\text{sub}}S_m^0$ , of sublimation per aryl group for the compounds studied, at  $T = 298.15$  K, calculated as ( $n$  is the number of aryl groups in the molecule):

$$\Delta\Delta_{\text{sub}}H_m^0 = \frac{(\Delta_{\text{sub}}H_m^0(\textit{substituted compound})) - (\Delta_{\text{sub}}H_m^0(\textit{parent compound}))}{n} \quad \text{Eq. 52}$$

$$\Delta\Delta_{\text{sub}}S_m^0 = \frac{(\Delta_{\text{sub}}S_m^0(\textit{substituted compound})) - (\Delta_{\text{sub}}S_m^0(\textit{parent compound}))}{n} \quad \text{Eq. 53}$$

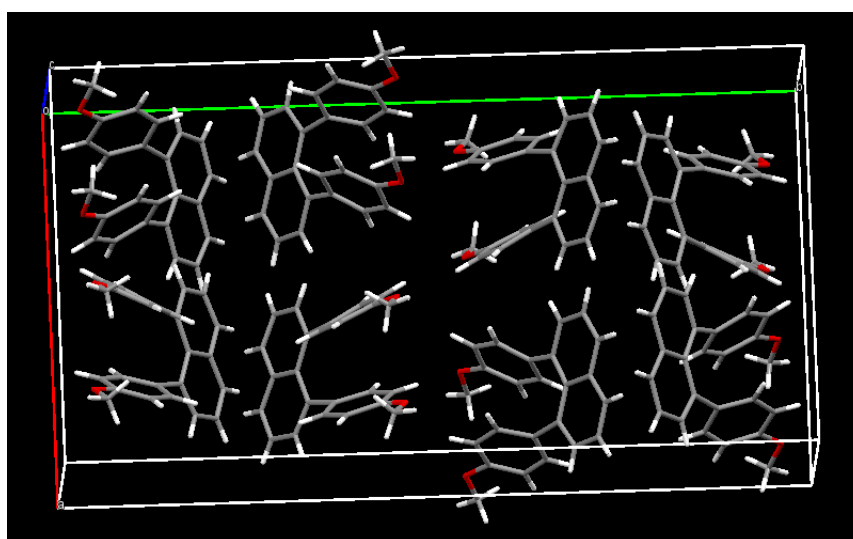
**Table 13.** Increments in the enthalpy and entropy of sublimation, at  $T = 298.15$  K, per substituent in the compounds studied.

Compound	$\Delta\Delta_{\text{sub}}H_m^0 / \text{kJ}\cdot\text{mol}^{-1}$	$\Delta\Delta_{\text{sub}}S_m^0 / \text{J}\cdot\text{K}^{-1}\cdot\text{mol}^{-1}$
1-methoxyPhNaph <sup>[1]</sup>	$49.6 \pm 0.3$	$68.8 \pm 1.0$
1-biPhNaph <sup>[41]</sup>	$66.2 \pm 0.4$	$76.9 \pm 1.1$
1,8-diPhNaph <sup>[41]</sup>	$26.9 \pm 0.3$	$31.4 \pm 0.8$
1,8-bismethoxyPhNaph <sup>[1]</sup>	$36.1 \pm 0.4$	$42.0 \pm 1.2$
1,8-dibiPhNaph <sup>[41]</sup>	$52.9 \pm 0.6$	$56.1 \pm 1.4$
1,8-diPhAnth	$18.7 \pm 0.9$	$18.5 \pm 2.4$
1,8-bismethoxyPhAnth	$35.4 \pm 1.1$	$39.8 \pm 3.0$
1,8-dibiPhAnth	$52.5 \pm 1.2$	$55.0 \pm 3.1$

With the values presented in Table 13, the increase of the various properties of sublimation are expected as previously seen in Table 12.

The  $\Delta\Delta_{\text{sub}}H_m^0$  values observed for disubstituted naphthalenes are low compared to their monosubstituted counterparts. This is because the two aryl substituents are adjacent and close to each other, effectively shielding two  $\pi$ -faces from intermolecular contacts.

The previous statement is further proven with their X-Ray crystallographic structures shown in Figure 58, Figure 62, and Figure 63, which shows the interactions that the compounds establish in its crystal packing.

**Figure 62.** X-Ray taken on 1,8-bis(4-methoxyphenyl)naphthalene that shows the packing of the compound and its molecular structure in the solid phase.

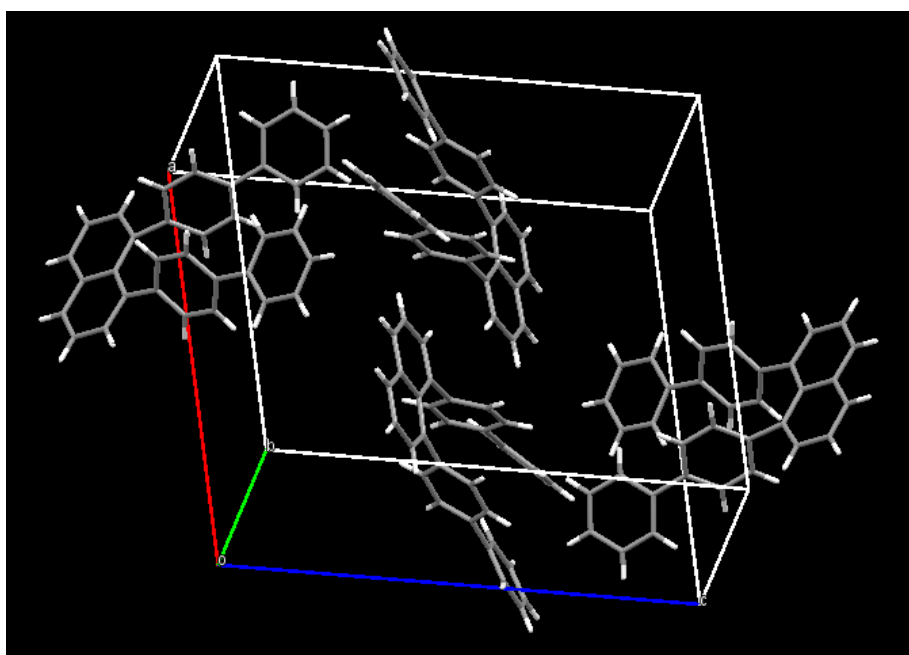


**Figure 63.** X-Ray taken on 1,8-di([1,1'-biphenyl]-4-yl)naphthalene that shows the packing of the compound and its molecular structure in the solid phase.

Among the 1,8-diarylnaphthalenes, the compound 1,8-dibiPhNaph stands out conspicuously due to its notably elevated increment of enthalpy of sublimation compared to the other 1,8-diarylnaphthalenes. This result highlights the fact that the biphenyl substituent contributes to a more stable and robust crystal packing than other substituents in this context (Figure 63). Conversely, the  $\Delta\Delta_{\text{sub}}S_m^0$  of 1,8-dibiPhNaph also exceeds that of the other naphthalene derivatives. This increased entropy is due to the larger number of molecular vibrations in the larger molecule, which includes the relatively flexible internal rotation of the phenyl groups. The same reasoning can be applied to 1,8-dibiPhAnth compared to the other 1,8-diarylanthracenes.

The increment values observed for 1,8-dibiPhAnth and 1,8-bismethoxyPhAnth (shown in Figure 64) closely match those of their 1,8-diarylnaphthalene counterparts. This observation underscores the fact that these two substituents, biphenyl and 4-methoxyphenyl, exert a similar and consistent influence on the sublimation properties in both aromatic systems. This consistency suggests that the influence of biphenyl and 4-methoxyphenyl groups on the sublimation behavior of aromatic compounds remains predictable and consistent, regardless of the parent structure (whether anthracene or naphthalene).

In contrast, the compound 1,8-diPhAnth, as shown in Figure 57, deviates from the anticipated pattern by exhibiting unequal sublimation increment values compared to 1,8-diPhNaph, with the former exhibiting lower values of the increments. This deviation contradicts the previously discussed expectation of a predictable and consistent behavior. The modest  $\Delta\Delta_{\text{sub}}H_m^\circ$  value for 1,8-diPhAnth suggests that its crystal packing is less efficient compared to the other compounds. This lower  $\Delta\Delta_{\text{sub}}H_m^\circ$  comes associated with a lower  $\Delta\Delta_{\text{sub}}S_m^\circ$ , suggesting a weaker and looser packing of 1,8-diPhAnth.

In principle, since anthracene is larger than naphthalene, the effect of blocking one edge of the molecule with phenyl substituents should be more dramatic, since a larger area of the acene core is precluded from intermolecular interactions. However, this does not hold for the other two -R groups studied (4-methoxyphenyl and biphen-4-yl). Hence, the following hypothesis can be considered: there are two opposing effects; while the two substituents have a more harmful impact on the bigger anthracene core, their larger intermolecular distance allow for more intermolecular interactions involving the aryl groups. In the smaller aryl groups (phenyl) the harmful effect prevails.

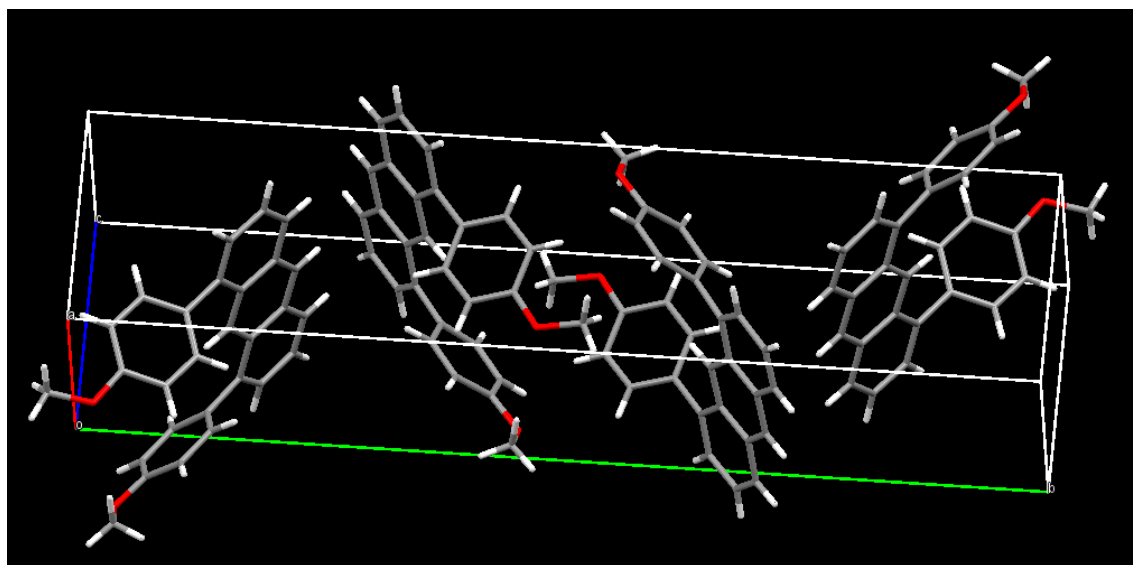


**Figure 64.** X-Ray taken on 1,8-bis(4-methoxyphenyl)anthracene that shows the packing of the compound and its molecular structure in the solid phase.

## Molecular Energetics

The general combustion results for the compounds studied using Mini-bomb Combustion Calorimetry are presented from Table 14 to Table 16. In these tables  $m(\text{cpd.})$  is the mass of the compound burnt in each experiment;  $m(\text{BA})$  is the mass of benzoic acid used as combustion auxiliary;  $T_i$  is the initial temperature;  $T_f$  is the final temperature;  $\varepsilon_i(\text{cont.})$  is the energy equivalent of the contents in the initial state;  $\varepsilon_f(\text{cont.})$  is the energy equivalent of the contents in the final state;  $\Delta T_{\text{ad}}$  is the corrected adiabatic temperature rise;  $\Delta U(\text{IBP})$  is the energy change for the isothermal bomb process;  $\Delta U(\text{BA})$  is the energy of combustion of benzoic acid;  $\Delta U(\text{ignition})$  is the electric energy for the ignition;  $\Delta U_{\Sigma}$  represents the standard state corrections;  $\Delta U(\text{carbon})$  is the energy of combustion of the carbon residue formed;  $\Delta_c u^0$  is the standard massic energy of combustion. The final result is presented as  $\langle \Delta_c u^0 \rangle \pm \sigma_m(\Delta_c u^0)$ . The error in the form of % is calculated as:

$$\% \text{ error} = \frac{\sigma_m(\Delta_c u^0)}{\langle \Delta_c u^0 \rangle} \quad \text{Eq. 54}$$

**Table 14.** Experimental results for the combustion of 1,8-diphenylanthracene, at  $T = 298.15$  K.

	<b>1</b>	<b>2</b>	<b>3</b>	<b>4</b>	<b>5</b>	<b>6</b>	<b>7</b>
<b><math>m(\text{cpd.}) / \text{mg}</math></b>	11.4341	17.7180	11.0026	11.0072	16.3428	14.4247	18.1087
<b><math>m(\text{BA}) / \text{mg}</math></b>	–	–	–	–	–	–	–
<b><math>T_i / \text{K}</math></b>	298.0805	298.0671	298.0846	298.0768	298.0647	298.0692	298.0685
<b><math>T_f / \text{K}</math></b>	298.2965	298.3904	298.2921	298.2858	298.3663	298.3384	298.3989
<b><math>\Delta T_{\text{ad}} / \text{K}</math></b>	0.232751	0.360683	0.223928	0.224223	0.332388	0.293741	0.368506
<b><math>\varepsilon_i (\text{cont.}) / \text{J}\cdot\text{K}^{-1}</math></b>	0.973	0.980	0.972	0.972	0.978	0.976	0.980
<b><math>\varepsilon_f (\text{cont.}) / \text{J}\cdot\text{K}^{-1}</math></b>	0.990	1.006	0.988	0.989	1.002	0.997	1.007
<b><math>-\Delta U(\text{IBP}) / \text{J}</math></b>	-452.164	-701.453	-434.981	-435.579	-646.326	-571.046	-716.671
<b><math>-\Delta U(\text{BA}) / \text{J}</math></b>	–	–	–	–	–	–	–
<b><math>-\Delta U(\text{ignition}) / \text{J}</math></b>	1.305	1.272	1.298	1.274	1.269	1.251	1.294
<b><math>\Delta U\Sigma / \text{J}</math></b>	0.244	0.391	0.235	0.235	0.359	0.314	0.401
<b><math>-\Delta U(\text{carbon}) / \text{J}</math></b>	0.261	0.059	0.399	0.092	0.129	0.063	0.106
<b><math>-\Delta_c U^0(\text{cpd.}) / \text{J}\cdot\text{g}^{-1}</math></b>	-39546.684	-39570.991	-39549.242	-39559.113	-39533.954	-39570.537	-39559.850
<b><math>-\langle \Delta_c U^0 \rangle / \text{J}\cdot\text{g}^{-1} = 39555.8 \pm 5.1 (0.013\%)</math></b>							

**Table 15.** Experimental results for the combustion of 1,8-bis(4-methoxyphenyl)anthracene, at  $T = 298.15$  K.

	<b>1</b>	<b>2</b>	<b>3</b>	<b>4</b>	<b>5</b>	<b>6</b>	<b>7</b>	<b>8</b>
<b><math>m(\text{cpd.}) / \text{mg}</math></b>	13.6239	11.5211	13.2569	15.9299	13.6808	9.7316	21.2392	17.5936
<b><math>m(\text{BA}) / \text{mg}</math></b>	–	–	–	–	–	–	–	–
<b><math>T_i / \text{K}</math></b>	298.0658	298.0633	298.0684	298.0626	298.0600	298.0619	298.0657	298.0600
<b><math>T_f / \text{K}</math></b>	298.3028	298.2658	298.2977	298.3316	298.2960	298.2376	298.4180	298.3558
<b><math>\Delta T_{\text{ad}} / \text{K}</math></b>	0.252726	0.213650	0.246092	0.295503	0.253942	0.180657	0.394179	0.326391
<b><math>\varepsilon_i (\text{cont.}) / \text{J}\cdot\text{K}^{-1}</math></b>	0.976	0.974	0.976	0.979	0.976	0.972	0.985	0.981
<b><math>\varepsilon_f (\text{cont.}) / \text{J}\cdot\text{K}^{-1}</math></b>	0.996	0.990	0.995	1.002	0.996	0.986	1.016	1.006
<b><math>-\Delta U(\text{IBP}) / \text{J}</math></b>	-490.896	-414.982	-478.204	-574.313	-493.516	-350.737	-766.752	-634.585
<b><math>-\Delta U(\text{BA}) / \text{J}</math></b>	–	–	–	–	–	–	–	–
<b><math>-\Delta U(\text{ignition}) / \text{J}</math></b>	1.491	1.271	1.258	1.418	1.241	1.236	1.237	1.327
<b><math>\Delta U\Sigma / \text{J}</math></b>	0.272	0.228	0.265	0.322	0.274	0.190	0.440	0.359
<b><math>-\Delta U(\text{carbon}) / \text{J}</math></b>	0.676	0.736	0.119	0.221	0.297	0.208	0.241	0.594
<b><math>-\Delta_c u^0(\text{cpd.}) / \text{J}\cdot\text{g}^{-1}</math></b>	-36061.678	-36063.552	-36061.145	-36046.218	-36075.208	-36042.888	-36091.340	-36082.375
<b><math>-\langle \Delta_c u^0 \rangle / \text{J}\cdot\text{g}^{-1} = 36065.6 \pm 5.9 (0.016\%)</math></b>								

**Table 16.** Experimental results for the combustion of 1,8-di([1,1'-biphenyl]-4-yl)anthracene, at  $T = 298.15$  K.

	<b>1</b>	<b>2</b>	<b>3</b>	<b>4</b>	<b>5</b>	<b>6</b>	<b>7</b>
<b><math>m(\text{cpd.}) / \text{mg}</math></b>	23.0143	20.0194	13.6303	11.8078	16.4749	22.0653	20.1528
<b><math>m(\text{BA}) / \text{mg}</math></b>	–	–	–	–	–	–	–
<b><math>T_i / \text{K}</math></b>	298.0660	298.0618	298.0639	298.0644	298.0649	298.0679	298.0660
<b><math>T_f / \text{K}</math></b>	298.4763	298.4236	298.3178	298.2875	298.3674	298.4623	298.4273
<b><math>\Delta T_{\text{ad}} / \text{K}</math></b>	0.466961	0.406417	0.276860	0.239718	0.334293	0.447739	0.409172
<b><math>\varepsilon_i (\text{cont.}) / \text{J}\cdot\text{K}^{-1}</math></b>	0.985	0.982	0.975	0.973	0.978	0.984	0.982
<b><math>\varepsilon_f (\text{cont.}) / \text{J}\cdot\text{K}^{-1}</math></b>	1.019	1.011	0.995	0.990	1.002	1.016	1.012
<b><math>-\Delta U(\text{IBP}) / \text{J}</math></b>	-908.506	-790.508	-538.081	-465.725	-650.028	-871.063	-795.852
<b><math>-\Delta U(\text{BA}) / \text{J}</math></b>	–	–	–	–	–	–	–
<b><math>-\Delta U(\text{ignition}) / \text{J}</math></b>	1.286	1.323	1.326	1.318	1.278	1.278	1.346
<b><math>\Delta U\Sigma / \text{J}</math></b>	0.522	0.448	0.296	0.254	0.363	0.499	0.452
<b><math>-\Delta U(\text{carbon}) / \text{J}</math></b>	0.290	0.317	0.162	0.135	0.168	0.079	0.188
<b><math>-\Delta_c u^0(\text{cpd.}) / \text{J}\cdot\text{g}^{-1}</math></b>	-39465.672	-39480.442	-39466.969	-39432.106	-39443.779	-39457.562	-39477.749
<b><math>-\langle \Delta_c u^0 \rangle / \text{J}\cdot\text{g}^{-1} = 39460.6 \pm 6.7 (0.017\%)</math></b>							

Table 17 presents the calculated electronic energies,  $E_{el}$ , at  $T = 0$  K, for the equilibrium conformations of the studied compounds, found in the optimization calculations. Table 17 also contains enthalpy values, denoted as  $H_{298.15}$  at the temperature of  $T = 298.15$  K, for the compounds, obtained by unscaled frequency calculations. The relative molecular complexity of the molecules presents a challenge in their conformational analysis. This complexity arises from the presence of flexible groups such as phenyl, methoxy, and biphenyl, which carry the possibility for multiple energy minima within the corresponding Potential Energy Surface (PES). Some of these minima may have very close energy values, significantly increasing the number of calculations required to comprehensively explore the relevant dimensions of PES.

The compounds present in Table 17 can exist in several conformations. There are two major conformers in 1,8-diarylanthracenes that are the parallel displaced conformation and a V-shaped conformation (shown in Figure 65). For these two conformations of the 1,8-diarylanthracenes, computational studies were made, and it was found that they are nearly isoenergetic. For this reason, only the most stable conformations are in Table 17 and all the computed enthalpies of reaction were made considering these conformers.

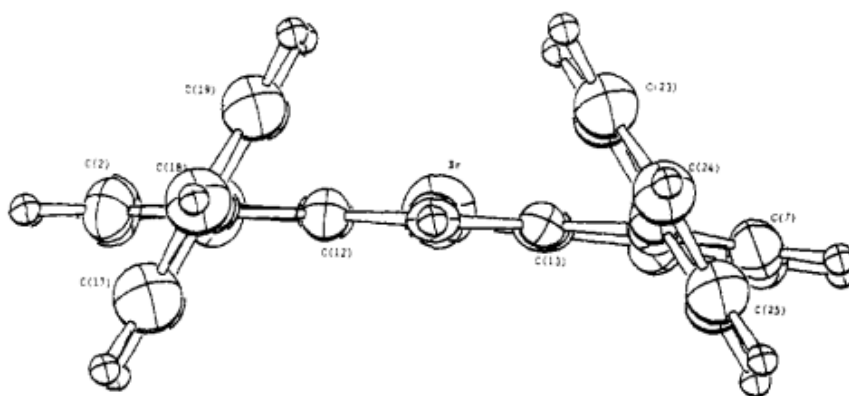


**Figure 65.** View from the top of the molecular structure of 10-bromo-1,8-diphenylanthracene [84].

**Table 17.** Raw computational data obtained for each compound.  $H_{298.15}$  corresponds to the sum of electronic,  $E_{el}$ , and thermal enthalpies. Optimization and frequency calculations were made using M06-2X/6-31+G(d,p). The CCSD(T) results are single-point energy calculations on MP2/cc-pVDZ optimized geometries.

<b>Molecule</b>	<b><math>H_{298.15}</math> / Hartree particle<sup>-1</sup></b>	<b><math>E_{el}</math> / Hartree particle<sup>-1</sup></b>	<b><math>E_{el}</math> (CCSD(T)) / Hartree particle<sup>-1</sup></b>
<b>Naphthalene</b>	-385.58393	-385.73996	-384.79546
<b>Anthracene</b>	-539.11545	-539.32093	-538.00238
<b>1-PhNaph</b>	-616.46787	-616.71058	-615.20188
<b>1-methoxyPhNaph</b>	-730.91511	-731.19349	
<b>4-Naph-1-BenzAl</b>	-729.74342	-729.99774	
<b>1-biPhNaph</b>	-847.35466	-847.68312	
<b>1,8-diPhNaph</b>	-847.34741	-847.67534	-845.60241
<b>1,8-bismethoxyPhNaph</b>	-1076.24240	-1076.64188	
<b>4,4'-Naph-1,8-diBenzAl</b>	-1073.90064	-1074.25200	
<b>1,8-dibiPhNaph</b>	-1309.12285	-1309.62366	
<b>1,8-diPhAnth</b>	-1000.88470	-1001.26304	-998.81736
<b>1,8-bismethoxyPhAnth</b>	-1229.77947	-1230.22899	
<b>4,4'-Anth-1,8-diBenzAl</b>	-1227.43608	-1227.83702	
<b>1,8-dibiPhAnth</b>	-1462.66211	-1463.21258	
<b>9,10-diPhAnth</b>	-1000.88245	-1001.25952	-998.81494

Table 18 shows the values of the enthalpies of combustion,  $\Delta_{\text{comb}}H^0(\text{cr})$ , and the derived enthalpies of formation,  $\Delta_fH^0(\text{cr})$ , in the crystal phase for the compounds studied by combustion calorimetry alongside the reference compounds. Table 19 shows the experimental values for the standard molar enthalpies of formation in the gas phase,  $\Delta_fH^0(\text{g})$ , for the compounds studied.

The  $\Delta_fH^0(\text{g})$  of the compounds were calculated using the following equation:

$$\Delta_fH^0(\text{g}) = \Delta_fH^0(\text{cr}) + \Delta_{\text{sub}}H^0 \quad \text{Eq. 55}$$

In order to apply Eq. 55 correctly, it is imperative to make sure that  $\Delta_f H^\circ(\text{cr})$  and  $\Delta_{\text{sub}} H^\circ$  were measured for the same solid phase. To this end, the following procedures were employed:

- The same sublimed sample of a compound for the Knudsen and combustion experiments was used.
- For 1,8-diPhAnth, the samples were verified by DSC, to confirm that no phase transition occurred between room temperature and the melting point.
- For 1,8-dibiPhAnth an additional set of combustion experiments was performed with the remaining sample from the Knudsen measurements (showing concordant results with the original sample).

**Table 18.** Standard molar enthalpies of combustion, as measured by mini-bomb combustion calorimetry, and derived standard molar enthalpies of formation of the compounds studied in the crystal phase, at  $T = 298.15$  K.

Compound	$-\Delta_{\text{comb}} H^\circ(\text{cr}) / \text{kJ}\cdot\text{mol}^{-1}$	$\Delta_f H^\circ(\text{cr}) / \text{kJ}\cdot\text{mol}^{-1}$
Naphthalene <sup>[78]</sup>	–	$79.0 \pm 1.8$
Anthracene <sup>[78]</sup>	–	$124.4 \pm 2.8$
1-PhNaph	–	–
1-methoxyPhNaph <sup>[1]</sup>	$8671.9 \pm 2.4$	$-18.6 \pm 3.3$
1-biPhNaph <sup>[41]</sup>	$11155.8 \pm 3.0$	$212 \pm 4.2$
1,8-diPhNaph <sup>[41]</sup>	$11187.4 \pm 3.2$	$243.5 \pm 4.3$
1,8-bismethoxyPhNaph <sup>[1]</sup>	$12218.2 \pm 3.4$	$-84.3 \pm 4.6$
1,8-dibiPhNaph <sup>[41]</sup>	$17186.0 \pm 4.8$	$376.7 \pm 6.5$
1,8-diPhAnth	$13081.5 \pm 4.6$	$277.8 \pm 5.7$
1,8-bismethoxyPhAnth	$14094.1 \pm 5.7$	$-68.4 \pm 6.8$
1,8-dibiPhAnth	$19060.7 \pm 7.9$	$391.6 \pm 9.4$

**Table 19.** Experimental values of  $\Delta_f H^0(g)$  for the compounds studied.

Compound	$\Delta_f H^0(g) / \text{kJ}\cdot\text{mol}^{-1}$
Benzene <sup>[78]</sup>	82.9 ± 0.9
Biphenyl <sup>[78,81]</sup>	182 ± 0.7
Naphthalene <sup>[80]</sup>	150.6 ± 1.5
Anthracene <sup>[78]</sup>	229.4 ± 2.9
1-PhNaph <sup>[41]</sup>	252.3 ± 3.4
1-methoxyPhNaph <sup>[1]</sup>	103.7 ± 3.4
1-biPhNaph <sup>[41]</sup>	350.9 ± 4.3
1,8-diPhNaph <sup>[41]</sup>	369.9 ± 4.3
1,8-bismethoxyPhNaph <sup>[1]</sup>	60.6 ± 4.7
1,8-dibiPhNaph <sup>[41]</sup>	555.2 ± 6.6
1,8-diPhAnth	416.3 ± 5.8
1,8-bismethoxyPhAnth	103.5 ± 7.0
1,8-dibiPhAnth	597.7 ± 9.6
9,10-diPhAnth <sup>[82]</sup>	435.2 ± 5.2

The results presented in Table 19 shows a significant difference in  $\Delta_f H^0(g)$  value between the isomers 1,8-diPhAnth and 9,10-diPhAnth. These two molecules have similar structures, with the only difference being the positional arrangement of their substituents. The difference in  $\Delta_f H^0(g)$  of 19.2  $\text{kJ}\cdot\text{mol}^{-1}$  clearly indicates a pronounced stabilization in 1,8-diPhAnth. When the substituents are shifted from positions 9,10 to positions 1,8, they assume a parallel orientation to each other. In this parallel configuration, the substituents engage in  $\pi \cdots \pi$  interactions, which in turn increase the stability of the molecule.

Figure 66 shows the PES for two different configurations (T-shaped and parallel displaced) of the benzene dimers in the gas phase. The lines are potentials calculated through computational methods [11,14]. The blue and red dots correspond to experimental data acquired in the literature [41,83]. The green dot corresponds to the experimental data obtained in this work.

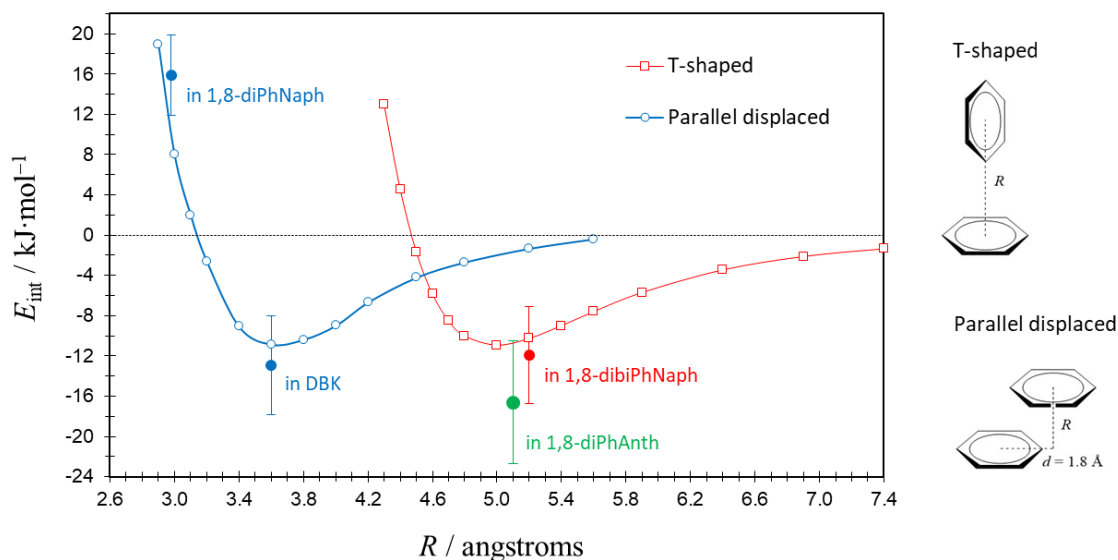


**Figure 66.** Left) Graphical representation of PES for the configurations T-shaped and Parallel displaced. Right) Visual representation of two configurations: up) T-shaped configuration; down) Parallel displaced [11,14,41,83].

A close examination of the reported structures reveals that both 1,8-diPhNaph and DBK (dibenzyl ketone) adopt a parallel displaced configuration [41,83]. A similar observation can be made for 1,8-dibiPhNaph, which has a T-shaped configuration [41]. Their respective positions along the potential line provide information about the strength of the aromatic interactions in these molecules. In particular, a higher  $E_{int}$  value indicates weaker interactions, while a lower  $E_{int}$  value indicates stronger interactions. In the case of 1,8-diPhNaph, its position on the potential line indicates that aromatic interactions are repulsive at such close distances.

In the case of 1,8-diPhAnth, it displays the strongest stabilizing interaction, but its situation is a little different from the other molecules. Although it shares a similar structural framework with 1,8-diPhNaph, differing mainly in the size of the parent structure, one might expect 1,8-diPhAnth to also adopt a parallel displaced configuration or a V-shaped configuration like the one observed by X-ray in Figure 65. Moreover, it cannot adopt a T-shaped configuration, although it is close to the potential line associated with such a configuration. This is due to the inherent geometry of 1,8-diPhAnth, which makes it very difficult for it to adopt a favorable T-shaped conformation.

Based on these results, it is clear that it is too simplistic to attribute the stabilization of 1,8-diPhAnth to  $\pi \cdots \pi$  interactions alone (the distance between the aromatic rings is way too large to justify such a strong energetic effect). Other, as yet unspecified, factors

exert an influence on this stabilization and contribute to the complexity of this molecular behavior.

Table 20, 21 and 22 show the calculated enthalpies of reaction in the gas phase,  $\Delta H^0_{\text{reaction}}(\text{g})$ , at  $T = 298.15 \text{ K}$ , based on the homodesmotic reaction provided at the top of each respective table.

The  $\Delta H^0_{\text{reaction}}(\text{g})$  of the homodesmotic reactions were calculated using the following formula:

$$\Delta H^0_{\text{reaction}}(\text{g}) = \Delta_f H^0_{\text{products}}(\text{g}) - \Delta_f H^0_{\text{reagents}}(\text{g}) \quad \text{Eq. 56}$$

In Tables 20-22, the experimental standard molar enthalpies of reaction in the gas phase,  $\Delta H^0_{\text{reaction}}(\text{g})$ , at  $T = 298.15 \text{ K}$ , for some selected homodesmotic reactions are presented. The values of  $\Delta_f H^0(\text{cr})$  for all the compounds presented in these reaction schemes were determined by combustion calorimetry. In this way, in the calculation of the uncertainties in  $\Delta H^0_{\text{reaction}}(\text{g})$  for all the homodesmotic reactions, some contributions cancel out and can be ignored in this comparative analysis:

- Uncertainties related to the formation of  $\text{CO}_2(\text{g})$  and  $\text{H}_2\text{O}(\text{l})$  in the corresponding combustion reactions cancel out completely.
- Uncertainties related to the calibration of the calorimeters cancel out to a significant extent (depending on the type of calorimeter and calibrant used).

**Table 20.** Experimental and theoretical calculated, M06-2X/6-31+G(d,p) and CCSD(T)/cc-pVDZ, enthalpies of reaction in the gas phase, at  $T = 298.15 \text{ K}$ .

$\Delta H^0_{\text{reaction}}(\text{g}) / \text{kJ}\cdot\text{mol}^{-1}$			
R	Experimental	M062X	CCSD(T)
Phenyl	$-32.4 \pm 5.7$	-15.1	-18.5
4-methoxyphenyl	$-35.9 \pm 6.4$	-14.6	–
4-formylphenyl	–	-10.3	–
Biphen-4-yl	$-36.3 \pm 8.2$	-20.3	–

Both the experimental and computational data in Table 20 show the increased stability when substituents transition from bonding with a naphthalene to bonding with an anthracene in all the 1,8-diarylanthracenes studied. This reaction was designed to quantify the enthalpy associated to lengthening the distance between the two aromatic interacting partners. One of the reasons for this increase in stability is the increased distance between the substituents, which is clearly too short in the naphthalene derivatives.

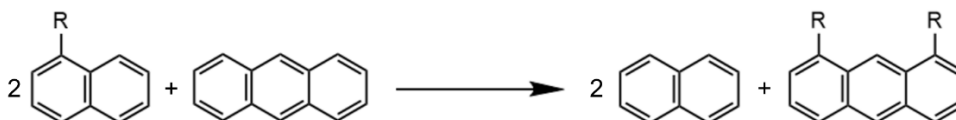
As previously mentioned, the proximity of the substituents in a 1,8-diarylnaphthalene leads to repulsive forces as the predominant factor for the interactions of the substituents. When the distance between substituents is increased, the occurrence of repulsive interactions decreases, while  $\pi \cdots \pi$  interactions become more prominent, increasing the stability of the molecule. Hence, a fraction of this stabilization comes from the alleviation of electronic repulsion by increasing the distance between the interacting rings. However, according to Figure 66, this contribution should be substantially lower than the experimental value of  $\Delta H_{\text{reaction}}^0(\text{g})$ . This difference surmounts to  $\sim 15 \text{ kJ}\cdot\text{mol}^{-1}$ .

In the experimental results, the results for the three substituents exhibit similar values for the homodesmotic reaction in Table 20, higher than  $-30 \text{ kJ}\cdot\text{mol}^{-1}$ . These results suggest the existence of an additional stabilizing factor in all the 1,8-diarylanthracenes studied.

It is worth noting that there is a remarkable discrepancy between the experimental results and the computational results. In particular, the experimental values for  $\Delta H_{\text{reaction}}^0(\text{g})$  show a more negative trend compared to the computational values. Given that M062X is a DFT method based on electron density, it lacks a comprehensive systematic framework to achieve an accurate representation of all electron interactions within a molecule. This characteristic is discussed in the subtopic "Density Functional Theory" under "Quantum Chemistry Calculations" in the broader context of this study. However, the so called gold standard of computational chemistry, CCSD(T), was also not able to adequately describe this system.

This particular feature suggests that the aromatic systems studied may have additional electron interactions not previously considered or that novel intramolecular interactions may be at play. The experimental results suggest the existence of certain unaccounted electronic effects that increase the stability of the molecules that the computational results cannot fully capture or calculate.

**Table 21.** Experimental and theoretical calculated, M06-2X/6-31+G(d,p) and CCSD(T)/cc-pVDZ, enthalpies of reaction in the gas phase, at  $T = 298.15$  K.



R	$\Delta H^{\circ}_{\text{reaction}}(\text{g}) / \text{kJ}\cdot\text{mol}^{-1}$		
	Experimental	M062X	CCSD(T)
Phenyl	$-16.5 \pm 6.1$	-3.6	-6.9
4-methoxyphenyl	$-32.1 \pm 6.6$	-4.4	–
4-formylphenyl	–	-4.4	–
Biphen-4-yl	$-32.3 \pm 8.2$	-13.6	–

Table 21 contains data on the  $\Delta H^{\circ}_{\text{reaction}}(\text{g})$  values obtained from a homodesmotic reaction in which the substituents shift their bonding from a monosubstituted naphthalene to a disubstituted anthracene. This reaction effectively quantifies the interaction involving the two aryl substituents in the anthracenes studied. As can be seen from the results presented in Table 21, this transition leads to an overall improvement in the stability of the molecules involved.

It is important to note that this increased stability represents a different scenario than the results in Table 20. In this case, there are no pronounced repulsive interactions resulting from the proximity of the substituents because the monosubstituted naphthalenes have just one substituent and no other substituents to cause repulsive interactions between them.

In the experimental data, there is a clear difference between the results associated with the phenyl substituent and the other two substituents. In particular, the 4-methoxyphenyl and biphen-4-yl groups exhibit similar  $\Delta H^{\circ}_{\text{reaction}}(\text{g})$  values, while the phenyl group registers a significantly higher (more positive)  $\Delta H^{\circ}_{\text{reaction}}(\text{g})$  value. This discrepancy suggests that the phenyl group contributes relatively less to the overall stability in the context of this homodesmotic reaction compared to the other two substituents. A plausible explanation for this observation could be attributed to the structural differences between these substituents. Both the 4-methoxyphenyl and biphen-4-yl groups have additional functional groups attached to their phenyl group. In the context of this homodesmotic reaction, these additional structural elements lead to an effect that increases the stability of the 1,8-diarylanthracenes. It is conceivable that

these additional components of the substituents enhance the overall aryl-aryl intramolecular interaction. This interaction can include strengthening the  $\pi \cdots \pi$  aromatic interactions and the direct interaction between the R groups, which is an additional aromatic interaction in the case of the biphen-4-yl.

As noted in Table 20, Table 21 also shows a discrepancy between the experimental and computational results. The computational results show less negative  $\Delta H_{\text{reaction}}^{\circ}(\text{g})$  values when contrasted with the experimental results. This recurring pattern highlights the possibility that certain electronic effects contributing to the stability of these aromatic systems have not been accurately captured by the computational method. The computational method gives the expected  $\Delta H_{\text{reaction}}^{\circ}(\text{g})$  if considering only the  $\pi \cdots \pi$  aromatic interactions: interaction enthalpies of  $\sim 5 \text{ kJ}\cdot\text{mol}^{-1}$  for a Ph-Ph distance of about 5 Å. Clearly, the experimental values indicate the presence of an additional stabilizing effect in all the anthracenes studied. The case of R = biphen-4-yl is quite interesting. The more negative  $\Delta H_{\text{reaction}}^{\circ}(\text{g})$  is explained by the existence of a T-shaped aromatic interaction in the “second floor” of phenyl rings. This is nicely observed in the M06-2X/6-31+G(d,p) optimized geometry (shown in Figure 67).

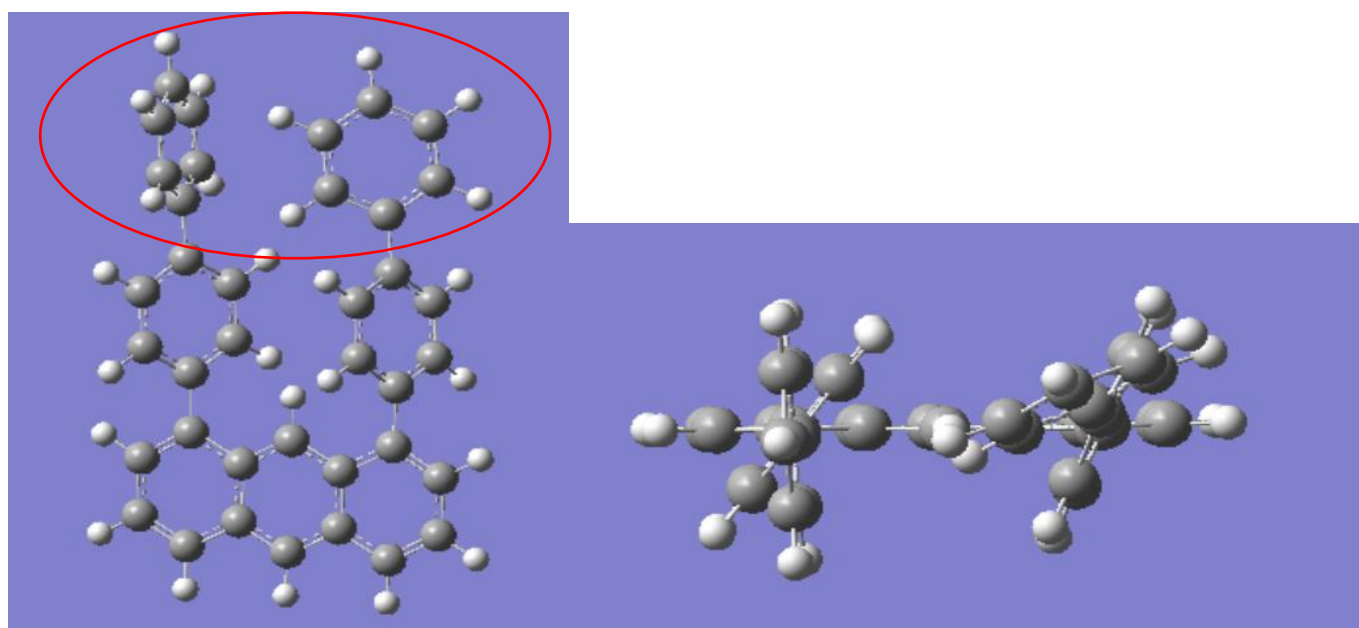
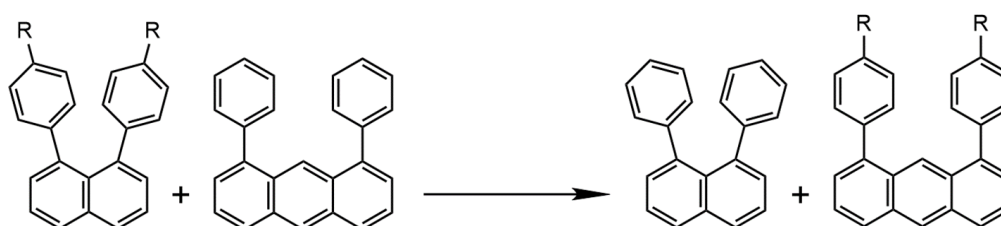


**Figure 67.** M06-2X/6-31+G(d,p) optimized geometry of 1,8-dibiPhAnth.

Such a “second floor” T-shaped interaction was also observed in 1,8-diPhNaph [41]. The magnitude of this interaction can be estimated by the difference in  $\Delta H^0_{\text{reaction}}(\text{g})$  between R = biphen-4-yl and R = phenyl as:  $\Delta H(\pi\cdots\pi, \text{second floor}) \approx (-32.3) - (-16.5) = -(15.8 \pm 10) \text{ kJ}\cdot\text{mol}^{-1}$ , which is a typical value of T-shaped benzene-benzene interactions.

In the computational results, the calculations for phenyl, 4-methoxyphenyl and 4-formylphenyl groups provide values of  $\Delta H^0_{\text{reaction}}(\text{g})$  that agree relatively well with each other. This is consistent with the behavior of the experimental results. In the case of biphen-4-yl, its computational result of  $\Delta H^0_{\text{reaction}}(\text{g})$  is relatively more negative than the other three, which shows that the computational method detects the additional  $\pi\cdots\pi$  interactions coming from the second phenyl group in the biphenyl structure.

**Table 22.** Experimental and theoretical calculated, M06-2X/6-31+G(d,p) and CCSD(T)/cc-pVDZ, enthalpies of reaction in the gas phase, at  $T = 298.15 \text{ K}$ .



R	$\Delta H^0_{\text{reaction}}(\text{g}) / \text{kJ}\cdot\text{mol}^{-1}$	
	Experimental	M062X
<b>4-methoxy</b>	$-3.5 \pm 7.2$	0.6
<b>4-formyl</b>	–	4.9
<b>Phenyl</b>	$-3.9 \pm 8.9$	-5.7

Table 22 contains the  $\Delta H^0_{\text{reaction}}(\text{g})$  values for a homodesmotic reaction where a 1,8-diarylnaphthalene trades its substituents with 1,8-diPhAnth, resulting in 1,8-diPhNaph and a 1,8-diarylanthracene. This homodesmotic reaction is significantly different from the previous two presented.

The experimental results, show less negative  $\Delta H^0_{\text{reaction}}(\text{g})$  values, approaching almost  $0 \text{ kJ}\cdot\text{mol}^{-1}$ , compared to the values in the previous two tables (Tables 20 and 21). In this particular scenario, these reactions are almost athermic, which suggests that there is an absence of significant effects that differentiate the reactants from the products. In

respect to energetics, the influence of the methoxy and phenyl groups in 1,8-diarylanthracenes and 1,8-diarylnaphthalenes is similar.

As repeatedly emphasized in the analysis of the results in Figure 66 and Tables 20 and 21, there is a discernible electronic effect that eludes detection by the computational approach but is evident in the experimental results. The reason this effect cannot be detected by the computational method is due to the possibility that it is not an aromatic interaction with dispersive properties, which is the primary focus of the computational method's detection capabilities. This electronic effect occurs consistently in all 1,8-diarylanthracenes, the only variation being the degree of stability it confers on the molecule.

Neeraj Agarwal *et al.* have noted that while substitutions at the 9,10-positions of anthracene have been extensively documented in the scientific literature, exploration of substitutions at alternative positions within the anthracene molecule remains comparatively limited [47]. As a result, the electronic effects mentioned earlier have not been thoroughly investigated. They have also indicated that 1,8-diarylanthracenes exhibit higher oxidation resistance compared to their 9,10-diarylanthracene counterparts [47]. This observation suggests that not only do additional  $\pi \cdots \pi$  interactions contribute to the stabilization of these molecules, but that there is also an intramolecular effect at play that ensures the structural integrity of the molecule.

In a related study, Herbert House *et al.* tested the reactivity of C-9 in 1,8-diarylanthracenes using various reactions, among them halogenation and acetylation reactions. However, they were unable to isolate a 9-halo derivative and the acetylation reaction resulted in the formation of a mixture of monoacetyl derivatives [84]. This indicates that the atom C-9 in a 1,8-diarylanthracene is relatively unreactive.

Furthermore, the same authors made a surprising discovery that showed that the two phenyl rings of 10-bromo-1,8-diphenylanthracene (Figure 68) were not approximately parallel to one another, as shown in Figure 65 [84].

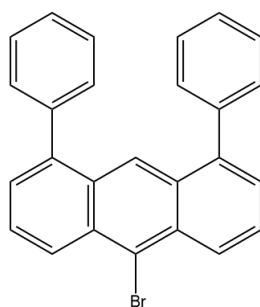


**Figure 68.** Visual representation of 10-bromo-1,8-diphenylanthracene.

Since the structure of 10-bromo-1,8-diphenylanthracene is similar to the structure of 1,8-diPhAnth, with the exception of the atom Br bonded to the atom C-10, it is safe to suggest that the behaviour exhibited by the two phenyl rings would be the same in 1,8-diPhAnth. This was confirmed by the X-ray structures shown in Figures 56 and 57. This discovery goes along with the affirmation made in Figure 66, where it was written that 1,8-diPhAnth can't have a T-shaped configuration. At least in the crystal phase, it also doesn't adopt the parallel displaced configuration.

In another study of Herbert House with his colleagues, mononitrations of 1,8-diPhAnth were made in hopes to synthesize a 9-nitro derivative of 1,8-diPhAnth. The mononitration led to a 10-nitro derivative of 1,8-diPhAnth and further nitration led to substitution at C-4 in the anthracene ring [85]. They concluded that there appears to be a steric hindrance to electrophilic substitution at C-9 in 1,8-diPhAnth [85].

A comparison of the NMR spectra, obtained in this work, was made in order to better understand the behaviour of the hydrogen atoms bonded to C-9 and C-10 of 1,8-diarylanthracenes molecules (shown in Figure 69).

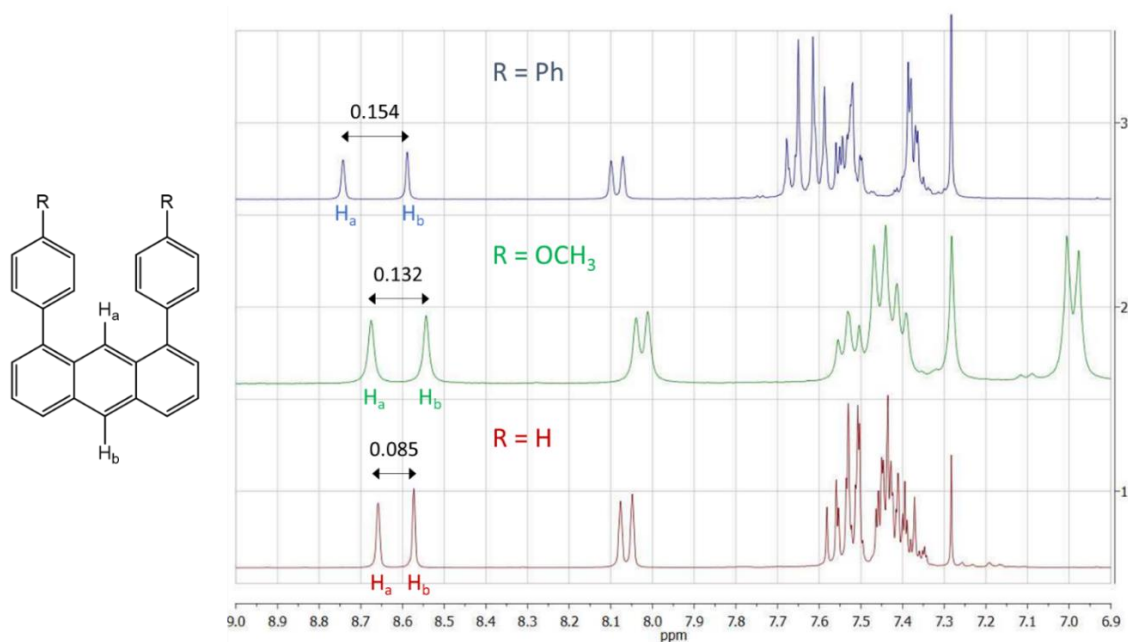


**Figure 69.** Left) 1,8-diarylanthracene; Right)  $^1H$  NMR spectra of 1,8-dibiPhAnth, 1,8-bismethoxyPhAnth and 1,8-diPhAnth. The spectra, recorded in  $CDCl_3$  at  $T = 298$  K, show the differences between the chemical shifts of the two protons in ppm.

From observing the spectrum of each molecule and comparing the peaks of  $H_a$  and  $H_b$ , it is noticeable that while the  $H_b$  peak is relatively insensitive, the  $H_a$  peak ( $H_a$  is bonded to C-9) of 1,8-diPhAnth suffers a downfield shift quite dependent on the substituent. Neeraj Agarwal *et al.* detected a similar behaviour. They observed that the proton bonded to C-9 of a 1,8-disubstituted anthracene is downfield shifted as compared to unsubstituted anthracene and they concluded that this may be because of the presence of an electron withdrawing nature of an aryl group in the neighborhood [47].

Considering that a downfield shift can occur when the electron density around an atom decreases, it is reasonable to assume that there is a factor that decreases the electron density around  $H_a$ . Although this downfield shift is not necessarily due to the electron-withdrawing nature of an aryl group in the vicinity, as Neeraj Agarwal and his colleagues suggest, it is obvious that some influencing factor is contributing to this downfield shift.

It is noteworthy that in Figure 69, the downfield shift occurs when the substituent moves from the simplest  $-H$  group to the more complicated 4-methoxy and 4-phenyl groups. Similarly, the downfield shift observed by Neeraj Agarwal *et al.* occurred when an unsubstituted anthracene was substituted [47]. Particularly, the authors found that electron-donating groups lead to downfield shifts and electron-withdrawing groups to

upfield shifts, of H-9 relative to H-10. This suggests that the introduction of substituents into anthracene along with the subsequent increase in their complexity may underlie this phenomenon. If this hypothesis is correct, interactions between the substituents and H<sub>a</sub> could occur, leading to a reduction of the electron density in the proton.

With all findings obtained in this subtopic, a theory can be made. There is evidence, not only obtained in this work but also in literature, that in 1,8-diarylanthracenes there is an electronic effect involving the substituents and the hydrogen atom bonded to C-9, that doesn't exist in 9,10-diarylanthracenes nor in 1,8-diarylnaphthalenes. There is still no comprehensive explanation to what this effect exactly is or does, but the findings show that this effect increases the stability, the integrity of the molecular structure and may contribute for making oxidations and other reactions difficult to occur [41,47,83,84,85].

Figure 70 shows a possible visual representation of the electronic effect present in 1,8-diarylanthracenes.

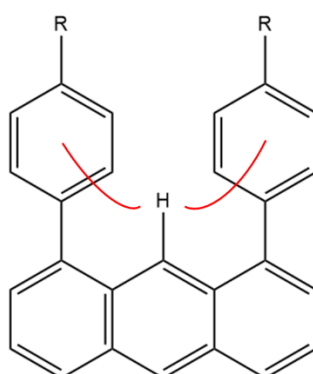


**Figure 70.** Visual representation of the possible electronic effect between two substituents and the hydrogen atom bonded to C-9, in 1,8-diarylanthracene.

## Optical Properties

The UV-Vis spectroscopy spectra for the compounds studied are shown in Figures 71 to 75. These spectra serve as a basis for comparative analysis and allow observation of changes in molar absorptivity when variations in size and substituents are introduced. In addition, the spectrum of 9,10-diPhAnth is shown alongside the spectrum of 1,8-diPhAnth for comparative evaluation.

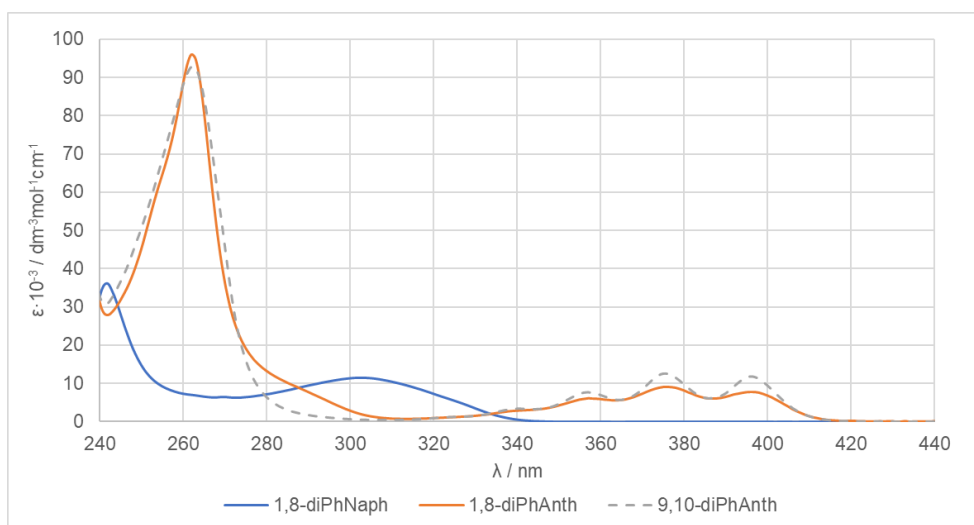


**Figure 71.** Plot of UV-Vis spectra, in  $\text{CH}_2\text{Cl}_2$  at  $T = 298.1 \text{ K}$ , comparing 1,8-diPhNaph, 1,8-diPhAnth and 9,10-diPhAnth analogs. The small hump centered at  $\sim 290 \text{ nm}$  is a prominent feature of 1,8-diPhAnth.

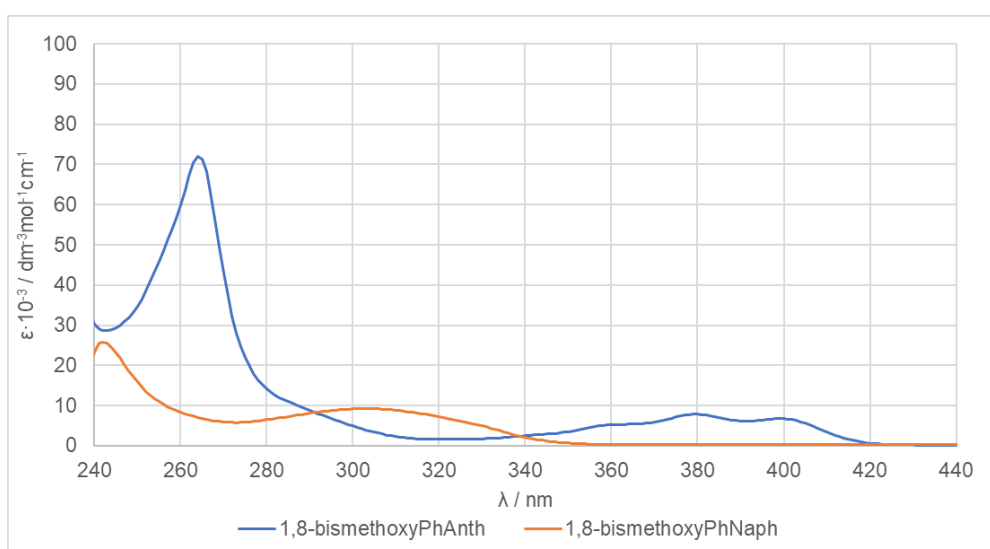


**Figure 72.** Plot of UV-Vis spectra, in  $\text{CH}_2\text{Cl}_2$  at  $T = 298.1 \text{ K}$ , comparing 1,8-bismethoxyPhNaph and 1,8-bismethoxyPhAnth analogs.

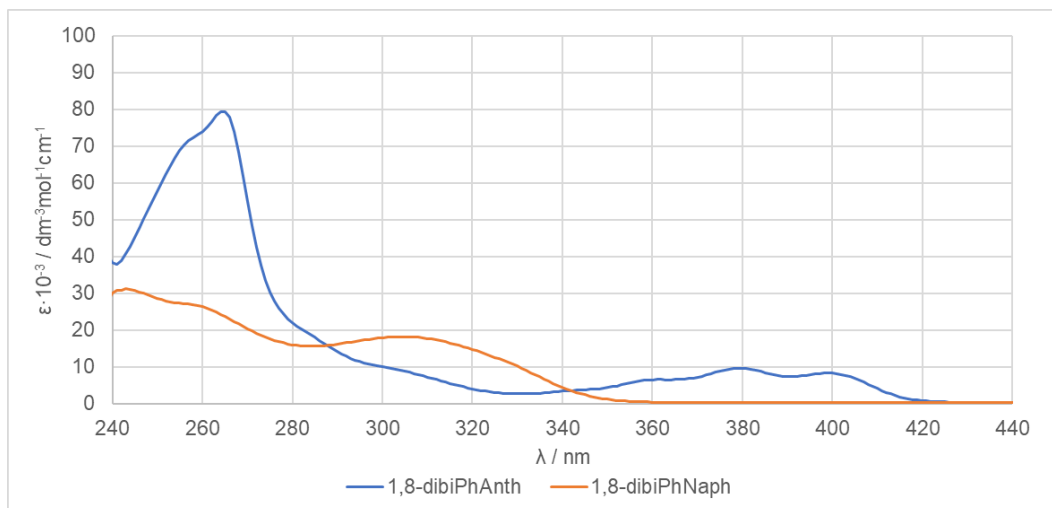


**Figure 73.** Plot of UV-Vis spectra, in  $\text{CH}_2\text{Cl}_2$  at  $T = 298.1 \text{ K}$ , comparing 1,8-dibiPhNaph and 1,8-dibiPhAnth analogs.

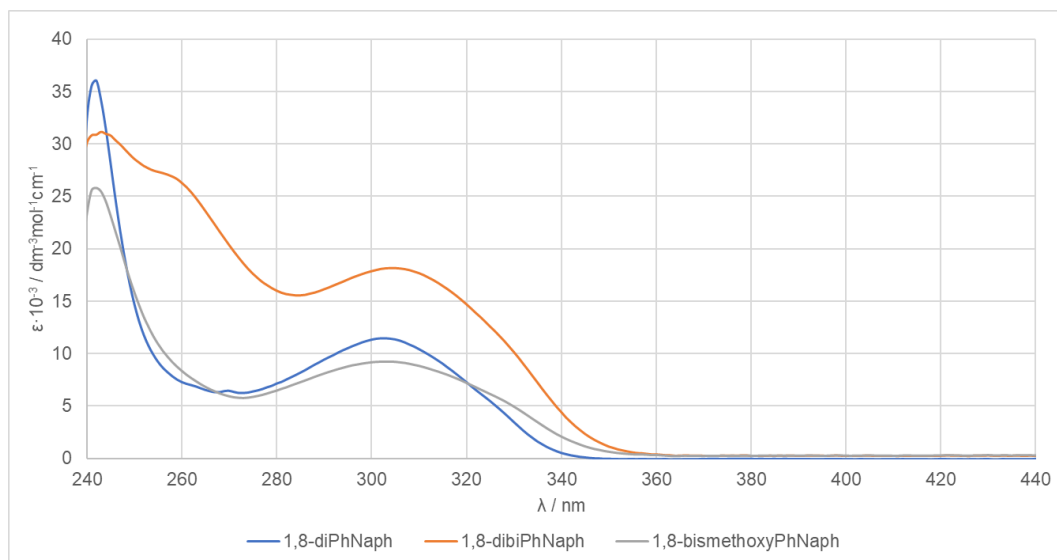


**Figure 74.** Plot of UV-Vis spectra, in  $\text{CH}_2\text{Cl}_2$  at  $T = 298.1 \text{ K}$ , comparing the three 1,8-diarylnaphthalene studied.

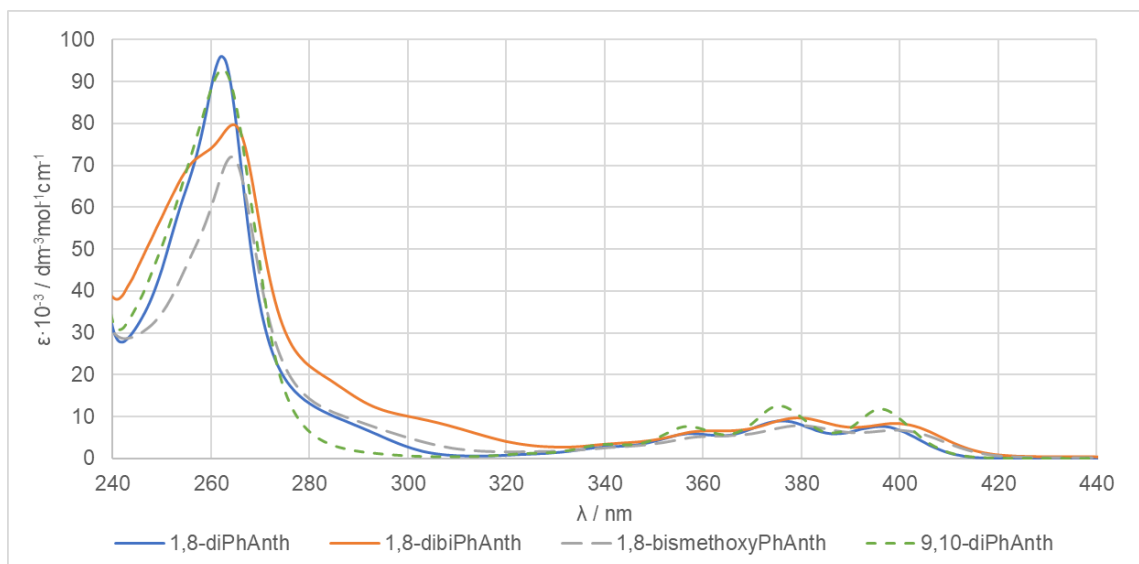


**Figure 75.** Plot of UV-Vis spectra, in  $\text{CH}_2\text{Cl}_2$  at  $T = 298.1 \text{ K}$ , comparing the three 1,8-diarylanthracenes studied and 9,10-diPhAnth.

In Figures 71-75, the comparison between 1,8-diarylnaphthalenes and their counterparts, 1,8-diarylanthracenes, is made. The first peak in each spectrum include electronic transitions between molecular orbitals mainly located in the aryl substituents and the following band corresponds to the molecular orbitals of the parent structure (naphthalene or anthracene). It is noticeable that 1,8-diarylanthracenes suffer a bathochromic shift and their peaks exhibit a higher molar absorptivity compared to their 1,8-diarylnaphthalene counterparts.

Figure 71 shows that the spectra of 9,10-diPhAnth is virtually superimposed with the corresponding 1,8-diPhAnth, indicating that the phenyl-acene conjugation is weak in both compounds. This supports that phenyl-acene conjugation is not energetically significant and is a negligible contribution to  $\Delta H^{\circ}_{\text{reaction}}(\text{g})$  of the homodesmotic reaction presented in “Molecular Energetics” subtopic. There is a striking feature that distinguishes the spectra of all the 1,8-diarylanthracenes, which is the small hump to the right (slightly bathochromically shifted) of the peak of highest intensity (290 nm, observable in Figures 71, 72, 73 and 75). This hump is not observable in the spectra of 1,8-diarylnaphthalenes and 9,10-diPhAnth and its location in the spectra suggests that it is related to transitions involving the aryl substituents.

## Conclusion

In this dissertation, comprehensive research of various aromatic systems was carried out. The investigation included the comprehensive evaluation of thermodynamic properties, including sublimation, fusion, optical properties, and molecular energetics, for a variety of 1,8-diarylanthracenes.

It was previously mentioned that increasing the separation distance between π···π interactions within the studied aromatic systems up to a certain threshold leads to an improvement in stability. This increased distance serves to weaken the repulsive forces between substituents, facilitating stronger interactions. In addition, the choice of substituents has been shown to be an influential determinant of stability.

In particular, the thermodynamic properties of fusion for the compound 1,8-diPhAnth were carefully investigated in this study. The results showed the presence of at least three polymorphs for 1,8-diPhAnth. While the existing literature acknowledges the existence of two polymorphs, the identification of this third polymorph represents a new contribution to the knowledge of these systems.

Regarding the thermodynamic properties of sublimation, a notable observation is the crystal packing of 1,8-diPhAnth, which exhibits relatively low packing efficiency compared to the other compounds.

In contrast, the other 1,8-diarylanthracenes exhibit commendable stability of their crystal packing. Moreover, their incremental changes in enthalpy and entropy closely mirror those observed in their 1,8-diarylnaphthalene counterparts. This consistency suggests that the behavior of their substituents remains predictable and uniform even when the parent molecular structure is altered.

Regarding molecular energetics, the results obtained were interesting. First it was found through Figure 66 that 1,8-diPhAnth doesn't exhibit a parallel displaced configuration, and it was later found in Figure 65 that it can exhibit a somewhat V-shaped configuration. On the subject of homodesmotic reaction, overall the experimental and computational results of  $\Delta H^0_{\text{reaction}}(\text{g})$  showed that there was an increase in stability associated with increasing the distance between the two aryl substituents from 1,8-diarylnaphthalenes to 1,8-diarylanthracenes. The computational results were overall more positive than the experimental ones, indicating that in the molecules there is an additional interaction that is not explained by dispersive forces alone.

According to the findings, the detected energy effect in the 1,8-diarylanthracenes studied:

- Involves the two aryl substituents and H-9.
- Leads to a significant energetic stabilization of about 15-20 kJ·mol<sup>-1</sup>.
- Is ill-described by M06-2X and CCSD(T) computational methods, thus suggesting that the origin of this effect is not related to aromatic interactions nor dispersive interactions (which is well described by the levels of theory used).
- Can contribute to explaining the low reactivity of the C-9 carbon.
- Can be related with a significant shift of the <sup>1</sup>H NMR signal of H-9 (downfield shift relative to H-10 in the three anthracenes studied).
- Can be related to the occurrence of a shoulder in the UV-Vis spectra, bathochromically shifted relative to the main UV-band.
- Can be related to a marked tendency, at least in the crystal phase of 1,8-diarylanthracenes, to adopt a V-shaped conformation.

Based on the observation it was proposed that the origin of this stabilization is the existence of some type of aryl $\cdots$ H $\cdots$ aryl electron delocalization, in which the H acts like an electron bridge between the substituents. This phenomenon is consistent with a stabilization of  $\sim 15$  kJ·mol<sup>-1</sup>, and would lead to a small bathochromic shift of UV-Vis peaks associated to molecular orbitals with a high contribution from the aryl substituents. The “transit” of electrons would significantly affect the <sup>1</sup>H NMR chemical shift of H-9. Being a phenomenon of electron delocalization would involve a good fraction of static electron correlation which is ill-described by M06-2X and CCSD(T). The breaking of this conjugation would contribute to the low reactivity of C-9. The V-shaped geometry in crystal 1,8-diarylanthracenes can simply be the result of crystal packing forces. However, one cannot discard that, instead, it is the conformation that, for some reason, maximizes this aryl $\cdots$ H $\cdots$ aryl interaction.

Although the exact source of this stabilization remains uncertain, this work has successfully identified and measured it. Furthermore, a link has been established between this phenomenon and observable physicochemical phenomena.



## Future Perspectives

In the future, the synthesis of 4,4'-Anth-1,8-diBenzAl needs to be redone, so that it can be analyzed, which will be important to progress further in this study. The determination of molecular energetics in this compound is particularly important to address the effect of electron-withdrawing group on the interaction between the two aryl rings.

The phase behaviour needs to be studied using DSC for all 1,8-diarylanthracenes.

The computational calculations for CCSD(T)/cc-pVDZ and CI for all molecules are already ongoing and only time is needed to acquire the results.

The study of 1,5-diphenylanthracene is currently underway. This compound will serve as a test to our hypothesis that the increase in stabilization in 1,8-diarylanthracenes is related to the adjacent position of the two phenyl rings.

The search for more types of 1,8-diarylanthracenes, for the enrichment of this study, is still ongoing. Another type of compounds that will be delved in the future is the 1,8-diarylbiphenylenes. These compounds exhibit higher distance between substituents than 1,8-diarylnaphthalenes but lower distance than 1,8-diarylanthracenes. The study of these aromatic systems might bring more enlightenment on the topic of  $\pi\cdots\pi$  interactions. Another type of compounds that might be studied are 1,10-diaryltetracenes. Their increased distance between substituents and additional H atoms in the core may bring to light interesting effects that may help in describing better the detected energy effect.

Research is currently being conducted on 1,8-diarylnaphthalenes, where aryl = naphthalene, and there are plans for future investigation of 1,8-dinaphthaleneanthracenes compounds, to better understand the effect of molecular size on these aromatic systems.



## Bibliography

- [1] Lima, C. F., Rocha, M. A., Gomes, L. R., Low, J. N., Silva, A. M., & Santos, L. M. (2012). Experimental support for the role of dispersion forces in aromatic interactions. *Chemistry—A European Journal*, 18(29), 8934-8943.
- [2] Cyranski, M. K., Krygowski, T. M., Katritzky, A. R., & Schleyer, P. V. R. (2002). To what extent can aromaticity be defined uniquely?. *The Journal of Organic Chemistry*, 67(4), 1333-1338.
- [3] Krygowski, T. M., Ejsmont, K., Stepień, B. T., Cyrański, M. K., Poater, J., & Sola, M. (2004). Relation between the substituent effect and aromaticity. *The Journal of Organic Chemistry*, 69(20), 6634-6640.
- [4] Hunter, C. A., Lawson, K. R., Perkins, J., & Urch, C. J. (2001). Aromatic interactions. *Journal of the Chemical Society, Perkin Transactions 2*, (5), 651-669.
- [5] Cozzi, F., Cinquini, M., Annunziata, R., Dwyer, T., & Siegel, J. S. (1992). Polar/π interactions between stacked aryls in 1, 8-diarylnaphthalenes. *Journal of the American Chemical Society*, 114(14), 5729-5733.
- [6] Wheeler, S. E. (2013). Understanding substituent effects in noncovalent interactions involving aromatic rings. *Accounts of chemical research*, 46(4), 1029-1038.
- [7] Janda, K. C., Hemminger, J. C., Winn, J. S., Novick, S. E., Harris, S. J., & Klemperer, W. (1975). Benzene dimer: a polar molecule. *The Journal of Chemical Physics*, 63(4), 1419-1421.
- [8] Steed, J. M., Dixon, T. A., & Klemperer, W. (1979). Molecular beam studies of benzene dimer, hexafluorobenzene dimer, and benzene–hexafluorobenzene. *The Journal of Chemical Physics*, 70(11), 4940-4946.
- [9] Young, L., Haynam, C. A., & Levy, D. H. (1983). The photophysics and photochemistry of weakly bound dimers of s-tetrazine. *The Journal of chemical physics*, 79(4), 1592-1604.
- [10] Gervasio, F. L., Procacci, P., Cardini, G., Guarna, A., Giolitti, A., & Schettino, V. (2000). Interaction between Aromatic Residues. Molecular Dynamics and ab Initio Exploration of the Potential Energy Surface of the Tryptophan– Histidine Pair. *The Journal of Physical Chemistry B*, 104(5), 1108-1114.

- [11] Sinnokrot, M. O., & Sherrill, C. D. (2004). Highly accurate coupled cluster potential energy curves for the benzene dimer: sandwich, T-shaped, and parallel-displaced configurations. *The Journal of Physical Chemistry A*, 108(46), 10200-10207.
- [12] Fu, C. F., & Tian, S. X. (2011). A comparative study for molecular dynamics simulations of liquid benzene. *Journal of chemical theory and computation*, 7(7), 2240-2252.
- [13] Headen, T. F., Howard, C. A., Skipper, N. T., Wilkinson, M. A., Bowron, D. T., & Soper, A. K. (2010). Structure of π- π Interactions in Aromatic Liquids. *Journal of the American Chemical Society*, 132(16), 5735-5742.
- [14] Tsuzuki, S., Honda, K., Uchimaru, T., Mikami, M., & Tanabe, K. (2002). Origin of attraction and directionality of the π/π interaction: model chemistry calculations of benzene dimer interaction. *Journal of the American Chemical Society*, 124(1), 104-112.
- [15] Sherrill, C. D., Takatani, T., & Hohenstein, E. G. (2009). An assessment of theoretical methods for nonbonded interactions: Comparison to complete basis set limit coupled-cluster potential energy curves for the benzene dimer, the methane dimer, benzene- methane, and benzene- H<sub>2</sub>S. *The Journal of Physical Chemistry A*, 113(38), 10146-10159.
- [16] Patrick, C. R., & Prosser, G. S. (1960). A molecular complex of benzene and hexafluorobenzene. *Nature*, 187(4742), 1021-1021.
- [17] Dahl, T. (1975). Crystal Structure of the 1: 1 Addition Compound between p-Xylene and Hexafluorobenzene. *Acta Chem Scand A*, 29, 170-174.
- [18] Tillack, A. F., & Robinson, B. H. (2017). Simple model for the benzene hexafluorobenzene interaction. *The Journal of Physical Chemistry B*, 121(25), 6184-6188.
- [19] Desiraju, G. R., & Gavezzotti, A. (1989). From molecular to crystal structure; polynuclear aromatic hydrocarbons. *Journal of the Chemical Society, Chemical Communications*, (10), 621-623.
- [20] Guckian, K. M., Schweitzer, B. A., Ren, R. X. F., Sheils, C. J., Tahmassebi, D. C., & Kool, E. T. (2000). Factors contributing to aromatic stacking in water: evaluation in the context of DNA. *Journal of the American Chemical Society*, 122(10), 2213-2222.
- [21] Petersheim, M., & Turner, D. H. (1983). Base-stacking and base-pairing contributions to helix stability: thermodynamics of double-helix formation with CCGG,

CCGGp, CCGGAp, ACCGGp, CCGGUp, and ACCGGUp. *Biochemistry*, 22(2), 256-263.

[22] Rotello, V. M., Viani, E. A., Deslongchamps, G., Murray, B. A., & Rebek Jr, J. (1993). Molecular recognition in water: New receptors for adenine derivatives. *Journal of the American Chemical Society*, 115(2), 797-798.

[23] Petti, M. A., Shepodd, T. J., Barrans, R. E., & Dougherty, D. A. (1988). "Hydrophobic" binding of water-soluble guests by high-symmetry, chiral hosts. An electron-rich receptor site with a general affinity for quaternary ammonium compounds and electron-deficient. pi. systems. *Journal of the American Chemical Society*, 110(20), 6825-6840.

[24] Cozzi, F., Cinquini, M., Annuziata, R., & Siegel, J. S. (1993). Dominance of polar/pi. over charge-transfer effects in stacked phenyl interactions. *Journal of the American Chemical Society*, 115(12), 5330-5331.

[25] Zhang, X., Zhao, K., & Gu, Z. (2022). Transition Metal-Catalyzed Biaryl Atropisomer Synthesis via a Torsional Strain Promoted Ring-Opening Reaction. *Accounts of Chemical Research*, 55(12), 1620-1633.

[26] Rickhaus, M., Mayor, M., & Juríček, M. (2016). Strain-induced helical chirality in polyaromatic systems. *Chemical Society Reviews*, 45(6), 1542-1556.

[27] Shchavlev, A. E., Pankratov, A. N., & Enchev, V. (2007). Intramolecular hydrogen-bonding interactions in 2-nitrosophenol and nitrosonaphthols: Ab initio, density functional, and nuclear magnetic resonance theoretical study. *The Journal of Physical Chemistry A*, 111(30), 7112-7123.

[28] Novoa, J. J., & Mota, F. (2000). The C–H··· π bonds: strength, identification, and hydrogen-bonded nature: a theoretical study. *Chemical Physics Letters*, 318(4-5), 345-354.

[29] Steiner, T., Starikov, E. B., Amado, A. M., & Teixeira-Dias, J. J. (1995). Weak hydrogen bonding. Part 2. The hydrogen bonding nature of short C–H··· π contacts: crystallographic, spectroscopic and quantum mechanical studies of some terminal alkynes. *Journal of the Chemical Society, Perkin Transactions 2*, (7), 1321-1326.

[30] Madhavi, N. L., Desiraju, G. R., Katz, A. K., Carrell, H. L., & Nangia, A. (1997). Evidence for the characterisation of the C–H··· π interaction as a weak hydrogen bond: toluene and chlorobenzene solvates of 2, 3, 7, 8-tetraphenyl-1, 9, 10-anthridine. *Chemical Communications*, (20), 1953-1954.

- [31] Arunan, E., & Gutowsky, H. S. (1993). The rotational spectrum, structure and dynamics of a benzene dimer. *The Journal of chemical physics*, 98(5), 4294-4296.
- [32] Reeves, L. W., & Schneider, W. G. (1957). Nuclear magnetic resonance measurements of complexes of chloroform with aromatic molecules and olefins. *Canadian Journal of Chemistry*, 35(3), 251-261.
- [33] Hobza, P., Selzle, H. L., & Schlag, E. W. (1996). Potential energy surface for the benzene dimer. Results of ab initio CCSD (T) calculations show two nearly isoenergetic structures: T-shaped and parallel-displaced. *The Journal of Physical Chemistry*, 100(48), 18790-18794.
- [34] Hansen, P. E., Bolvig, S., & Wozniak, K. (2005). Steric compression and twist in o-hydroxy acyl aromatics with intramolecular hydrogen bonding. *Journal of molecular structure*, 749(1-3), 155-168.
- [35] Gilli, P., Bertolasi, V., Pretto, L., Ferretti, V., & Gilli, G. (2004). Covalent versus electrostatic nature of the strong hydrogen bond: discrimination among single, double, and asymmetric single-well hydrogen bonds by variable-temperature X-ray crystallographic methods in  $\beta$ -diketone enol RAHB systems. *Journal of the American Chemical Society*, 126(12), 3845-3855.
- [36] Abildgaard, J., Bolvig, S., & Hansen, P. E. (1998). Unraveling the electronic and vibrational contributions to deuterium isotope effects on  $^{13}\text{C}$  chemical shifts using ab initio model calculations. Analysis of the observed isotope effects on sterically perturbed intramolecular hydrogen-bonded o-hydroxy acyl aromatics. *Journal of the American Chemical Society*, 120(35), 9063-9069.
- [37] Tanimoto, Y., Kobayashi, H., Nagakura, S., & Saito, Y. (1973). The crystal structure of acetophenone at 154 K. *Acta Crystallographica Section B: Structural Crystallography and Crystal Chemistry*, 29(9), 1822-1826.
- [38] Raissi, H., Yoosefian, M., Mollania, F., & Khoshkhou, S. (2013). Electronic structures, intramolecular interactions, and aromaticity of substituted 1-(2-iminoethylidene) silan amine: a density functional study. *Structural Chemistry*, 24, 123-137.
- [39] Suresh, C. H., & Koga, N. (2002). Accurate calculation of aromaticity of benzene and antiaromaticity of cyclobutadiene: new homodesmotic reactions. *The Journal of Organic Chemistry*, 67(6), 1965-1968.

- [40] Bock, C. W., Trachtman, M., & George, P. (1990). A molecular orbital study comparing the effects of heteroatom substitution in trans-1, 3-butadiene, all-trans-1, 3, 5-hexatriene, and benzene. *Structural Chemistry*, 1, 345-354.
- [41] Lima, C. F., Rocha, M. A., Schröder, B., Gomes, L. R., Low, J. N., & Santos, L. M. (2012). Phenyl naphthalenes: sublimation equilibrium, conjugation, and aromatic interactions. *The Journal of Physical Chemistry B*, 116(11), 3557-3570.
- [42] Martinez, C. R., & Iverson, B. L. (2012). Rethinking the term "pi-stacking". *Chemical Science*, 3(7), 2191-2201.
- [43] Hunter, C. A., & Sanders, J. K. (1990). The nature of pi-π interactions. *Journal of the American Chemical Society*, 112(14), 5525-5534.
- [44] Kais, S. (2007). Entanglement, electron correlation, and density matrices. *Advances in Chemical Physics*, 134, 493.
- [45] Ramos-Cordoba, E., Salvador, P., & Matito, E. (2016). Separation of dynamic and nondynamic correlation. *Physical Chemistry Chemical Physics*, 18(34), 24015-24023.
- [46] Mok, D. K., Neumann, R., & Handy, N. C. (1996). Dynamical and nondynamical correlation. *The Journal of Physical Chemistry*, 100(15), 6225-6230.
- [47] Agarwal, N., Patil, M., & Patil, M. (2015). Synthesis of highly emissive 1, 8-diaryl anthracene derivatives and fabrication of their micro/nanostructures. *RSC advances*, 5(119), 98447-98455.
- [48] Kusukawa, T., Kojima, Y., & Kannen, F. (2019). Mechanofluorochromic properties of 1, 8-diphenylanthracene derivatives. *Chemistry Letters*, 48(10), 1213-1216.
- [49] Maluenda, I., & Navarro, O. (2015). Recent developments in the Suzuki-Miyaura reaction: 2010–2014. *Molecules*, 20(5), 7528-7557.
- [50] Carrow, B. P., & Hartwig, J. F. (2011). Distinguishing between pathways for transmetalation in Suzuki–Miyaura reactions. *Journal of the American Chemical Society*, 133(7), 2116-2119.
- [51] Suzuki, A. (2002). Cross-coupling reactions via organoboranes. *Journal of organometallic chemistry*, 653(1-2), 83-90.
- [52] Bartle, K. D., & Myers, P. (2002). History of gas chromatography. *TrAC Trends in Analytical Chemistry*, 21(9-10), 547-557.

- [53] Dutta, A. (2017). Fourier transform infrared spectroscopy. *Spectroscopic methods for nanomaterials characterization*, 73-93.
- [54] Van de Voort, F. R. (1992). Fourier transform infrared spectroscopy applied to food analysis. *Food Research International*, 25(5), 397-403.
- [55] Jaggi, N., & Vij, D. R. (2006). Fourier transform infrared spectroscopy. In *Handbook of Applied Solid State Spectroscopy* (pp. 411-450). Boston, MA: Springer US.
- [56] Picollo, M., Aceto, M., & Vitorino, T. (2018). UV-Vis spectroscopy. *Physical sciences reviews*, 4(4), 20180008.
- [57] Mäntele, W., & Deniz, E. (2017). UV–VIS absorption spectroscopy: Lambert-Beer reloaded. *Spectrochimica Acta Part A: Molecular and Biomolecular Spectroscopy*, 173, 965-968.
- [58] Gill, P., Moghadam, T. T., & Ranjbar, B. (2010). Differential scanning calorimetry techniques: applications in biology and nanoscience. *Journal of biomolecular techniques: JBT*, 21(4), 167.
- [59] (2003). Diamond Differential Scanning Calorimeter (DSC). *Diamond Differential Scanning Calorimeter (DSC) - Brochure*. <https://web.itu.edu.tr/~yusuf/labs/DSC.pdf>.
- [60] Santos, L. M., Lima, L. M. S. S., Lima, C. F., Magalhães, F. D., Torres, M. C., Schröder, B., & da Silva, M. A. R. (2011). New Knudsen effusion apparatus with simultaneous gravimetric and quartz crystal microbalance mass loss detection. *The Journal of Chemical Thermodynamics*, 43(6), 834-843.
- [61] da Silva, M. A. R., Pilcher, G., Santos, L. M., & Lima, L. M. S. S. (2007). Calibration and test of an aneroid mini-bomb combustion calorimeter. *The Journal of Chemical Thermodynamics*, 39(5), 689-697.
- [62] Hubbard, W. N., Scott, D. W., & Waddington, G. (1956). Standard states and corrections for combustions in a bomb at constant volume. *Experimental thermochemistry*, 1, 75-128.
- [63] Chachiyo, T., & Chachiyo, H. (2020). Understanding electron correlation energy through density functional theory. *Computational and Theoretical Chemistry*, 1172, 112669.
- [64] Cremer, D. (2001). Density functional theory: coverage of dynamic and non-dynamic electron correlation effects. *Molecular Physics*, 99(23), 1899-1940.

- [65] Stanton, J. F. (1997). Why CCSD (T) works: a different perspective. *Chemical Physics Letters*, 281(1-3), 130-134.
- [66] Harding, M. E., Metzroth, T., Gauss, J., & Auer, A. A. (2008). Parallel calculation of CCSD and CCSD (T) analytic first and second derivatives. *Journal of Chemical Theory and Computation*, 4(1), 64-74.
- [67] Rezac, J., Simova, L., & Hobza, P. (2013). CCSD [T] describes noncovalent interactions better than the CCSD (T), CCSD (TQ), and CCSDT methods. *Journal of chemical theory and computation*, 9(1), 364-369.
- [68] Bartlett, R. J., & Musiał, M. (2007). Coupled-cluster theory in quantum chemistry. *Reviews of Modern Physics*, 79(1), 291.
- [69] Nesbet, R. K. (1955). Configuration interaction in orbital theories. *Proceedings of the Royal Society of London. Series A. Mathematical and Physical Sciences*, 230(1182), 312-321.
- [70] Cremer, D. (2013). From configuration interaction to coupled cluster theory: The quadratic configuration interaction approach. *Wiley Interdisciplinary Reviews: Computational Molecular Science*, 3(5), 482-503.
- [71] Häser, M. (1993). Møller-Plesset (MP2) perturbation theory for large molecules. *Theoretica chimica acta*, 87, 147-173.
- [72] Tsuchimochi, T., & Van Voorhis, T. (2014). Extended Møller-Plesset perturbation theory for dynamical and static correlations. *The Journal of Chemical Physics*, 141(16).
- [73] Häser, M., Almlöf, J., & Scuseria, G. E. (1991). The equilibrium geometry of C60 as predicted by second-order (MP2) perturbation theory. *Chemical physics letters*, 181(6), 497-500.
- [74] Schäfer, T., Ramberger, B., & Kresse, G. (2017). Quartic scaling MP2 for solids: A highly parallelized algorithm in the plane wave basis. *The Journal of Chemical Physics*, 146(10).
- [75] Grimme, S. (2003). Improved second-order Møller–Plesset perturbation theory by separate scaling of parallel-and antiparallel-spin pair correlation energies. *The Journal of chemical physics*, 118(20), 9095-9102.
- [76] Frisch, M. J. (2009). gaussian09. <http://www.gaussian.com/>.

- [77] Hino, Y., & Hayashi, S. (2021). Thermotriggered Domino-like Single-Crystal-to-Single-Crystal Phase Transition from Face-to-Edge to Face-to-Face Packing of Anthracenes. *Chemistry—A European Journal*, 27(70), 17595-17600.
- [78] Roux, M. V., Temprado, M., Chickos, J. S., & Nagano, Y. (2008). Critically evaluated thermochemical properties of polycyclic aromatic hydrocarbons. *Journal of Physical and Chemical Reference Data*, 37(4), 1855-1996.
- [79] Marco Lima, "Filmes Finos de Semicondutores Orgânicos", MSC, 2021.
- [80] Monte, M. J., Santos, L. M., Fulem, M., Fonseca, J. M., & Sousa, C. A. (2006). New static apparatus and vapor pressure of reference materials: naphthalene, benzoic acid, benzophenone, and ferrocene. *Journal of Chemical & Engineering Data*, 51(2), 757-766.
- [81] Chirico, R. D., Knipmeyer, S. E., Nguyen, A., & Steele, W. V. (1989). The thermodynamic properties of biphenyl. *The Journal of Chemical Thermodynamics*, 21(12), 1307-1331.
- [82] Lima, L. M. S. S., Santos, L. M. N. B. F., & Ribeiro da Silva, M. A. V. (2009). Estudo energético de alguns hidrocarbonetos aromáticos policíclicos e polifenilos (Doctoral dissertation, Ph. D. Dissertation, University of Porto, Portugal).
- [83] Lima, C. F., Sousa, C. A., Rodriguez-Borges, J. E., Melo, A., Gomes, L. R., Low, J. N., & Santos, L. M. (2010). The role of aromatic interactions in the structure and energetics of benzyl ketones. *Physical Chemistry Chemical Physics*, 12(37), 11228-11237.
- [84] House, H. O., Ghali, N. I., Haack, J. L., & VanDerveer, D. (1980). Reactions of the 1, 8-diphenylanthracene system. *The Journal of Organic Chemistry*, 45(10), 1807-1817.
- [85] House, H. O., Koepsell, D., & Jaeger, W. (1973). Derivatives of 1, 8-diphenylanthracene. *The Journal of Organic Chemistry*, 38(6), 1167-1173.



